Alma Mater Studiorum · Università di Bologna

SCUOLA DI SCIENZE
Corso di Laurea in Astrofisica e Cosmologia
Dipartimento di Fisica e Astronomia

IRAS 00183-7111: ALMA and X-ray view of an Ultra Luminous Infrared Galaxy

Tesi di Laurea Magistrale

Relatore:
Chiar.mo Prof.
Cristian Vignali

Co-relatore:
Dott.Arturo Mignano

Presentata da:
Ilaria Ruffa

Sessione I
Anno Accademico 2016-2017

This Thesis work was done as part of the research activity of the Italian ALMA Regional Centre and of the Istituto di Radioastronomia - Istituto Nazionale di Astrofisica (INAF) in Bologna.

Ai miei genitori
a cui devo tutto
e alla Vita
che mi ha resa
forte come il mare
in tempesta
e fragile come
le foglie d'autunno

Contents

List of Tables

List of Figures

Sommario

Lo scopo di questo lavoro di Tesi è stato quello di condurre uno studio multi-frequenza della sorgente IRAS 00183-7111 (I00183) a $z = 0.327$, appartenente alla classe delle galassie ultraluminose nell'infrarosso (Ultra Luminous Infrared Galaxies o ULIRG). L'analisi è stata condotta utilizzando dati nel millimetrico, osservati con l'interferometro ALMA (Atacama Large Millimeter/submillimeter Array), e dati in banda X, con l'obiettivo principale di delineare meglio le caratteristiche della fonte di energia dominante di questa sorgente e verificare se il gas molecolare tracciato dal CO possa essere ritenuto responsabile dell'oscuramento rilevato dalle osservazioni in banda X. I00183 è una delle ULIRG più luminose scoperte dal satellite IRAS, con una luminosità bolometrica dell'ordine di 9×10^{12} $L_{\odot}$, emessa principalmente nel regime del lontano infrarosso. Quest'ultima è una proprietà tipica delle ULIRG: la loro elevata luminosità viene di solito attribuita a fenomeni di merger tra galassie a spirale ricche di gas, che innesca sia un processo di accrescimento sul buco nero centrale (AGN), sia violenti fenomeni di formazione stellare su scale nucleari ("starburst"). Dal punto di vista teorico, lo scenario più comunemente accettato è quello secondo cui il pre-esistente buco nero centrale super massiccio accresce materia ad un tasso elevato ed è oscurato da spessi strati di gas e polveri che sono stati convogliati dal merging nelle regioni centrali; successivamente, si possono verificare fenomeni di fuoriuscita di "venti" di materia ad altissima velocità dall'AGN ("quasar wind"), che allontanano il materiale di cui l'AGN è circondato. Questa attività termina quando le riserve di gas delle regioni centrali si esauriscono e la maggior parte del gas rimanente viene esplulso, interrompendo sia l'attività di AGN, sia quella di formazione stellare, e lasciando la galassia evolvere successivamente come un sistema passivo. Le ULIRG sono sorgenti molto diffuse, ma la grande quantità di polvere diffusa causa una significativa estinzione del nucleo, rendendo complicato lo studio delle loro regioni più interne e difficile distinguere se la fonte dominante di energia sia attribuibile ad attività da AGN o da formazione stellare.
I00183 è stata selezionata dal diagramma diagnostico di Spoon (Spoon *et al.* 2007), che mette a confronto gli spettri di un centinaio di galassie luminose nell'infrarosso, confrontando la larghezza equivalente della componente di emissione a 6.2 μm degli Idrocarburi Policiclici Aromatici (PAH) con l'intensità della banda di assorbimento dei silicati centrata a 9.7 μm. Lo studio di queste componenti spettrali costituisce uno strumento molto potente per indagare sul relativo contributo energetico

proveniente dalla formazione stellare e/o da AGN nelle ULIRG. Il diagramma di Spoon è suddiviso in nove regioni, che rappresentano le classi in cui gli spettri delle galassie campione sono stati suddivisi. I00183 è stata selezionata dalla regione 3A del diagramma di Spoon, dove sono collocate le sorgenti classificate come fortemente oscurate, sulla base delle profonde bande di assorbimento dei silicati presenti nei loro spettri. I00183 è situata comunque in una posizione di "confine" all'interno del diagramma di Spoon, trovandosi tra la regione in cui sono collocati i candidati AGN fortemente oscurati e quella popolata dalle galassie classificate come AGN non oscurati. Numerosi studi in diverse bande spettrali sono stati effettuati su questa sorgente, la cui posizione da "outlier" nel diagramma di Spoon sembrerebbe attribuibile alla sua peculiare natura. I00183 ha una luminosità radio a 4.8 GHz dell'ordine di 3×10^{25} W Hz^{-1}, che la classifica come una radio galassia brillante FRII, ed è stata sttribuita all'ingente attività di accrescimento su un buco nero centrale; la detezione dell'AGN risulta ardua a più alta frequenza a causa dell'elevata estinzione causata dalle polveri, legate ad un'intensa attività di formazione stellare (~ 220 $M_\odot$ yr^{-1}), che contribuisce per circa il 14% alla sua luminosità bolometrica. In base alle caratteristiche osservate, I00183 potrebbe trovarsi nel breve periodo di transizione tra la fase di intensa e dominante attività di formazione stellare innescata dal merging, e la fase di accrescimento non oscurato dell'AGN centrale, la cosidetta "quasar-mode accretion".
Al fine di studiare le proprietà sub-millimetriche di I00183, sono state analizzate osservazioni ALMA Ciclo 0 di archivio in Banda 3 (87 GHz) e Banda 6 (270 GHz). È importante sottolineare che il Ciclo 0 di ALMA era prevalentemente una fase di test dello strumento (cosiddetta "Early Science") per cui il riprocessamento dei dati è fortemente consigliato. Il lavoro principale di questa tesi è stato quello di calibrare i dati "grezzi", confrontando poi i risultati ottenuti con quelli presenti in archivio e cercando di apportare un miglioramento.
Le proprietà in banda X di I00183 sono state studiate analizzando osservazioni *Chandra*, XMM-*Newton* e *NuSTAR*, che consentono una copertura a banda larga dello spettro in banda X ($\sim$0.5$-$30 keV). Sono stati utilizzati dati di archivio *Chandra* e XMM-*Newton*, con tempi di esposizione effettivi di 22 e 22.2 ks, rispettivamente; la riduzione dei dati è stata condotta utilizzando i software CIAO e SAS, rispettivamente; i 109 ks *NuSTAR* sono ancora privati e gli spettri ridotti sono stati gentilmente ottenuti dal PI (K. Iwasawa). La dettagliata analisi spettrale è stata condotta utilizzando il software XSPEC e si è svolta cercando di riprodurre la forma spettrale a partire da semplici modelli fenomenologici, introducendo poi modelli analitici più complessi, per tenere conto della fisica dei processi che coinvolgono questa sorgente.
Nel capitolo 1 di questo lavoro di Tesi verrà presentato un quadro generale della problematica scientifica, descrivendo le principali proprietà di I00183 emerse da diversi lavori. Nel capitolo 2 verranno introdotti i principi di base dell'interferometria, applicata poi a tutto il processo di calibrazione dati. Nel capitolo 3 verrà presentato

lo strumento ALMA, fornendo una breve descrizione delle sue principali caratteristiche tecniche e capacità presenti e future. Il capitolo 4 sarà dedicato alla descrizione del processo di calibrazione dei dati ALMA, fino alla presentazione delle immagini ottenute. Nel capitolo 5 verranno descritti e discussi i risultati ottenuti dalle osservazioni ALMA. Il capitolo 6 presenterà i risultati derivanti dalla riduzione e analisi spettrale dei dati in banda X, con una piccola introduzione sui principi di base dell'astronomia X e le proprietà dei satelliti di cui sono state usate le osservazioni. Infine, l'intero lavoro verrà riassunto, ponendo l'accento sui principali risultati ottenuti da questo progetto di tesi e sulle possibili prospettive future.

Abstract

The aim of this Thesis work is to study the multi-frequency properties of the Ultra Luminous Infrared Galaxy (ULIRG) IRAS 00183-7111 at $z = 0.327$, connecting ALMA sub-mm/mm observations with those at high energies in order to place constraints on the properties of its central power source and verify whether the gas traced by the CO may be responsible for the obscuration observed in X-rays.
IRAS F00183-7111 (I00183, hereafter) is one of the most luminous ULIRGs known: its bolometric luminosity, $9 \times 10^{12}\ L_{\odot}$, is mostly radiated in the far-IR. This property is typical of ULIRGs: their high luminosity is often attributed to the merger of two gas-rich spirals which triggers both Active Galactic Nuclei (AGN) activity in a pre-existing quiescent black hole and a powerful nuclear starburst. The current theoretical picture suggests that the supermassive black hole at the center of the galaxy grows by accretion while surrounded by thick layers of dust and gas which are then blown away by outflows driven by powerful quasar wind. This activity ceases when the fuel provided to the central regions is exhausted, and most of the remaining gas is expelled, switching off both the AGN and the star-forming activity, and leading to form a passive galaxy. ULIRGs are much more common at high redshift, but the presence of high amounts of dust causes significant extinction to their nuclei, making hard the study of their inner regions and difficult to determine whether their dominant power source is due to AGN or star-formation activity.
I00183 was selected from the so-called Spoon diagnostic diagram (Spoon *et al.* 2007) for mid-infrared spectra of infrared galaxies based on the equivalent width of the 6.2 μm Polycyclic Aromatic Hydrocarbon (PAH) emission feature versus the 9.7 μm silicate strength. Such features are a powerful tool to investigate the contribution of star formation and AGN activity in this class of objects. The diagram is divided into nine region representing the classes in which the galaxy spectra of the sample are distributed. I00183 was selected from the top-left region of the plot where the most obscured sources characterized by a strong Si absorption feature are located. According to its spectral features, I00183 is a peculiar example of an ULIRG whose nucleus is loud at 4.8 GHz ($L_{4.8\ GHz} = 3 \times 10^{25}\ W\ Hz^{-1}$) and buried within a dusty galaxy with a star-formation activity ($\sim$220 $M_{\odot}\ yr^{-1}$); it is believed to be in the brief transition period between merging starburst and 'quasar-mode' accretion.
To link the sub-mm/mm to the X-ray properties of I00183, ALMA archival Cycle 0 data in Band 3 ($\sim$ 87 GHz) and Band 6 ($\sim$ 270 GHz) have been calibrated and

analyzed, using CASA software. ALMA Cycle 0 was the Early Science program for which data reprocessing is strongly suggested. The main work of this Thesis consisted in reprocessing raw data to provide an improvement with respect to the available archival products and results, which were obtained using standard procedures.
The high-energy data consists of *Chandra*, XMM-*Newton* and *NuSTAR* observations which provide a broad coverage of the spectrum in the energy range $\sim 0.5-30$ keV. *Chandra* and XMM archival data were used, with an exposure time of 22 and 22.2 ks, respectively; their reduction was carried out using CIAO and SAS software. The 100 ks *NuSTAR* are still private and the spectra were obtained by courtesy of the PI (K. Iwasawa). A detailed spectral analysis was done using XSPEC software; the spectral shape was reproduced starting from simple phenomenological models, and then more physical models were introduced to account for the complex mechanisms that involve this source.
In Chapter 1, an overview of the scientific background will be discussed, with a focus on the target, I00183, and the Spoon diagnostic diagram, from which it was originally selected. In Chapter 2, the basic principles of interferometry will be briefly introduced, with a description of the calibration theory applied to interferometric observations. In Chapter 3, ALMA and its capabilities, both current and future, will be shown, explaining also the complex structure of the ALMA archive. In Chapter 4, the calibration of ALMA data will be presented and discussed, showing also the obtained imaging products. In Chapter 5, the analysis and discussion of the main results obtained from ALMA data will be presented. In Chapter 6, the X-ray observations, data reduction and spectral analysis will be reported, with a brief introduction to the basic principle of X-ray astronomy and the instruments from which the observations were carried out. Finally, the overall work will be summarized, with particular emphasis on the main obtained results and the possible future perspective.

Chapter 1

Scientific background

1.1 Introduction

Active Galactic Nuclei (AGN) are one of the most powerful sources of radiation in the Universe. The complex physical processes involving these sources lead them to emit along the whole electromagnetic spectrum, therefore multi-wavelength studies are needed to characterize their overall properties. A complete census of the AGN population, including the most elusive, buried sources, is also required to better understand the observed variety in properties, to "map" their evolution up to high redshift, and shed light on the black holes/host galaxies co-evolution issue. Moreover, the detection and the study of the most obscured objects is essential to clarify their contribution to the unresolved X-ray cosmic background. Ultra Luminous Infrared Galaxies (ULIRGs) are a particular class of objects, most of which seem to host obscured accretion, especially the most powerful ones. IRAS 00183-7111 (I00183, hereafter), the target of this Thesis work, is a peculiar and widely studied example within this class of galaxies, and its main properties will be described in this Chapter. Also an overview of the scientific background will be presented, with a focus on AGN and ULIRGs properties, and presenting the so-called Spoon diagnostic diagram, from which I00183 was originally selected. Throughout this work distances and luminosity have been computed assuming a ΛCDM cosmology, where: $H_0 = 70$ km s^{-1} Mpc^{-1}, $\Omega_M = 0.27$ and $\Omega_\Lambda = 0.73$.

1.2 Active Galactic Nuclei

It is widely accepted that almost every galaxy hosts a Super-Massive Black Hole (SMBH, $10^6 - 10^9$ M$_\odot$) in its nuclear regions, but only a fraction of them ($\sim 10\%$) have an active one. A SMBH is called "active" when emits radiation through a gravitational process in which the material of a surrounding accretion disk falls into the BH and is converted in energy; since this process produces a huge amount of energy

($10^{42} - 10^{48}$ erg s^{-1}) in small volumes (1−2 pc[1]), it is considered one of the most powerful engines in the Universe, providing a significant contribution to the energy radiated over cosmic times. Galaxies which host an active SMBH are called Active Galactic Nuclei (AGN), and are divided into two major categories, on the basis of their optical spectral properties: Type 1 and Type 2. Type 1 are unobscured objects which show both narrow and broad emission lines in their optical spectra, and a strong optical/UV continuum; Type 2 are obscured AGN, which show only narrow emission lines and a suppressed continuum. In the X-ray domain the main difference between the two categories is the progressive suppression of the primary power-law emission from Type 1 to Type 2 and the limited presence of nuclear emission in the soft-band (below 2 keV) in the most obscured objects. Moreover, highly obscured AGN have Fe Kα emission line with large equivalent width (≥ 1 keV) and intrinsic N_H column density larger than 10^{24} cm^{-2}; such kind of objects are called Compton-thick AGN ($N_H > 1 \times 10^{24}$ cm^{-2}). Historically, different AGN types were brought into a single framework by the standard Unified Model (e.g. Antonucci 1993, Urry & Padovani 1995, Veilleux 2003 and references therein), according to which Type 1 and Type 2 objects belong to the same category and the observed spectral differences result from different viewing angles: Type 1 AGN are nearly face-on objects, and the nucleus can be directly seen; Type 2 AGN have larger viewing angles, thus the line of sight intercepts the obscuring medium surrounding the nucleus; when the AGN is seen completely face-on assumes a star-like visual appearance and is called *Quasar* (Quasi-stellar Object, also known as QSO), whose optical spectrum is characterized by a strong continuum and very broad emission lines. A schematic picture of the Unified model is shown in figure 1.1. In this scenario, the central SMBH is surrounded by an accretion disk of infalling material on scales down to a few gravitational radii; it involves spatial scales of the order of $\sim 10^{-3}$ pc. The gravitational radius is usually defined as $R_g = \frac{GM_{BH}}{c^2}$, where where G is the gravitational constant, M_{BH} is the black hole mass and c is the speed of light. Typically, $R_g = 1/2R_s$, where R_s is the Schwarzschild radius; it is defined as the radius of a sphere such that, if all the mass of an object is compressed within that sphere, the escape speed from its surface would equal the speed of light. A black hole is an example of an object smaller than its Schwarzschild radius. The accretion disk is, in turn, surrounded by a dusty torus whose typical extension are $r \sim 1 - 100$ pc from the nucleus. Clouds of gas also extend from the central regions, and they are divided into the closer and denser Broad Line Regions ($r \sim 0.01 - 0.1$ pc) and the farther and rarefied Narrow Line Regions ($r \sim 100 - 1000$ pc). Under some physical conditions, AGN can produce an outflow of magnetically-confined relativistic particles, i.e. the jets, which are the source of the radio synchrotron emission. The AGN are generally classified as *radio-loud* when the ratio between the radio (5 GHz) and optical (4400 Å) emission is > 10, they are considered *radio-*

[1] 1 pc$\simeq 3.08 \times 10^{18}$ cm

quiet, otherwise (Kellermann 1989).
One of the most important issues in modern astrophysics is the connection between the growth of SMBHs and their host galaxies, the so-called "co-evolution" (e.g. Kormendy & Ho 2013, for a review). Since its discovery, many efforts had been made to understand the origin of the tight correlation between the SMBH mass and the velocity dispersion (or the bulge stellar mass) in nearby galaxies (e.g. Kormendy 1995, Magorrian *et al.* 1998, Ferrarese *et al.* 2000). Important observational evidences about the mutual interplay were found in the last years, showing, for example, that the energetic output of an accreting SMBH can significantly affect its surrounding environment: the AGN feedback is considered as a more effective mechanism of quenching gas cooling and star formation (e.g. Somervile *et al.* 2008, Fabian 2012). In order to better constrain this scenario and understand the effective role of SMBHs in the context of galaxy formation and evolution, a complete survey of the AGN population is required, with particular attention to the search and the study of the most elusive ones. The obscured accretion phase is a crucial step in the AGN and co-evolution scenario, since much of the SMBH mass growth occurs during this phase (e.g. Hopkins *et al.* 2005, Treister *et al.* 2010). A complete census of the most obscured objects is also needed to better understand their contribution to the unresolved X-ray cosmic background (e.g. Maiolino *et al.* 2003, Gilli *et al.* 2007).
In the heavily obscured objects, the absorbed optical to soft X-ray primary radiation is reprocessed by the obscuring medium and re-emitted at longer wavelengths, driving a significant luminosity in the infrared regime (e.g. Nardini & Risaliti 2011). The intense infrared emission from the hot dust layers exposed directly to the central engine enables the detection of heavily obscured AGN components that are missed at others wavelengths. A significant fraction of heavily obscured AGN candidates seem to be harbored in the so-called Ultra Luminous Infrared Galaxies (ULIRGs), that are considered unique laboratories to place constraints on the properties of the most obscured sources.

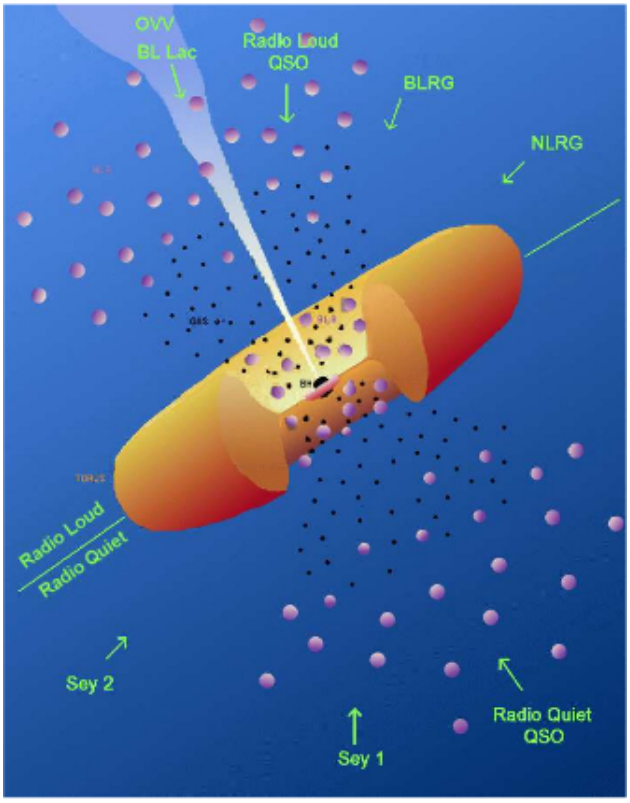

Figure 1.1: Unified Model of the AGN adapted from Urry & Padovani (1995). In this framework, the central SMBH is surrounded by an accretion disk of infalling material on scales of the order of $\sim 10^{-3}$ pc. The accretion disk is, in turn, surrounded by a dusty torus whose typical extension are $r \sim 1 - 100$ pc from the nucleus. Clouds of gas also extend from the central regions, and they are divided into the closer and denser Broad Line Regions ($r \sim 0.01 - 0.1$ pc) and the farther and rarefied Narrow Line Regions ($r \sim 100 - 1000$ pc). The differences observed in their optical spectra are attributed to different viewing angles: Type 1 (i.e. unobscured AGN) are nearly face-on objects, and the nucleus can be directly seen; Type 2 (i.e. obscured AGN) have larger viewing angles, thus the line of sight intercepts the obscuring medium surrounding the nucleus. When an AGN is seen completely face-on is called *quasar*.

1.3 Ultra Luminous Infrared Galaxies (ULIRGs)

The Ultra Luminous Infrared Galaxies are a class of galaxies historically defined in terms of their huge infrared luminosity $L_{8-1000\mu m} > 10^{12}$ $L_{\odot}$ (e.g. Sanders & Mirabel 1996). They were discovered by the Infrared Astronomical Satellite[2] (IRAS) in 1983, and were found to be more numerous at $z > 1$ than locally; these distant ULIRGs may signpost the obscured phases of very dramatic events suspected of building the most massive galaxies seen in the local Universe (e.g. Lonsdale *et al.* 2006, for a review).

1.3.1 The AGN/starburst components

It is now well established that the hidden source of the primary radiation field inside ULIRGs is a combination of extremely starburst activity (i.e. a star forming event with a gas exhaustion timescale very short compared to the Hubble time) and highly obscured accretion (e.g. Genzel *et al.* 1998). The distinction between the two power sources is very difficult due to the high dust extinction of their nuclei, which leads to a substantial obscuration even in the mid-infrared and X-ray regimes. Despite this, several spectroscopic signatures of starburst and/or AGN activity can be identified: line strengths, ratios and spectral shapes can provide powerful constraints on the nature of the source of excitation (Lonsdale *et al.* 2006); thus, it is now clear that the complexity of the involved phenomena require a multi-wavelength approach.
Genzel et al. (1998) demonstrated that it is possible to separate AGN from starburst power by comparing the strength of the 7.7 μm PAH equivalent width to high/low excitation line ratios such as 25.9 μm [O IV]/12.8 μm [Ne II]. PAH molecules will be destroyed by high-intensity AGN radiation fields, so low PAH/continuum ratio should correlate with strong [OIV]/[NeII] ratios; however, dense nuclear environments can hide AGN activity even at mid-infrared wavelengths. Also the mid-IR continuum shape can be a powerful diagnostic itself, since the peak of the thermal dust emission is strongly dependent on the heating mechanism: $\sim$ 20 μm in the close vicinity of an AGN, $\sim$ 100 μm in star-forming regions. On the basis of their 25/60 and 60/100 μm infrared flux ratios, ULIRGs are found to fall into two general classes: "cool" systems, which show low 25/60 and 60/100 μm infrared flux ratios, are considered dominated by star formation, while "warm" systems, with higher infrared flux ratios, are usually assumed to be AGN-dominated (Surace *et al.* 1998). Warm ULIRGs tend to have optical spectral features typical of unobscured AGN, while cool ones have starburst or Type 2-AGN optical spectra.
The studies of the molecular gas, primarily traced by CO and HCN, demonstrated that ULIRGs host huge amounts ($\geq 10^{10}$ $M_{\odot}$) of cool gas in their central regions,

[2]The Infrared Astronomical Satellite (IRAS) was the first-ever space observatory to perform an all-sky survey at infrared wavelengths. It was launched in January 25, 1983 and the mission lasted ten months.

concentrated into a radius of $r \leq 0.5 - 1$ kpc, and with densities of 10^4 cm^{-3} (e.g. Downes & Solomon 1998). Particularly, the HCN molecule is a tracer of warmer (60−90 K) and denser ($10^5 - 10^7$ cm^{-3}) gas, and Gao & Solomon (2004) demonstrated that ULIRGs have a much higher HCN to CO luminosity ratio with respect to quiescent spirals like the Milky Way.
However, in the last years, many efforts have been directed to disentangle the AGN and starburst components in ULIRGs (e.g. Veilleux *et al.* 2002, Franceschini *et al.* 2003, Farrah *et al.* 2006, Imanishi *et al.* 2010). Most of these works represent systematic studies of large nearby samples of ULIRGs, observed in radio, mid-infrared, and X-ray regimes, with the primary aim to estimate the AGN contribution. The observed properties seems to be in agreement from each other, converging in some fundamental points:

- The majority of ULIRGs have optical spectra reminiscent of starburst, but with an increase in the fraction of ULIRGs with Type 1 or 2 AGN spectra with increasing IR luminosity; however, most of the ULIRGs with AGN spectral features also show evidence for ongoing or recent star formation;

- The hard X-ray luminosity (2−10 keV) associated with the AGN in ULIRGs is systematically below ($< 10^{42}-10^{43}$ erg s^{-1}) from that expected for a local QSO of the same infrared luminosity; furthermore, many ULIRGs X-ray spectra show an excess of emission below 2 keV, which can be, in most cases, associated to thermal emission with kT$\sim$0.7 keV, related to the starburst activity;

- From a combination of mid-IR and X-ray spectral analysis, it was found that the environment surrounding the AGN component in ULIRGs is much richer in gas and dust than in ordinary active galaxies, and the degree of absorption can be directly related to the starburst intensity, indicating a strong interaction between the two processes.

Therefore, these studies are fundamental not only to understand the nature of local ULIRGs, but also to place constraints on the interplay and mutual feedback between star formation and BH accretion, which are basic ingredients of galaxy formation and evolution (e.g. Zheng 2013).

1.3.2 The evolutionary scenario

According to the multi-wavelength observed properties, the most popular scenario suggests that ULIRGs are triggered by major merger events between gas-rich galaxies which channeled very large masses of gas and dust into the few hundred parsecs of their central regions (e.g. Sanders & Mirabel 1996, Veilleux *et al.* 2002). For this reason, ULIRGs are placed in an evolutionary sequence (fig. 1.2) in which the major galaxy mergers first result in a massive cool starburst-dominated ULIRG, followed by a warm ULIRG as the QSO turns on and heats the surrounding dust

layers; finally, the QSO emerges in an optically bright phase when it blows away the surrounding material, quenching both star forming and AGN activity, and the resulting stellar system evolves as a passive spheroid (e.g. Lipari *et al.* 2003, Hopkins *et al.* 2008). This picture provides supporting evidence to the co-evolution framework, but is in contrast with the Unified Model scenario described above, for which an optically bright QSO viewed not completely face-on would appear as a ULIRG; both scenarios, however, predict close relationship between starburst and AGN.

The evolutionary sequence is supported theoretically by works reporting high resolution hydrodynamic simulations of major mergers (e.g. Di Matteo *et al.* 2005, Hopkins *et al.* 2005); these studies predict highest accretion rates at late merger stages, when the mass of the SMBH rapidly grows, followed by the most luminous optically bright QSO phase. The period of high obscuration would correspond to an obscured QSO, i.e. an AGN-powered ULIRG, while the bulk of the starburst activity occurs in the earlier merger stages (Hopkins *et al.* 2005).

Observationally, optical imaging from the Hubble Space Telescope (HST) offered enhanced resolution to analyze the morphology of these objects. An early HST study presented by Surace *et al.* (1998) was focused on a small sample of ULIRGs with "warm" infrared colors ($f_{25}/f_{60} > 0.2$, with f_{25} and f_{60} as the 25 μm and 60 μm IRAS fluxes, respectively); this study indicates that all of the sample show signs of interaction, with complex structures in their nuclear regions. Several systems showed a large number of compact bright "knots" a few hundred parsecs in diameter, whose ages suggest they result from the merger. Complementary, a ground-based survey of ULIRGs with "cool" infrared colors (Surace *et al.* 2000) found a similar picture: all the galaxies shows sign of interactions, from early to late stage, and many systems harbor "knots" similar to those seen in the warm sample. The optical magnitudes are, in most cases, relatively modest, compared to their enormous infrared luminosity. A later HST survey of an unbiased sample of ULIRGs (both "cool" and "warm" systems) conducted by Farrah *et al.* (2001), found also similar results. As a consequence, ULIRGs are expected to evolve into passive spheroidal systems as the galaxy mergers that appears to trigger their activity progresses (e.g. Dasyra *et al.* 2006).

According to this picture, a significant fraction of heavily obscured AGN is harbored in ULIRG at late merger stages. The study of elusive AGN hosted in these systems is a proper way to provide new clues in the proposed evolutionary scenario. For this reason, adopting a multi-wavelength approach and, in particular, using the best data currently available, is the best strategy to shed light on the open AGN/ULIRG issue.

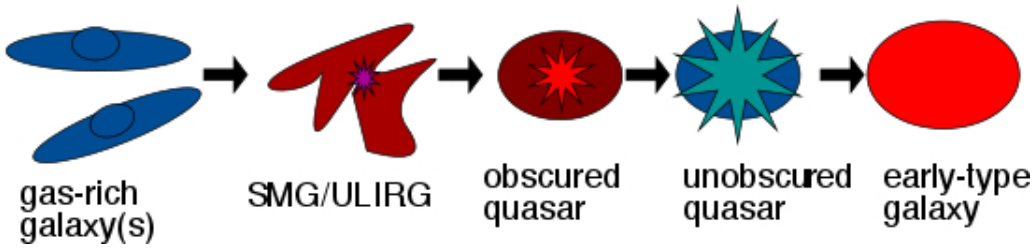

Figure 1.2: A schematic picture of the ULIRG evolutionary sequence adapted from Alexander & Hickox (2012). According to this scenario, ULIRGs are triggered by major mergers between gas-rich galaxies, fueling both violent starburst events and buried AGN activity. The QSO gradually turns on inside the nuclear regions and heats the surrounding dust; finally, the QSO becomes optically bright and powerful quasar winds blow away the surrounding layers of gas and dust. When the fuel provided to the central regions is exhausted, these activities cease and the galaxy evolves as a passive spheroidal system.

1.4 Source selection: the Spoon diagram

Since the discovery of ULIRGs, several diagnostic diagrams have been proposed to establish whether their huge luminosity can be attributed to starburst and/or AGN activity. I00183 was selected from the so-called Spoon mid-infrared diagnostic diagram (Spoon *et al.* 2007), which introduced the strength of the 9.7 μm silicate absorption feature as a tool to distinguish between different ULIRG populations. The Spoon diagram is mostly based on the observations which were carried out by the Infrared Spectrograph (IRS) aboard the Spitzer Space Telescope[3] and the Short Wavelength Spectrometer (SWS) on board the Infrared Space Observatory[4] (ISO). The sample comprises ~ 100 ULIRGs in the redshift range $0.02 < z < 0.93$, which is compared to samples of AGN and starburst templates from others IRS programs. Archival ISO SWS spectra of starburst nuclei were used. For all the spectra of the sample, Spoon *et al.* measured the equivalent width (EW) of the 6.2 μm Polycyclic Aromatic Hydrocarbon (PAH) emission feature as well as the strength of the 9.7 μm silicate absorption feature, and plotted the two quantities into the diagnostic diagram shown in figure 1.3. The flux in the 6.2 μm PAH emission band is measured by integrating the flux above an interpolated local continuum from 5.95 to 6.55 μm; the EW of the PAH is then obtained dividing the integrated PAH flux by the interpolated continuum flux density. The strength of the 9.7 μm silicate

[3]The NASA's Spitzer Space Telescope (SST) is an infrared space observatory launched in 2003. The satellite contains three instruments that allow it to perform astronomical imaging and photometry from 3.6 to 160 micrometers, spectroscopy from 5.2 to 38 micrometers, and spectrophotometry from 5 to 100 micrometers.

[4]The ESA's Infrared Space Observatory (ISO) was the world's first true orbiting infrared observatory, which was launched in November 1995 and lasted until April 1998. The instruments aboard ISO covered wavelengths from 2.5 to around 240 microns with spatial resolutions ranging from 1.5 arcsec (at the shortest wavelengths) to 90 arcsec (at the longer wavelengths).

feature is computed by adopting a local continuum and evaluating the ratio of the observed flux density (f_{obs}) to continuum flux density (f_{cont}) at 9.7 μm; consequently, the silicate strength parameter can be defined as:

$$S_{sil} = \ln \frac{f_{obs}(9.7\ \mu m)}{f_{cont}(9.7\ \mu m)} \tag{1.1}$$

For sources with silicate absorption features, S_{sil} assumes a negative value that can be interpreted as the negative of the apparent silicate optical depth.
The observed galaxy spectra are classified into nine different classes on the basis of their 6.2 μm PAH EW and 9.7 μm silicate strength; the average mid-infrared spectra for the eight populated classes (class 3C is not populated) are shown in figure 1.4. The classes 1A and 1B spectra are dominated by a hot dust continuum, but the class 1B differs from the class 1A spectrum by clearly showing the PAH emission features; such features become dominant in the class 1C spectrum. The EW of the PAH emission lines progressively decrease from the class 2C to 3B spectrum, and they are absent or very weak in the class 3A spectrum. Conversely, the silicate absorption features show an increasing depth from the 2C to the 3A spectra, where they become dominant; another noticeable feature from the class 2C to the 3A spectra is the progressive steepening of the 20−30 μm continuum. On the basis of their observed differences, the mid-infrared spectra were divided into three main groups: continuum-dominated spectra (classes 1A and 1B), PAH-dominated spectra (classes 1C and 2C), and absorption-dominated spectra (classes 3B, 3A and 2A). I00183 was selected from the 3A region of the diagram (black circle in fig. 1.3), showing in its mid-infrared spectrum strong silicate absorption features ($S_{sil} = -2.9$) and very low PAH 6.2 μm EW. As already explained, PAH molecules are destroyed by high-intensity AGN radiation fields, thus low or absent PAH features would reasonably indicate the presence of an intense AGN activity, and strong silicate absorption features suggest the presence of a dense nuclear environment. Therefore, these spectral characteristics are consistent with an heavily obscured AGN origin. Moreover, galaxies are not distributed randomly through the Spoon diagram; they appear to be distributed along two branches: one extending horizontally from the AGN-heated hot dust-dominated spectra (unobscured nuclei, class 1A) to the prototypical starburst-dominated nuclei (class 1C); the other branch extending diagonally from the deeply obscured nuclei of the 3A region to the starburst-dominated nuclei. Galaxies along the horizontal branch may be thought as combinations of AGN and starburst activity, while those along the diagonal branch may be thought as intermediate stages in between a fully obscured galactic nucleus (3A class) and an unobscured nuclear starburst (1C class). The black curved arrow in figure 1.3 indicates that a class 3A galaxy can be turned into a class 2A galaxy by adding a featureless hot dust continuum to the 3A absorbed continuum spectrum. The distribution of ULIRGs spectra along the full length of the horizontal and diagonal branches illustrates the diverse nature of the ULIRG

family, and seems to be coherent with an evolutionary scenario: the interaction may start with nuclei classified as starburst, which then gradually move up the diagonal branch as more dust is accumulated on the remnant nuclei and then the sources evolve from here, once the obscuring screen "breaks up" and the hidden nuclear engine is revealed (from 3A to 1A classes).

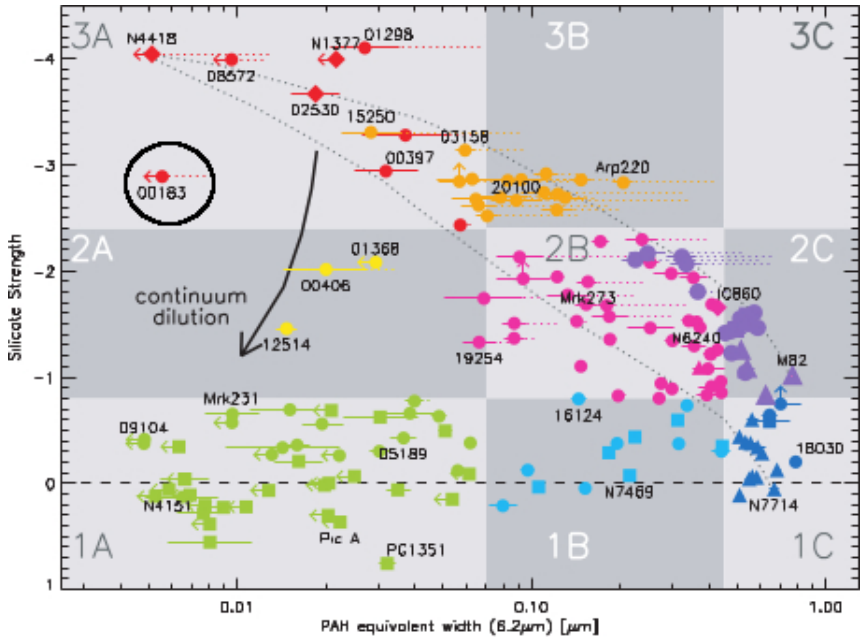

Figure 1.3: Spoon diagnostic plot of the equivalent width of the 6.2 μm PAH emission feature versus the 9.7 μm silicate strength, adapted from Spoon et al. (2007). Upper and lower limits are denoted by arrows. The galaxy spectra are classified into nine classes, identified by the gray rectangles, based on their position in this plot. Different colors are used to distinguish between the nine classes. The two dotted black lines are mixing lines between the spectrum of the deeply obscured and the starburst nuclei. The different plotting symbols are used to distinguish between different galaxy types: filled circles, filled triangles, filled squares, and filled diamonds refer to ULIRGs and HyLIRGs, starburst galaxies, Seyfert galaxies and QSOs, and other infrared galaxies, respectively. The black circle highlights the position of IRAS 00183-7111 (the target of this work).

1.4.1 The case of IRAS 00183-7111

I00183 is at $z = 0.3276$ (Roy & Norris 1997) and is one of the most luminous ULIRGs discovered by IRAS: it has a bolometric luminosity of 9×10^{12} $L_{\odot}$ (Spoon *et al.* 2009), most of which is radiated at far-infrared wavelengths. I00183 has been optically classified as a type-2 Seyfert galaxy by Armus *et al.* (1989), but multi-frequency studies of this source reveal its peculiar nature.
Mid-infrared imaging in the 2.5-11-6 μm range by Rigopoulou *et al.* (1999, fig. 1.5)

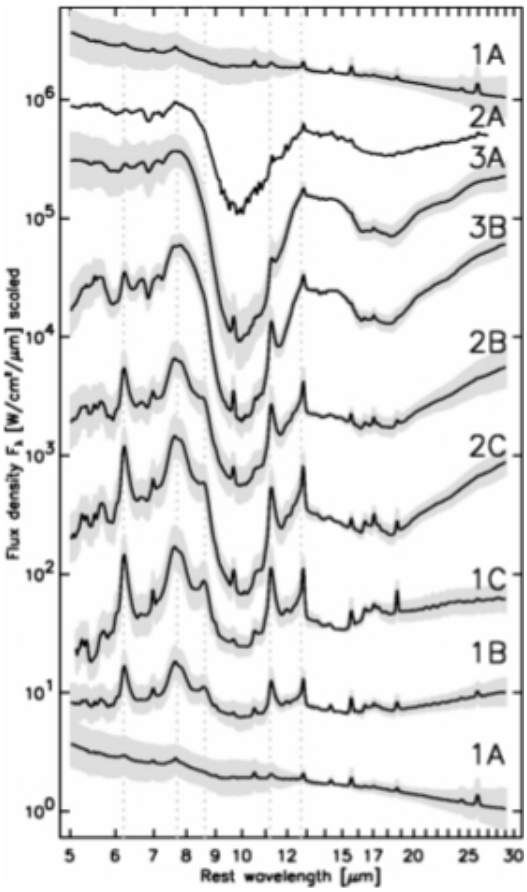

Figure 1.4: Average mid-infrared spectra for the eight populated classes of the Spoon diagram, adapted from Spoon et al. (2007). The gray shading represents the 1σ dispersion range. Spectra at the bottom of the figure are dominated by hot dust emission (classes 1A and 1B), spectra in the middle by PAH emission (classes 1C and 2C), while spectra toward the top by absorption features (classes 3B, 3A, and 2A).

revealed a disturbed morphology and a single nucleus, and long-slit spectroscopy (Drake *et al.* 2004, fig. 1.6) shows bright, highly-disturbed, ionized gas extending 50 kpc east and 10 kpc west of the nucleus. Recently, Norris *et al.* (2013) presented a R+I band image of I00183 obtained with the Australian Astronomical Telescope (AAT) in June 2012; this image (fig. 1.7) shows what appear to be tidal tails, or remnants from a recent merger. However, they argued that the many magnitudes of extinction that affect the nucleus ($A_V \geq 90$), even at near-infrared wavelengths, indicate that these image may be showing the outer shells of the galaxy, rather than the nucleus (Norris *et al.* 2013).

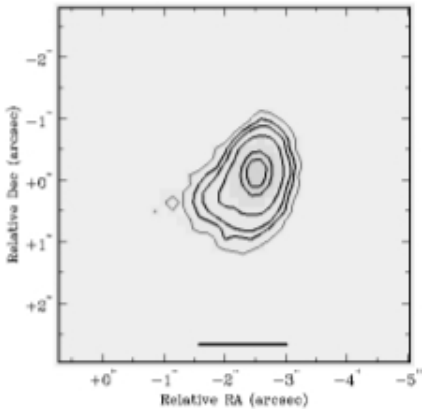

Figure 1.5: ISO mid-infrared (2.5-11.6 μm) image of I00183, adapted from Rigopoulou *et al.* (1999). The image shows a disturbed morphology and a single nucleus. The angular scale on the sky is indicated by the bar, which represent 10 kpc.

Nuclear outflows of high-velocity ionized gas traced by the 12.81 μm [NeII] and 15.51 μm [NeIII] emission lines were observed by Spoon *et al.* (2009). Line profiles are clearly asymmetric and strongly blueshifted, with FWHM of the order of $\sim$ 3000 km s^{-1}. They have found unusual excitation conditions in I00183, by comparing the ratio between the combined [NeII] and [NeIII] luminosity and the combined 6.2 and 11.2 μm PAH luminosity for a sample of 56 ULIRGs: if predominantly excited in star forming regions, the PAH luminosity should track the low-ionization neon emission line luminosity to within a factor two (Farrah *et al.* 2007). I00183 appears to be at least 8 time over-luminous in the neon lines compared to the PAH luminosity with respect to the average ratio for low-excitation ULIRGs ($\sim$ 0.4), thus they argued that the neon line ratios are consistent with an origin in fast shocks ($v > 500$ km s^{-1}) in an environment with gas densities $n > 10$ cm^{-3}: Spoon *et al.* (2009) placed I00183 in an evolutionary scenario in which the strongly blueshifted [NeII] and [NeIII] emission from shock may trace the (partial) disruption of the obscuring medium around a buried AGN.
The entire 4−27 μm Spitzer Infrared Spectrograph (IRS) spectrum of I00183 has been presented and discussed by Spoon *et al.* (2004, fig. 1.8). The spectrum is

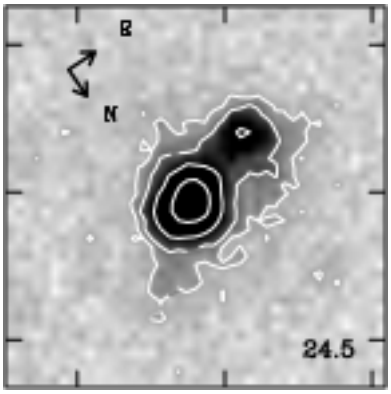

Figure 1.6: Grey scale R-band image of I00183, adapted from Drake *et al.* (2004). The overlaid contours highlight the low surface brightness structure. The image has dimensions of 150 kpc×150 kpc. Thick marks indicate intervals of 10 arcsec. North and east directions are indicated by arrows. The surface brightness of the lowest contour in magnitudes per square arcsec is given in the bottom right corner of the image, and contours are separated by 1 mag arcsec^{-2}.

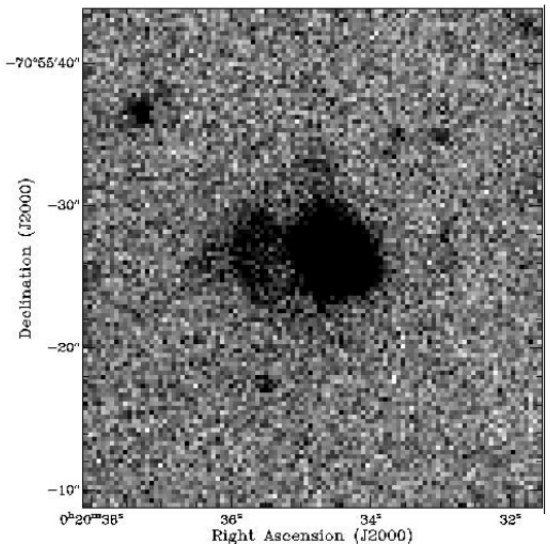

Figure 1.7: Uncalibrated R+I image of IRAS 00183-7111, adapted from Norris *et al.* (2013). The image was taken with the Australian Astronomical Telescope (AAT) in June 2012. The entire disturbed galaxy has a total extent of about 15 arcsec, which correspond to $\sim$ 70 kpc at the galaxy redshift ($z = 0.327$).

dominated by broad and overlapping absorption features, but also emission features have been detected in the 9.5-13 μm range. Particularly, they detected the 4.7 μm broad absorption feature of the CO, from which a column density of $\sim 10^{19.5}$ cm^{-2} was derived, and a gas temperature of 720 K. Beyond 8 μm, the spectrum shows the strong absorption silicate bands. Also the presence of 11.2 PAH and the 12.7-12.8 μm blend of PAH and [NeII] is inferred from the spectrum; their presence in the center of the optically thick 9.7 μm silicate band suggest an origin away from the absorbing medium. From the strength of the 11.2 μm PAH feature, they evaluated that the starburst activity has to contribute of at least 30% to the bolometric luminosity of the source. Spoon *et al.* suggest an exotic picture to explain the 4−27 μm spectral properties of I00183: the central dominant power source of I00183 seems to be deeply buried behind two obscuring shells. The inner shell is composed of a warm and dense gas with temperatures of $\sim$ 720 K and $n > 3 \times 10^6$ cm^{-3} that give rise to the CO absorption bands; the outer and colder shell is responsible for the absorption features of ice and silicates, and from the depth of the 9.7 μm features; the column density of the outer shell was evaluated to at least 10^{23} cm^{-2}. By placing their results in the diagram based on the 6.2 μm PAH and $L_{(FIR)}$ ratio, they argued that the IR spectrum of I00183 shows both signatures of AGN-like hot dust continuum and deeply obscured source (Spoon *et al.* 2004).

The presence of cold and dense molecular gas in the central regions of the galaxy

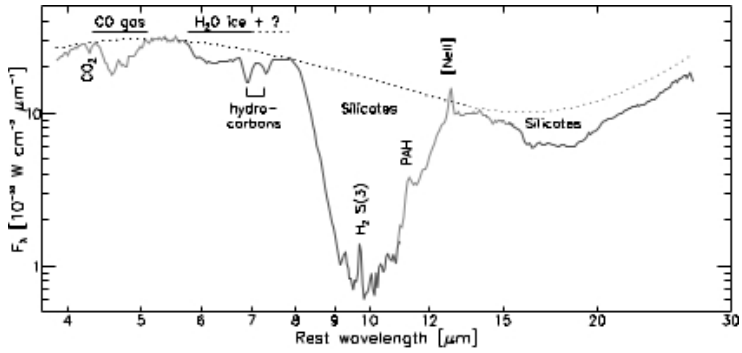

Figure 1.8: IRS low-resolution spectrum of IRAS 00183-7111 adapted from Spoon *et al.* 2004. The spectrum is dominated by strong silicate absorption bands at 9.7 and 18 μm with weaker absorption bands due to CO_2, CO, water ice, and hydrocarbons in the 4-7.5 μm range. Weak emission features of PAHs and [NeII] are detected at 11.2 and 12.8 μm, respectively. The dotted line shows the interpolated continuum.

was also indicated by weak ($\sim 3\sigma$) ALMA detections of HCN, HCO^+ and HNC emission lines at $\sim$ 1 mm (Imanishi & Nakanishi 2014); the detections were too weak to infer strong conclusions, but it is important to note that enhanced HCN emission is typical in AGN-dominated ULIRGs (Imanishi *et al.* 2009). Even if its IR spectrum lacks the 7.65 μm [NeIV] and 24.3/14.3 μm [NeV] lines, which are distinctive features observed in AGN spectra (Spoon et al. 2009), I00183 has been

overall classified as a peculiar example of an extremely obscured AGN. The differences from a classical AGN template spectrum at optical and infrared wavelengths are attributed to the dense dust layers surrounding it (Tran *et al.* 2011).
Radio observations are generally unaffected by the heavy dust obscuration that blocks the view at shorter wavelengths and allow to see directly the nucleus. Its radio luminosity of $\sim 10^{25.4}$ W Hz^{-1} at 4.8 GHz indicates that it is significantly more radio-luminous than expected from its FIR emission; such radio-excess places it within the regime of high luminosity (FRII-class) radio galaxy (Roy & Norris 1997). Very Long Baseline Interferometry (VLBI) observations of I00183 presented by Norris *et al.* (2012), reveal the presence of a compact core-jet AGN with a double-lobed morphology and compact jets only 1.7 kpc long (fig. 1.9). More recently, Mao *et al.* (2014) presented an ATCA $CO_{(1-0)}$ detection which was used to estimate a mass of molecular gas in I00183 of 2.4×10^{10} M$_\odot$; such gas mass is associated to a vigorous starburst with a SFR of ~ 220 M$_\odot$ yr^{-1}. They also estimated the relative contributions of star-formation and AGN to the total power of I00183, arguing that observations of molecular gas can be considered a powerful tool to show how the AGN is interacting with its host star-forming galaxy, because they are unaffected by the presence of AGN; they assert that only $\sim 14\%$ of the total power of the source is contributed by star-formation, which is a further indication that I00183 is predominately powered by the AGN (Mao *et al.* 2014).
The presence of a powerful AGN was also confirmed by the detection of a 6.7 keV FeK line (Fe XXV) with a large equivalent width (~ 1 keV) indicative of reflected light from an heavily obscured object, with a hard X-ray luminosity in the $2-10$ keV energy range of 2×10^{44} erg s^{-1} (Nandra & Iwasawa 2007).
All these results seems to be in agreement in placing I00183 in an evolutionary scenario which is consistent with the initial stage of the formation of a quasar, with powerful radio jets still confined by the gas from the galaxy that merged to form this system: I00183 appears to have been caught in the brief transition period as the radio-loud AGN switches on in the center and starts boring its way through the dense gas and dust (Norris *et al.* 2013). This picture could also explain the outlying location of I00183 in the mid-infrared Spoon diagnostic diagram (fig. 1.3): it lies between the two branches which separate deeply buried nuclei and unobscured AGN source, thus it may truly be an AGN in the process of disrupting its fully covering medium before settling on the AGN branch.
The aim of this work is to connect the sub-millimeter properties of I00183 with those at high energies, and one of the main goals is to investigate about the molecular gas (traced by the CO) contribution to the line-of-sight column density observed in the X-ray band.

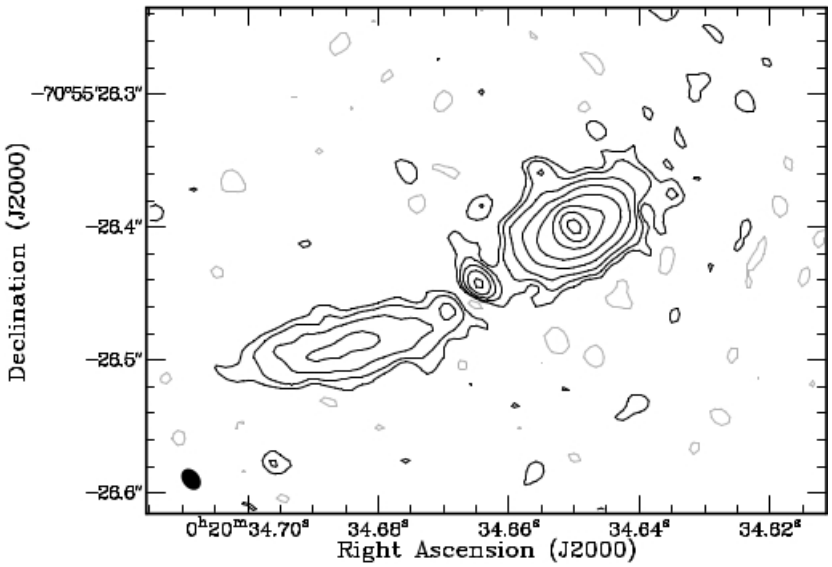

Figure 1.9: The VLBI 2.3 GHz image of I00183, taken from Norris et al. (2012). The peak surface brightness is 45 mJy beam^{-1}. The entire radio source is just over 1 kpc in extent.

Chapter 2

Interferometry: the basics

2.1 Introduction

The signal detection in the millimeter/radio regime is based on revealing the electric field of an incoming electromagnetic wave to obtain a picture of the sky. The measured astronomical signal is convolved with the response of the instrument and corrupted by several factors such as atmospheric turbulence and opacity. In millimeter/radio astronomy, the purpose is to "clean" the detected signal from all spurious features and to obtain images which describe as much as possible the real sky brightness distribution. In order to achieve this goal, it is important to have a good knowledge of the principles at the basis of the interferometric technique and the instruments used for detection, as well as of the theory of the calibration process.
In this chapter the basics of the interferometric theory and its parameters will be presented. In the second part, the calibration theory will be described, followed by the description of the imaging process.

2.2 Single-dish response

The signal detection in millimeter/radio astronomy is based on the principles of the Fraunhofer diffraction theory: under the approximation of a point-like source at infinity, the incident light is a plane and parallel waves front and its electric field distribution at the aperture forms a diffraction pattern on the focal plane; the Fourier transform of such power distribution is called **power pattern (beam)** and represents the response of the instrument to the incoming signal. The instrument consists of a parabolic aperture (i.e. *antenna*) which reflects the incident electromagnetic (EM) power and bring it on the focal plane, where the receiver is placed. The antenna power pattern is shown in figure 2.1. The cental gaussian-like feature is called the *mainlobe* and its Half Power Beam Width (HPBW) is $\sim \lambda/D$ where D is the antenna diameter (i.e. the aperture width). The 1D cross-section of the

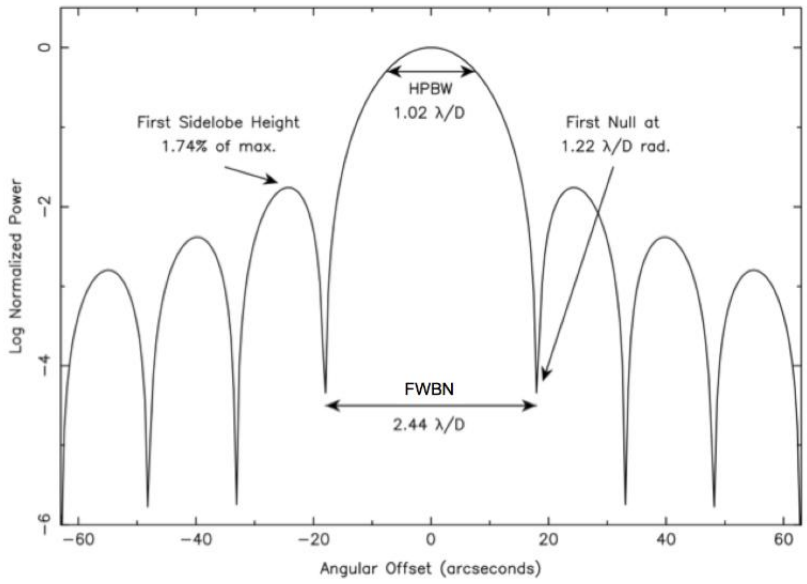

Figure 2.1: Normalized 1-D antenna power pattern for an uniformly illuminated antenna. The power is in log units. The HPBW of the main lobe is $\sim 1.02\lambda/D$ and the FWBN is $\sim 2.44\lambda/D$. The angle of the first null, i.e. the resolution is $\sim 1.22\lambda/D$

power pattern clearly shows that the constructive and destructive interference at increasing off-axis angles leads to a series of secondary lobes (*sidelobes*), that decrease with increasing off-axis angle. The angular distance between nulls is named the Full Width Between Nulls (FWBN) and it is given by 2.44 λ/D; half of the FWBN is considered the resolution of the antenna, i.e. the ability to distinguish between objects on the sky separated by a certain angular distance. The antenna power pattern can be altered by several factors such as surface imperfection[1]. The ALMA feedhorns (i.e. the receivers) has been designed to provide an antenna power pattern which is nearly Gaussian with low sidelobes, in order to improve resolution and sensitivity (meant as the sum of the electromagnetic power brought to the focus); actually the measured ALMA 12-m antenna HPBW is ~ 1.13 λ/D.
Defining θ and φ as orthogonal directional variable, it is possible to define $I_\nu(\theta, \varphi)$ as the directional function of the sky brightness distribution and $P_N(\theta, \varphi)$ as the normalized antenna power pattern (i.e. the power pattern divided by its value in the main lobe); the power measured by a receiver can be written as:

$$P_{rec} = \frac{1}{2} A_e \int_{4\pi} I_\nu(\theta, \varphi) P_N(\theta, \varphi) d\Omega \tag{2.1}$$

[1]Irregularities on the reflecting surface lead to a signal loss: the radiation which falls into a surface hole will be reflected later to the focus leading to a phase delay which can reduce the coherence of the incoming radiation and lead to a decreasing measured power. The tolerance on the surface imperfections depends by the observing frequency; in the case of ALMA short wavelengths it is nearly to $\lambda/16$

where 1/2 derives from the fact that a receiver is generally sensitive to only one mode of polarization[2]. A_e is the effective area of the antenna, i.e. the effective antenna area available for reflecting the incoming electromagnetic waves and it is usually less than the geometric area (πr^2). Their ratio gives the aperture efficiency:

$$\eta_A = \frac{A_{eff}}{A_{geom}} \tag{2.2}$$

which is always $\leq$1. ALMA's 12-m antennas have an aperture efficiency of $\sim 70\%$. The solid angle of the antenna power response can be found as:

$$\Omega_A = \int\int_{4\pi} P_N(\theta, \varphi) d\Omega \tag{2.3}$$

which can be used in first approximation to compute a relation between the received (S_r) and the emitted (S_e) flux, as a function of frequency (ν):

$$S_r(\nu) = S_e(\nu)\Omega_A \tag{2.4}$$

If the integral in eq. 2.3 is computed over the main lobe of the power pattern, it gives the solid angle of the main lobe:

$$\Omega_M = \int\int_{mainlobe} P_{norm}(\theta, \varphi) d\Omega \tag{2.5}$$

The directions from which an antenna can collect signal are limited by its shape so that it cannot be considered an isotropic receiver (i.e. receives flux from angles smaller than 4π); in this sense it is possible to define the directivity D of a single-dish as:

$$D = \frac{4\pi}{\Omega_A} \tag{2.6}$$

The monochromatic received power can be written as:

$$W(\nu) = mA_{eff} \int\int B(\nu, \theta, \varphi) P_N(\theta_0 - \theta, \varphi_0 - \varphi) d\Omega = kT_A \tag{2.7}$$

and it has units of W m^{-2} Hz^{-1}; in millimeter/radio astronomy the power received has units of *Janskys* (Jy), where 1 Jy = 10^{-26} W m^{-2} Hz^{-1} = 10^{-23} erg cm^{-2} s^{-1} Hz^{-1}. T$_A$ is the antenna temperature in K and it represents what the antenna effectively measure:

$$T_A = \frac{mA_{eff}S(\nu)}{k} = GS(\nu) \tag{2.8}$$

where k is the Boltzmann constant and G is the so-called **antenna gain**:

$$G = \frac{mA_{eff}}{k} \text{ [K/Jy]} \tag{2.9}$$

i.e. a measure of how well an antenna collects signal and it is related to the effective area.

[2]ALMA receivers are constructed with two independent receptors so that both modes of polarization can be detected simultaneously.

2.2.1 Basic principle of interferometry

Since the resolving power of a single-dish observation depends on the observing wavelengths, for millimeter/radio observations it could be very low compared to optical observations (lambda is larger by many orders of magnitude). Furthermore, it is not possible to increase D as much as to obtain the same angular resolution of ground-based optical telescope ($\sim$ 1 arcsec). Interferometry, also known as *aperture synthesis*, is the technique developed in order to obtain higher angular resolution images using the combined signal from two or more separated elements. The power response of each antenna is time averaged and then *cross-correlated* (i.e. multiplied) by a *correlator* and the resulting power pattern will be the sum of such products of voltage patterns from element pairs. Figure 2.2 shows a scheme of a simple two-antenna interferometer, where b is their distance, called *baseline*. The antennas in

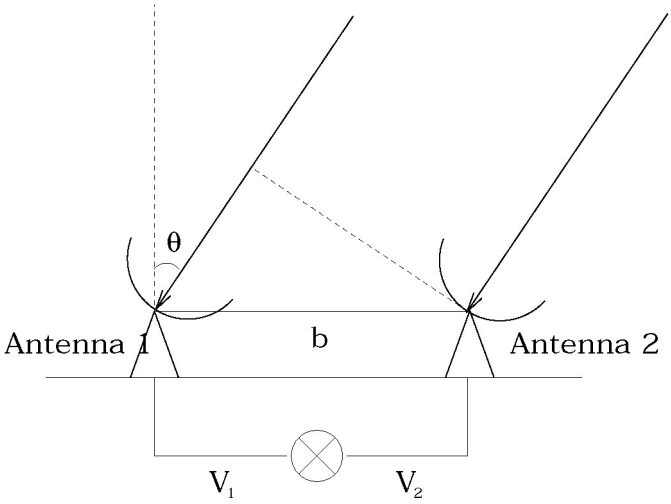

Figure 2.2: An ideal 1-D two-antenna interferometer consisting of two antennas, 1 and 2, separated by a physical distance b, their *baseline*. The antennas are both pointed towards a sky location s_0 which is at an angle θ from the meridian. The projected distance between the two antennas in that direction is $u = b\cos\theta$. The detected voltages of each antenna are bring via cable to a correlator and then combined.

figure 2.2 observe the same source but the signal is received at different times by the two elements; antenna 1 experiences the *geometrical delay* $\tau_g = b\ s_0/c$, where s_0 is the position observed by the antennas and c is the light-speed. Before correlate the signals it is necessary to take into account τ_g, applying an artificial delay to the signal path of the antenna 2. The correlator multiplies and time-averages the signals incoming from the two elements and measures a quantity known as the *the complex visibility*, which is the Fourier transform of the sky brightness distribution B(x,y) (*Cittert-Zernike* theorem):

$$V(u,v) = \int\int B(x,y)e^{2\pi i(ux+vy)}dxdy = V_0 e^{i\varphi} \tag{2.10}$$

$$B(x,y) = \int\int V(u,v) e^{-2\pi i(ux+vy)} du dv \tag{2.11}$$

U and V are the spatial frequency components of the power pattern in the E-W and N-S directions, respectively; they represent the projected lengths of the baselines onto a plane normal to the direction of the source, measured in units of wavelength at the time of the observation;x,y (rad) are the angles in a tangent plane relative to a reference position in the E-W and N-S directions. V is a complex quantity which is described by an amplitude A and phase φ containing information about the source brightness and its location relative to the phase center, respectively. The complex visibility distribution is called the *(u,v)* plane whose Fourier transform gives the sky brightness distribution: the image is a "sum" of the visibilities where each has an amplitude and phase representing the brightness and relative position of emission on a specific angular scale. The power pattern of an interferometric observation is called **synthesized beam**. Each pairs of antennas sample the sky brightness distribution on a scale inversely proportional to the projection of their distance on the sky. The response of the interferometer is sinusoidal (usually called *fringe*) and in the 1-D case, it samples spacing on the sky given by λ/b; the antennas can sample the sky brightness distribution only on the scale defined by the wavelength of the sinusoid. Since the fringe spacing depends inversely on the projected distance, as closer the antenna pair are larger the sampled scales are. Conversely, the signal produced by a distant antenna pair samples smaller angular scales. Furthermore, since the fringe spacing also depends on the wavelength of emission, observing shorter or longer wavelengths can sample smaller or larger angular scales, respectively.
A given pair of antennas will instantaneously sample a single scale of the sky brightness distribution. Given the spatial coordinates of a pair, a visibility in the *uv*-plane is measured. The visibilities are complex functions with Hermitian symmetry so that a single sampling gives two points in the *uv*-plane, (u,v) and its complex conjugate (-u,-v). In order to model the true sky brightness distribution it is necessary to sample as much as possible the *uv*-plane. It can be done using multiple antennas at different distances into an array[3] or increasing the observation time. Due to the Earth's rotation effect, the baselines projection plane change continuously its position relative to the source allowing to sample many visibilities across the *uv*-plane. Furthermore, the antennas can be configured in different ways so that pairs of antennas have different distances and sample different parts of the *uv*-plane, i.e. different angular scales. Figure 2.3 shows an *uv*-plane example.

[3]If N is the number of the available antennas, $\frac{N(N-1)}{2}$ is the number of the baselines, each pair providing a pair of samples in the *uv*-plane.

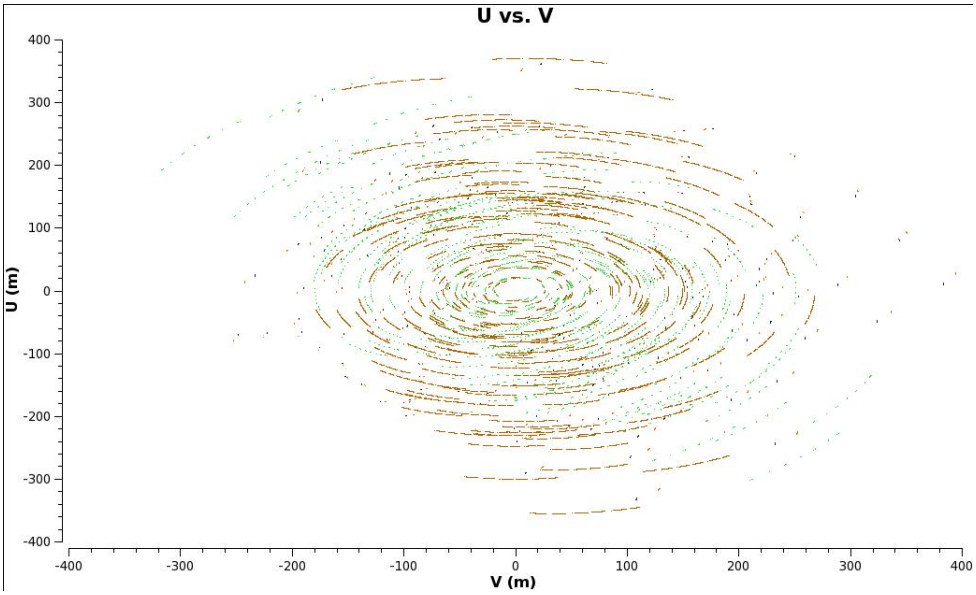

Figure 2.3: Example of *uv*-plane coverage for a typical ALMA observation. The integration time is $\sim$ 46min; u and v are in meter unit. The Earth's rotation leads to the observed "tracks", allowing to sample different angular scales.

2.2.2 Interferometer properties

Angular resolution (Synthesized beam)

The resolution of an image is defined as the compactness of the central feature of the beam, i.e. half its FWBN. In the case of interferometric observations the beam is usually called 'synthesized beam'. Due to the complexity of the beam structure, it is not so easy to measure FWBN, so that the resolution is typically approximated to first order by the FWHM of a Gaussian fit to the central feature of the beam; it depends on how the interferometer antennas are arranged in configurations: a compact configuration gives low resolution since the central beam feature is wide, while an extended configuration gives higher resolution since the central beam feature is narrow. To first order, the resolution provided by an interferometer can be computed as:

$$\theta_{res} = k\frac{\lambda}{B_{max}}[radians] \tag{2.12}$$

where k is a factor that depends on visibilities weighting and B_{max} is the longest baseline in the array.

Field of View (FOV)

The Field of view (FOV) is the angular sensitivity pattern on the sky of each element in the array. In interferometric observations it is usually called *Primary Beam*. The

FOV is typically approximated by a Gaussian whose FWHM is:

$$FOV =\sim 1.13\frac{\lambda}{D}\ [radians] \tag{2.13}$$

where D is the antenna diameter. It sets the field of view of an observation with the array.

Maximum Recoverable Scale (MRS)

Interferometric observations provide highest angular resolution with respect to single-dish observations, but they are insensitive to large angular scales. In fact, the array cannot sample spacial frequencies lower than those that can be sampled by a baseline equal to the antenna diameter; this means that the closest regions of the *uv*-plane cannot be sampled, leading to the so-called *zero-spacing problem*. This lack of sampling on the visibilities plane leads to a lack of information in the image plane, those corresponding to the largest angular structures. The maximum angular scale structure that may be recoverable from an interferometric observation is called **Maximum Recoverable Scale (MRS)** and it can be computed by:

$$\theta_{MRS} \approx 0.6\frac{\lambda}{B_{min}}\ [radians] \tag{2.14}$$

where B_{min} is the minimum baseline of the array configuration. Structures larger than the MRS are 'resolved out' and cannot be recovered in the observation.

Largest Angular Structure (LAS)

The LAS is the largest scale structure of interest in the source to be observed. If the LAS is larger than the MRS, it cannot be recovered by the observations and a more compact array configuration may be required.

2.3 Calibration: an overview

Observed visibilities are "corrupted" by a variety of effects such as the signal processing by the instrument electronics and the transmission through the atmosphere, which cause signal absorption and distortion. Calibration is the process of correcting such effects to make data as close as possible to the ideal ones, measured in vacuum by a perfect system. It is not an arbitrary process and is done in order to provide an accurate picture of the sky when data are imaged.
The relationship between the observed and ideal visibilities on the baseline between antennas i and j may be expressed by the Hamaker-Bregman-Sault *Measurement equation*:

$$\overrightarrow{V_{ij}}(\nu,t) = G_{ij}(\nu,t)\ \overrightarrow{V_{ij}}^{IDEAL}(\nu,t) + noise \tag{2.15}$$

where $\overrightarrow{V_{ij}}$ represents the observed visibilities, $\overrightarrow{V_{ij}}^{IDEAL}$ represents the corresponding ideal ones and G_{ij} represents the combination of all the "corruption" factors related to the baseline *ij*. Most of these effects are antenna-based and are related both to the impact of the atmosphere and to the instrumental response (e.g. Hamaker *et al.* 1996), so that the calibration deal with the temporal gain G and the bandpass response B. This process is simplified because the time-dependent and the frequency-dependent solutions are almost unrelated to each other. In order to estimate such correction factors, calibrator sources are observed, solving the measurement equation for them. Once determined, the antenna-based gain factors are stored in the so-called calibration tables, which are then applied to the data to correct the observed visibilities for the science target.
There are three major stages of calibration:

- **A-priori Calibration.** Calibrations associated with relatively fixed properties of the array which are measured periodically: the estimate of antenna positional errors and pointing models, for example.
- **Online parameters and calibrations.** Measurements of relevant instrumental parameters during the observations, which are made to determine calibration values that can be applied once the data are taken. At ALMA observing wavelengths, it includes measurement of the system temperature (T_{sys}) and of the water vapour emission of each antenna toward the source.
- **Offline calibrations.** Measurements carried out after the completion of the observation, associated to the calibrator sources: the removal of time-dependent and frequency-dependent amplitude and phase corruptions and the conversion of the visibilities amplitude to Janskys flux density unit.

A-priori and Online calibration steps are typical of the ALMA working modes, while the offline calibration could be considered almost the classical procedure done to reduce data from whatever kind of telescope. A brief description of the philosophy of each calibration steps is outlined below.

2.3.1 The WVR and Tsys corrections

At ALMA working wavelengths the Earth's troposphere introduces a large degrading effect on astronomical observations which produces two related phenomena:

1. Absorption of astronomical radiation, re-emitted by incoherent thermal radiation.
2. Delay of the incoming radiation that is variable in time and position.

These effects are directly correlated to the amount of precipitable water vapour (PWV, hereafter) on the atmosphere, which causes the atmospheric turbulence

that leads to record a less accurate signal. The impact of the radiation delay is much stronger on longer baselines and produces a fluctuation in the phase of a visibility recorded by two pair of array elements (e.g. Nikolic *et al.* 2013). Such phase fluctuation produces firstly a de-correlation of the astronomical signal due to its incoherence during the observation and this leads to a reduction of the apparent amplitude of visibilities. Such attenuation can be estimated by 2.16:

$$V_{obs} = V_0 \exp^{-\frac{\varphi_{rms}^2}{2}} \tag{2.16}$$

where V_{obs} are the observed visibilities, V_0 are the intrinsic ones and φ_{rms} is the root-mean-square (rms) fluctuation of phase, also known as **phase noise**. The phase noise could also produce spurious features on images and then leads to a significant reduction of the dynamic range of the maps. Moreover, the totality of these effects can reduce significantly the angular resolution of the observation.
In order to resolve this issue ALMA uses a system of Water Vapour Radiometers (WVR) which samples the water line at 183 GHz to give and estimate of the PWV quantity on the atmosphere during the observation. This sampling allows computing the correction factors for such phase delay.
Directly related to the role of the atmosphere at such frequencies is the system temperature (T_{sys}) correction. The T_{sys} is given by several factors and can be defined as (e.g. Jewell *et al.* 1997, ALMA memo series):

$$T_{sys} = \frac{(1+g)[T_{rx} + T_A(sky)]}{\eta \times \exp \tau_0 \sec z} \tag{2.17}$$

where:

- g represent the ratio of the gain response between the image and the signal;
- T_{rx} is the receiver noise temperature;
- $T_A(sky)$ is the antenna-based temperature of the sky which includes contributions from the atmosphere, antenna response and cosmic microwave background (CMB);
- η is the antenna efficiency, related to the maximum antenna gain and to the antenna power pattern;
- τ_0 is the zenith optical depth of the atmosphere;
- $\sec z$ is the zenith secant which gives an estimate of the number of airmasses at the observing elevation.

All these terms give a negative contributions to the millimeter/sub-millimeter observations, producing signal attenuation and fake absorption lines on spectra due

to the tropospheric emissivity. The T_{sys} correction does not need a calibrator but it is strictly dependent from the elevation of the source and the atmospheric opacity on such direction; it drops exponentially with τ. The T_{sys} is also important to give an estimate of the flux density sensitivity of interferometric array data, also know as **thermal noise**:

$$\sigma = \frac{4\sqrt{2}k_b T_{sys}}{\gamma\epsilon_q\epsilon_a\pi D^2\sqrt{n_p[\frac{N(N-1)}{2}]\Delta\nu\Delta t}}\ W/Hz\ m^2 \tag{2.18}$$

where k_b is the Boltzmann constant (1.38×10^{-23} J/K); T_{sys} is defined as in equation 2.17; ϵ_a is the aperture efficiency; ϵ_q is the correlator quantization efficiency; D is the antenna diameter; n_p is the number of simultaneously sampled polarizations; N is the number of the antennas in the array; $\Delta\nu$ is the bandwidth; Δt is the integration time and γ is the gridding parameter set equal to unity. The T_{sys} also determines visibility weight $\propto \frac{1}{T_{sys}(i)T_{sys}(j)}$, where i and j are the two array elements.

2.3.2 Antenna positional errors

An important requirement in an interferometer is an accurate knowledge of the antenna position. The importance of this determination become essential at ALMA working frequencies for that the tropospheric turbulence play an important role on data phase errors, as explained above. An inaccurate characterization of the array geometry could induces phase delay across the bandpass, especially on longer baselines; to establish a good antenna position is necessary to get a good bandpass calibration. Furthermore it could involves position imprecision on imaging and sources astrometry (e.g. Conway 2004, ALMA memo series). The spatial offset parameters are composed of three values, one for each Cartesian coordinate. In the case of compact array configuration the errors are too small that they can be considered negligible ($\sim 10^{-5}$) and set as zero. Usually only offset parameters larger than 3 mm need to be applied.

2.3.3 Bandpass calibration

The response across each observed frequency ranges will not be flat in amplitude and phase, although the delay errors that produce a large slope of phase versus frequency should have been removed by the a-priori and online calibrations. For each tuning, the residual bandpass correction is determined from a scan of a bright calibrator source with a known radio spectral index (see Section 4.3.4 for details). After removing any significant phase variations over the bandpass scan, the amplitude and phase corrections as a function of frequency are computed and placed in a table. The bandpass response is almost time-independent and extremely stable over all

angles, thus the bandpass determination will not change by more than 0.4% in each run (about an hour); this solutions can be applied to all of the observed data in a single tuning.

2.3.4 Gain calibration (G)

All ALMA observations use the *phase referencing* technique to calibrate the temporal antenna-based variations in amplitude and phase. Such method consists in interleaving scans between the science target and a nearby calibrator source (the so-called *phase calibrator*), whose long-timescales solutions will be then used to calibrate the target visibilities. The larger temporal changes should have been removed with a priori and online calibrations. The plots of the antenna-based amplitudes and phases should be carefully inspected, and some guidelines are: (1) The antenna-based amplitudes should not vary by more than about 10% over the observation period, and differ by more than about 20% among the antennas. For antennas with low gain or drop-outs, it is necessary to check the data quality. (2) The phase difference between adjacent calibration scans should be relatively small. For example, if the antenna-based phase changes between scans exceeds about 60°, applying an interpolated solutions between scans to the target could lead to an imperfect calibration; this usually occurs at longer baselines and higher frequencies.

2.3.5 Absolute Flux Density Calibration

The Calibration of the data using the T_{sys} measurements converts the raw correlation amplitude into Kelvin. The relationship of the correlation units in Kelvin to Jy is called the System Equivalent Flux Density (SEFD), and depends on the antenna diameter and efficiency. The SEFD is very stable with time and similar among the antennas of the same type. In order to derive a more accurate absolute flux calibration scale, a measurement of a source with known flux density and structure is usually included in the observations. The most reliable Kelvin to Jy conversion is obtained observing solar system objects of relatively small angular size that have accurate visibility models versus frequency and baseline length (see Section 4.3.3).

2.4 Imaging process

Once the calibration process is done, the calibrated visibilities are Fourier transformed in order to obtain the sky brightness distribution. As explained above, the limited sampling of the *uv*-plane provide a fundamental limit to the level of detail in the sky brightness distribution and the resulting images do not contain information about the angular scales unobserved by the interferometer. Knowing that the resolving power of an array depends on the measured visibilities distribution, the so-called *sampling function*, S, is defined. It describes the *uv*-plane coverage and

is 1 at locations where visibilities are measured and zero elsewhere. In this way, the true visibilities distribution, which corresponds to an ideal total coverage of the *uv*-plane, is 'filtered' by the sampling function obtaining the observed calibrated visibilities:

$$V^{meas}(u,v) = S(u,v) \cdot V^{true}(u,v) \tag{2.19}$$

The measured sky brightness distribution is obtained by computing the inverse Fourier transform of 2.19, making the so-called **dirty image**:

$$I^{meas} = FT^{-1}(V^{cal}) = FT^{-1}(S) \otimes FT^{-1}(V^{true}) \tag{2.20}$$

where I^{meas} is the measured sky brightness distribution. The inverse Fourier transform of the sampling function is called **dirty beam** (PSF). The gaps in the *uv*-plane sampling, produces aliased features in the resulting image, the magnitude of which depends on the extents and locations of gaps and the brightness of emission on sampled scales. Furthermore, the synthesized beam sidelobes can corrupt the image since the brightness is distributed by the PSF throughout the image. The imaging process consists in improving the dirty image using the **CLEAN** algorithm (Hogbom 1974, Clark 1980, Cotton-Schwab 1984), an iterative method which makes a deconvolution of the 2.20 with the goal of minimizing the effects of the incomplete spatial frequency sampling. As explained above the visibility plane (1) and the image plane (2) are Fourier transform to each other. To make the Fourier transform faster, the two planes are gridded: each element of the grid is spaced Δu and $1/u_{max}$ in the (1) and (2) case and the grid size is u_{max} and $1/\Delta u$, respectively. This involves the choice of a pixel size (i.e. *cellsize*) and an image size (i.e. *imsize*) before start cleaning. Usually the cellsize is chosen 1/5 of the synthesized beam size and the imsize is chosen twice the primary beam size (in order to check for serendipitous sources close to the target). Furthermore, knowing that shorter baseline lengths are usually sampled more than longer ones, a *weighting function*, W(u,v), is associated to each visibility whose choice allows dealing between the image resolution and the sensitivity: the **natural weighting** ($W(u,v) = 1/\sigma^2(u,v)$, where σ is the noise variance of the visibilities) is based on the true density distribution of the visibilities in the *uv*-plane and lead to maximum sensitivity and larger synthesized beam; the **uniform weighting** ($W(u,v) = 1/\delta_s(u,v)$, with δ as the density of visibilities in a uniform region of the *uv*-plane) removes the dependencies of spatial-scale sensitivity on the density of sampled visibilities and lead to higher resolution but less sensitivity. Usually what it is used is a compromise between the two types of weighting, the **Briggs** weighting, which uses a parameter called *robust (r)* allowing variations between *natural* (r=+2) and *uniform* (r=−2).
The **clean** algorithm is based on some a-priori assumptions about the sky brightness distribution: the sky intensity is positive and each source is a collection of point-like sources. Once determined the parameters described above, it is possible to start cleaning; a scheme of the iterative steps made during the clean process are itemized on following:

- Initializes the residual map to the dirty map, and the Clean component list to an empty value;
- Identifies the pixel with the peak of intensity (I_{max}) in the residual map, and adds to the clean component list a fraction of $I_{max} = \gamma\ I_{max}$ ($\gamma \sim 0.1, 0.3$);
- Multiplies the clean component by the dirty beam and subtract it to the residual map;
- Iterates until stopping criteria are reached ($|I_{max}| <$ multiple of the rms (when rms limited); $|I_{max}| <$ fraction of the brightest source flux (when dynamic range limited);
- Multiplies the clean components by the clean beam, which is an elliptical Gaussian fitting of the central region of the dirty beam, and add it back to the residual (restoring).

The resulting image pixels have units of Jy per clean beam.

2.4.1 Self-calibration

Once a first deconvolved model image is computed, a "self-calibration" loop can be performed. Self-calibration is used to refine the target source calibration making its own calibration, rather than using external calibrator source. Usually linear interpolation is done between the averaged per-scan solutions of the phase calibrator, but it is on different position in the sky and its visibilities are carried out at different times with respect those of the target; this could lead to an imperfect calibration of the target. The basic idea is that objects with enough signal-to-noise ratio (SNR) can be used to calibrate themselves to obtain a more accurate image; in general if the signal-to-noise ratio of the image is > 20, it is worth trying phase-only self-calibration. The aim of this process is to get phase errors smaller than 10-20 deg and amplitude errors $< 5\%$, following the regular calibration procedure outlined above. One crucial parameter is the time interval in which computing the solutions: for a given number of antennas, the higher SNR on the image is, the shorter the solution interval can be. Any number of self-calibration loops can be performed. Once computed, the solutions are applied to the data, and a new map is produced; if the noise lowering is $> 50\%$ another phase self-calibration can be done. As long as the images are improved, it is usually prudent to continue the self-calibration iterations.

Chapter 3

The ALMA era

3.1 Introduction

The Atacama Large Millimeter/sub-millimeter array is an aperture synthesis telescope located on the Chajnantor plain of the Chilean Andes at an elevation of about 5000 m and at a latitude of $-23°$ (Fig. 3.1). It operates over a broad range of observing frequencies in the millimeter and sub-millimeter regime and its Early Science Operations started with Cycle 0 in September 2011. Upon completion, ALMA will be composed of 66 high-precision antennas arranged in a series of different configurations: Fifty 12-meter dishes in the 12-m Array and the Atacama Compact Array (ACA), with twelve 7-m antennas and four 12-m antennas used as single-dish (TP Array). The 12-m array is used for sensitive, high resolution imaging; its baselines range from 15 m up to $\sim$ 16 km, allowing to reach a spatial angular resolution as small as 5 milliarcsec (@950 GHz), in the most extended configuration. ACA (or Morita-San Array) has been designed to solve the well-known *zero-spacing problem* and achieve good imaging of sources with emission on angular scales larger than those corresponding to the minimum spacing of the 12-m Array. Its four single-dish antennas provide spatial information samples equivalent spacing of their diameter (12 m), while the 7-m Array baselines range from 9m to 30m, bridging the baseline sampling gap between the 12-m Array and the TP Array.
At mm/sub-mm wavelengths the influence of the "wet" component of the troposphere become important; this causes significant amplitude absorption and phase dispersion. The ALMA site is one of the driest locations on Earth and allows to have the transparency and the stability needed to limit the negative effects of the troposphere on the observations. The large ALMA collective area (6500 square meters) allows to reduce the noise by two order of magnitude with respect any other interferometer and to sample almost instantaneously many spatial frequency. This aspect also allows to reach the best ever sensitivity at these wavelengths.
ALMA enables transformational research into the physics of the so-called '*Cold Universe*', such as dark clouds and star-formation regions which are optically dark

but shine brightly at mm wavelengths. Thanks to its high sensitivity, ALMA allows the study of high-redshift objects, probing the first stars and galaxies and directly imaging the disks in which planets are forming. Its high spectral resolution (~ 3 kHz) is giving a great hand on studying stellar evolution and astrochemistry.
ALMA is an international facility, a partnership between Europe, East Asia and North America, in cooperation with the Republic of Chile. To interface with the geographically distributed user communities, the partners have established the ALMA Regional Centers (ARCs), which provide user assistance with proposal preparation, writing and refining observing scripts, processing and analyzing data. The Italian ARC is located in Bologna-Area della Ricerca (CNR).

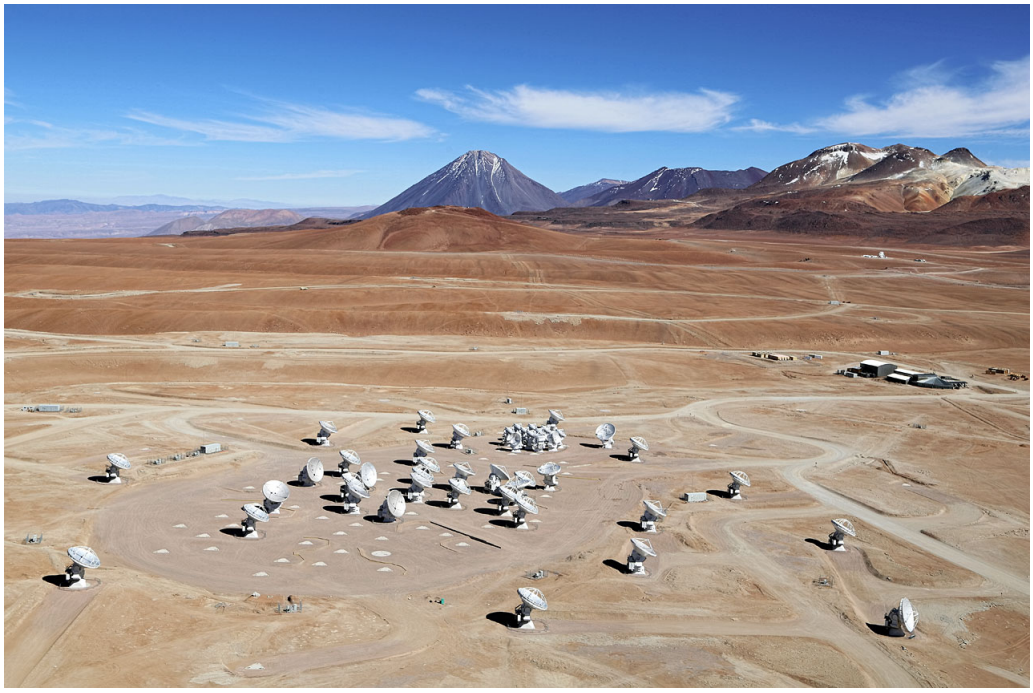

Figure 3.1: Aerial view of the Chajnantor Plateau, the ALMA site, situated in the Chilean Andes at an elevation of about 5000 m and at a latitude of $-23°$.

3.2 ALMA technical specifications

The purpose of this Section is to summarize the instrument characteristic in order to describe the path followed by the signal once it is captured by an ALMA antenna. The signal is first collected by the parabolic antenna and reflected to the focal plane; then it is down-converted at the Front End stage where cryogenically cooled receivers (4 K) are located. Finally the signal from the receivers is digitized by the Back End and transmitted to the Correlator which combines it from couple of antennas. From the correlator, data, additional monitor and weather data are sent

via dedicated optical fiber links (1−10 Gbit/s) to the Operation Support Facility (OSF, located at an elevation of 2900 m), where data are quality-checked and archived.

3.2.1 Antennas

ALMA antennas has been produced by three different contractors: the north American VertexRSI, the European AEM and the east Asian MELCO. Each antenna consists of symmetrical parabolic mirrors composed of individual panels and assembled in a Cassegrain mount; the surface of the panels are etched to scatter optical and near-infrared solar radiation. The receivers are mounted in the secondary focus in a cabin that is kept at a constant temperature of 20° C. The different antennas have been built in metrology systems which allow thermal and wind deformation to be computed and corrected. Their performance criteria are very stringent, e.g. the RMS deviation for the antenna surface has to be 25 μm for 12-m dishes and 20 μm for 7-m; relative pointing accuracy less than 0.6" and absolute pointing $\leq$ 2" all-sky. The antennas are placed on specially-designed pads to guarantee stable orientation and location; their position is measured to a precision of 65 μm and then monitored for stability for over two weeks. The estimated minimum antennas lifetime is 30 years.

3.2.2 Front end and ALMA receivers

The Front End is the analogue part of the receiver. It converts two orthogonally polarized signals into an IF (Intermediate Frequency) of 4 to 12 GHz. All Front Ends are fed with a Local Oscillator (LO) that is optically transmitted over the distance from the center of the array to the antennae. The ALMA frontend can accommodate up to ten receiver bands at its full capabilities, that will cover most of the wavelength range from 10 to 0.5 mm (30 - 950 GHz); actually not all the projected bands are already active. Each receiver band is designed to cover a tuning range which is approximately tailored to the atmospheric transmission windows (Fig. 3.2). The ALMA receivers in each antenna are situated in a large cryostat kept at a temperature of 4 K, that contains the mixer, the IF and LO electronics of each band. Each receiver contains two receiving systems sensitive to orthogonal linear polarizations. Also the Water Vapour Radiometers (WVRs) are placed at frontend-stage in each antenna (See Section 2.3.1 for details).

3.2.3 Local oscillators and IF system

The observed sky frequencies need to be down-converted to frequency bands between 0-2 GHz in order to send the signals to the correlator. This down-conversion involves the LO and IF system, used to define the spectral setup for the user. At the first stage the signal is down-converted to 4/8 GHz-wide IF bands, the so-called

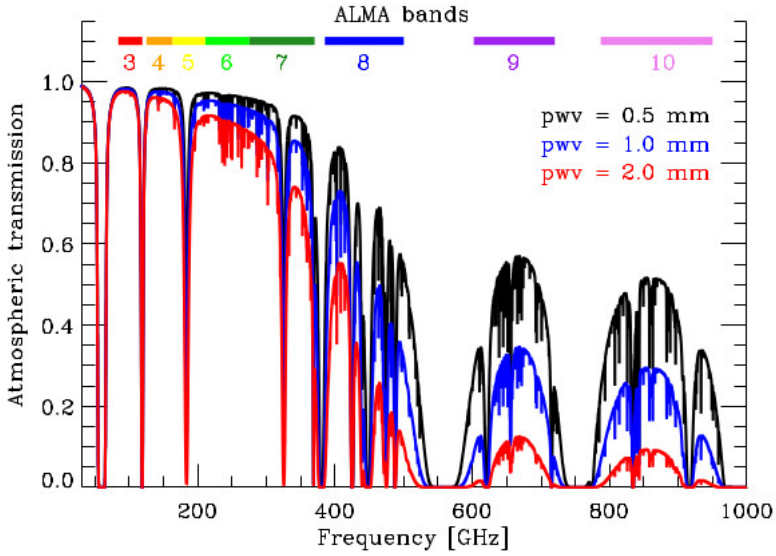

Figure 3.2: Atmospheric transmission curves at Chajnantor Plateau (ALMA site) for different amounts of precipitable water vapour. The horizontal colored bars represent the frequency ranges of the ALMA bands.

upper sideband (USB) and *lower sideband* (LSB). Using the second stage of down-conversion, up to four 2-GHz wide *Basebands* (BBs) can be placed in either or both the USB and LSB. Within each of this basebands it is possible to place, in principle, up to 32 spectral windows (SPWs), even if usually not more than four SPWs per baseband are used. Each SPW forms a contiguous spectrum with bandwidths up to 1.85 GHz-wide and is divided into several channels whose number depends on the correlator operating mode, requested to reach a certain spectral resolution. A schematic view of the ALMA IF system is shown in figure 3.3.

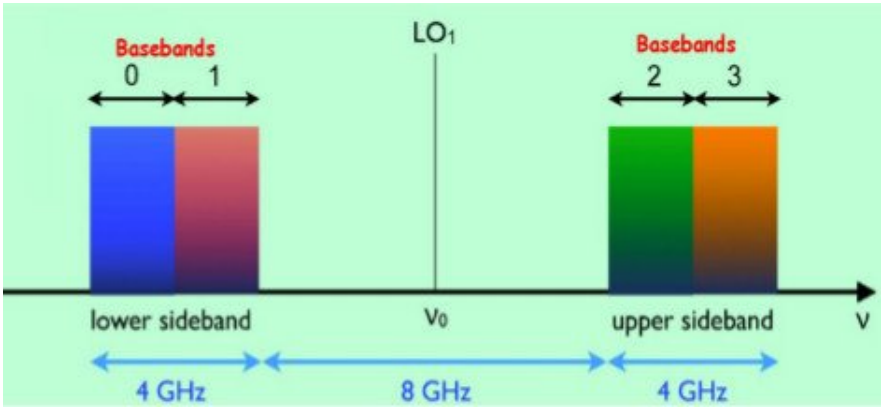

Figure 3.3: Schematic view of ALMA LO and IF system. Basebands may be tuned to overlap or may be located so as to maximize the total bandwidth. Each baseband may be further subdivided into as many as 8 spectral windows.

3.2.4 Back End and Correlators

A correlator is a virtual focal plane of an interferometer array. It receives signals from individual antennas, calculates cross-correlations and auto-correlations for each antenna pair and produces complex visibilities that users will reduce to synthesize images. Once the astronomical signal is down-converted to lower frequencies and the spectral setup is defined, these analog signals are sampled, quantized in digitizers and then transferred via cable to the correlator. The specifications of the correlator determine a lot of observational performance such as bandwidth, spectral resolution, time resolution and polarimetry; imperfect correction for the response in the correlators invokes systematic errors in complex visibilities. The correlator works in two basic modes, Time Division Mode (TDM) and Frequency Division Mode (FDM). TDM provides wide bandwidth and low spectral resolution for mainly continuum observations; FDM is usually used in the case of spectral-line based observations allowing an high spectral resolution.

3.3 ALMA Cycle 0 capabilities

The data analyzed in this Thesis work were carried out during ALMA Early Science Cycle 0 program. During Cycle 0 the whole array was on Science Verification phase so that only a limited number of antennas, frequencies, array configurations and observing modes were available. Table 3.1 summarizes Cycle 0 capabilities for the four available Bands (3,6,7,9). Cycle 0 started on September 30, 2011 and finished on June 30, 2012. The available antennas were all from the 12-m Array in a limited number ($\sim$ 16). During the Early Science data were usually reduced by an expert analyst with CASA version 3/3.2 (see Section 4.2). The caveat is to reduce ALMA archival Cycle 0 data using the last CASA version, checking for the reliability of the calibration, in order to obtain good final products[1].

[1] https://help.almascience.org/index.php?/Knowledgebase/Article/View/161/0/

Table 3.1: ALMA Early Science Cycle 0 Capabilities*

Band	ν **(GHz)**	λ **(mm)**	**Angular Resolution**(1) **(")**	**Maximum Scale**(2) **(")**	**Field of View**(3) **(")**	**5σ continuum sensitivity in 1 hour**(4) **(mJy/beam)**	**3σ line sensitivity in 1 hour**(5) **(K) per 1 km/s**
Properties of Compact Configuration (baseline ∼18 m to ∼ 125 m)							
3	84-116	2.6-3.6	5.3	21	62	0.65	0.030
6	211-275	1.1-1.4	2.3	9	27	1.0	0.029
7	275-373	0.8-1.1	1.55	6	18	1.8	0.043
9	602-720	0.4-0.5	0.8	3	9	15	0.27
Properties of Extended Configuration (baseline ∼36 m to ∼ 400 m)							
3	84-116	2.6-3.6	1.56	10.5	62	7.6	0.35
6	211-275	1.1-1.4	0.68	4.5	27	11	0.34
7	275-373	0.8-1.1	0.45	3.0	18	20	0.50
9	602-720	0.4-0.5	0.23	1.5	9	175	3.1

*All these values are estimated basing on simulations and modelling together with test data. The uncertainty concerns especially the sensitivities; for most up-to-date values, it is recommended the use of the ALMA sensitivity Calculator[2].
(1) The FWHM of the synthesized dirty beam
(2) Is the largest angular scale that can be effectively observed.
(3) The nominal field of view (FOV) for single-field interferometry. It is close to the FWHM of the primary beam.
(4) The five-sigma continuum flux sensitivity in mJy/beam for a 1-hour observation.
(5) The three-sigma spectral-line brightness temperature sensitivity in Kelvin for a 1-hour observation, with 1 km/s as spectral resolution.

3.4 ALMA full capabilities

Still upon completion, ALMA will be an incredibly powerful instrument at its full capabilities stage. Up to ten receiver bands will be available, covering a wavelengths range from 3.5 mm to 300 μm (84−950 GHz), with possible extension to 10 mm (30 GHz). The instrument will work in full Stokes polarimetry, and it will work with up to 2016 baselines simultaneously. The expected ALMA full capabilities performances are summarized in table 3.2.

Table 3.2: ALMA full array capabilities

						Compact		Extended	
Band	ν **(GHz)**	λ **(mm)**	**Field of View**(1) **(")**	**Largest Scale**(2) **(")**	**Continuum Sensitivity**(3) **(mJy/beam)**	**Angular resolution**(4) **(")**	**ΔT_{line} (K)**(5)	**Angular resolution**(6) **(")**	**ΔT_{line} (K)**(7)
1†	31.3-45	6.7-9.5	145-135	93	†	13-9	†	0.14-0.1	†
2†	67-90	3.3-4.5	91-68	53	†	6-4.5	†	0.07-0.05	†
3	84-116	2.6-3.6	72-52	37	0.05	4.9-3.6	0.07	0.05-0.038	482
4	125-163	1.8-2.4	49-37	32	0.06	3.3-2.5	0.071	0.035-0.027	495
5	163-211	1.4-1.8	37-29	23	*	*	*	*	*
6	211-275	1.1-1.4	29-22	18	0.10	2.0-1.5	0.104	0.021-0.016	709
7	275-373	0.8-1.1	22-16	12	0.20	1.5-1.1	0.29	0.016-0.012	1128
8	385-500	0.6-0.8	16-12	9	0.40	1.07-0.82	0.234	0.011-0.009	1569
9	602-720	0.4-0.5	10-8.5	6	0.64	0.68-0.57	0.641	0.007-0.006	4305
10	787-950	0.3-0.4	7.7-6.4	5	1.2	0.52-0.43	0.940	0.006-0.00	-

†To be developed in future.
*avaliable on a limited number of antennas.
(1)-(2)-(4)-(6) Refer to table 3.1.
(3) The continuum expected sensitivity for a 1-hour observation estimated by simulations.
(5)-(7) The brightness temperature sensitivity, for 1-hour observation with a 50-antenna array arranged in 'compact' or 'most extended' configuration.

3.5 The ALMA archive

An observing proposal submitted to the ALMA archive will have an associated structure, the so-called *Observing project*, organized and subdivided into a well defined structure with clear hierarchical levels (fig. 3.4). Observations are divided

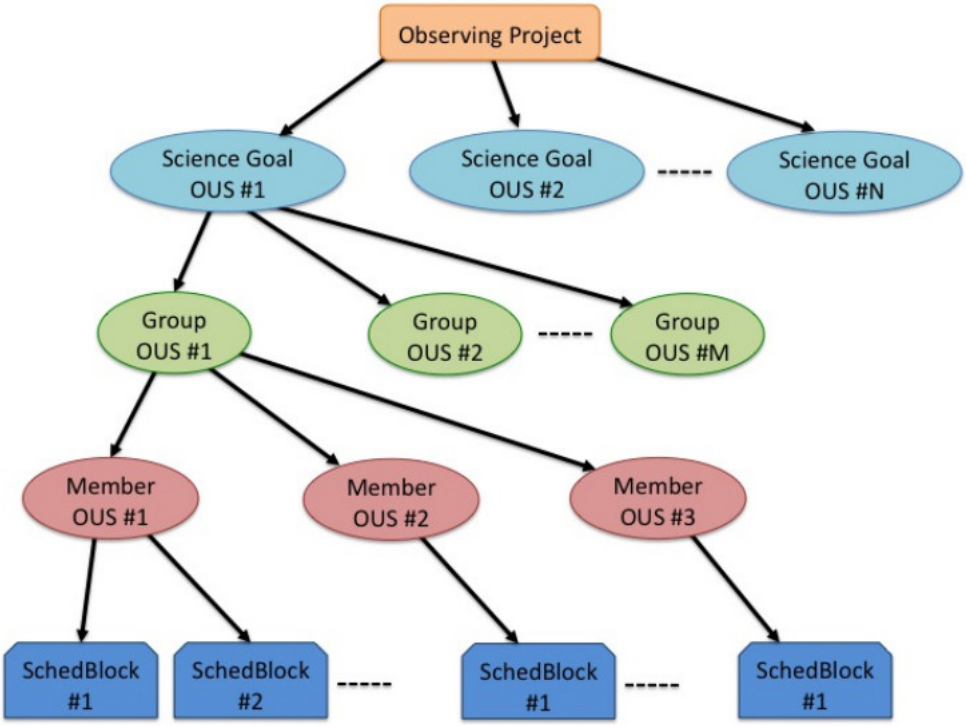

Figure 3.4: Block diagram of an Observing Project. All projects have the same Observation Unit Set (OUS) level, the Science Goal OUS level, the Group OUS level and the member OUS level. Scheduling Blocks are attached to the Member OUS. Each time a Scheduling Block is executed, a new Execution Block stucture is created (see text for details).

into *Science Goals (SG)* which represent the minimun proposed observational unit including targets in the same sky positions that roughly share the same calibration, spectral setup and PI requests (i.e. sensitivity, angular resolution, largest angular scale). Each SG is converted into *Scheduling Blocks (SB)*, the mininum observational unit including targets in the same sky region and their calibrators to be observed with the same instrumental setup; they are the minimum set of instructions to perform an observation and different configuration cannot stay in the same SB. The current maximum time for an SB is chosen based on statistical measurement about the stability of the system, so that executing SBs for more that two hours become unsafe in this sense. A SB that needs to be repeated to reach the requested sensitivity, could be divided into *Execution Blocks (EB)*. The EB is the

minimum observing unit and the minimum data reduction unit; it is also the minimum archive unit. Each EB is carried out by breaking it down into scans, subscans and integrations, the time at which the signal is effectively recorded by the antenna. If the SB is the smallest entity used for observing, the *Observing Unit Set* (OUS, hereafter) is the smallest unit for data processing. A **GROUP OUS** (GOUS) can contain several configurations to be combined in data processing; each observation with a different array configuration would be in separate *MEMBER OUS* (MOUS), but in the same GOUS. A MOUS can contain multiple executions of a SB and is the minimum scheduling entity. The SB/MOUS/GOUS are the smallest structures that hold science observations that need to be observed/processed/combined together to produce calibrated science products. ALMA data are archived in the ALMA Science Data Model (ASDM) format, which contains the meta-data (headers, description of the observation setup, etc) and the binary data (raw visibilities). The first step of any data processing is importing the ASDM in the format suitable for the CASA software (See Section 4.2 for details), the so-called Measurement Set (MS) whose table-based structure contains most (not all) of the information hold in the ASDM.
Once downloaded from the archive and untarred, data are structured into several directories and sub-directories following the ALMA data hierarchy described above (fig. 3.5). (1) is a text file containing information about the achieved beam and

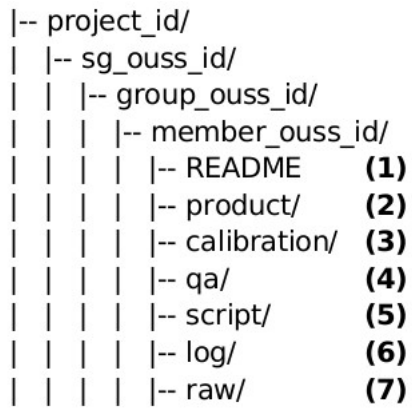

Figure 3.5: Directory tree of an ALMA data delivery. Items 1 to 6 are delivered in one package which should be downloaded first. Item 7 is avaliable for download separately.

image noise RMS and explaining the structure of untarred files; it may contain specific caveats about the observation. (2) consists of some imaging products made to check for the PI requests (e.g. angular resolution, rms, line detection); they cannot be considered science-ready, but only as a starting point. (3) contains calibration (Tsys, WVR, Bandpass, Gain, Amplitude) and flagversion tables; (4) includes the Quality Assurance (see the next section) documentation in the form of plots and text files, in order to check for the quality of calibrated data. (5) consists of data

reduction scripts (one for each EB, if present); (6) contains the CASA log files. (7) (if downloaded) includes raw data. Cycle 0 was the unique in which calibrated MS were archived together with the data products. Two MS are stored in Cycle 0 archival packages: the so-called raw MS with the T_{sys} and WVR corrections applied (in the *raw* directory) and the fully calibrated MS (in the *calibrated* directory). The ASDMs are not in the package but they are available upon request. For Cycle 1 and later it is possible to download only the products file which not contains the raw data.

3.5.1 Data Quality Assessment

ALMA performs science-goal-oriented service data analysis, the so-called Quality Assurance (QA). The QA goal is to ensure that a reliable final data product is delivered to the PI, checking that the product has reached the desired control parameters outlined in the SG, that it is calibrated to the desired accuracy and it is free of calibration or imaging artifacts. ALMA QA has been divided into several stages that mimic the main steps of the data flow; it mainly happens on four levels:

- **QA0:** near-real time verification of weather and hardware performances carried out on each EB immediately after the observation.
- **QA1:** verification of longer-term performance parameters and telescope properties like absolute pointing and flux calibration.
- **QA2:** offline full calibration and imaging of completely observed MOUS. It is performed by expert analyst with the help of semi-automatic procedures; calibration can be manual or based on the pipeline (even for Cycle 0), imaging is usually manual and all this procedures are limited to verify the achievement of the PI requests for each MOUS. QA2 results are archived (as explained above).
- **QA3 (optional):** it is done upon PI request due to issues found after data delivery and could leads to data re-reduction or possibly re-observation.

Errors introduced by users supplied parameters, such as astrometry issues, incorrect redshift or inadequate sensitivity limits are outside the scope of the QA.

Chapter 4

IRAS 00183-7111: reduction of archival ALMA data

4.1 Introduction

In this Thesis work archival ALMA data of IRAS 00183-7111 (I00183) have been reduced and analyzed; data were taken into different frequency Bands: ALMA Band 3 ($\sim$ 87 GHz) and Band 6 ($\sim$ 270 GHz). The observations were carried out during ALMA Cycle 0 Early Science program. Data re-processing is strongly suggested for Cycle 0 observations mainly because new flux model libraries were released after the archival data reduction, providing a more reliable flux calibration[1]. Moreover, during the Cycle 0 program the whole array was on a testing phase and this could lead to find instrumental problems on recorded data.
As explained in Section 3.4, ALMA Cycle 0 archival projects are delivered with automatically generated python scripts for calibration, raw data, some imaging products and calibrated data. The main work of this Thesis was to generate new reduction scripts to be compared with the archival ones and to process raw data (starting from the ASDM format) in order to probe the archival data reduction and provide an improvement, where possible. The analysis was carried out using the Common Astronomy Software Application (CASA), version 4.3.1. In the following sections data properties and the steps followed to reduce them are presented, focusing on calibration issues and the peculiarity of some dataset.

4.1.1 The CASA software

The Common Astronomy Software Application (CASA) is a package developed with the primary goal of reducing interferometric data from the last generation of

[1] see in https://help.almascience.org/index.php?/Knowledgebase/Article/View/161/0/

radio telescope such as ALMA and EVLA[2]. CASA software, which is still under development, has a C++ core with an iPython interface which works in the form of a set of data reduction tasks. The software could reduce, in principle, any kind of interferometric data using a tool which converts the output data format of whatever radio telescope in the CASA data format, the so-called MEASUREMENT SET (MS, hereafter). The MS has a table-based structure: there is a principal table, called MAIN, which is structured into several sub-tables that contain auxiliary information about the observation (e.g. sources, pointing, atmosphere, antennas). Each table or sub-table appears in form of directory on disk. The MAIN table is divided into several columns: the DATA column, which contains the information about the raw visibilities and will never be over-written; the "Scratch Columns" that are filled with the modification to the raw data, such as CORRECTED DATA (containing the calibrated data) and MODEL, which holds the information about model visibilities.

4.2 Observations

The sample is composed of three Scheduling Block (SB, see Section 3.4) divided into two bands: one observed in Band 3, and two in Band 6. Data properties are described below.

4.2.1 The band 3 data

The Band 3 data consist of three Execution Blocks (EB, see Section 3.4) which were observed between 18 and 31 December 2012. The spectral configuration is the same for each one of them: 4 SPWs of 128 channels each with 87 GHz as the representative frequency; the total bandwidth is 1875 MHz ($\sim$ 6474 km/s), while the width of a single channel is 15.6 MHz ($\sim$ 45 km/s). The sky frequency coverage is $86.1 - 87.8$ GHz for the lower SPWs, $96.2 - 97.7$ GHz for the upper ones, as shown in figure 4.1. The runs were performed with 24/25 12-m antennas arranged in a compact configuration, with baseline lengths ranging from 15 m to 400 m; the achieved resolution is $\sim$ 1.85 arcsec. The bandpass calibrator is the bright QSO J2225-049, the phase calibrator is J2157-694. The amount of Precipitable Water Vapour (PWV) varies from $\sim$ 2 to $\sim$ 3.5 mm in each run, while the recorded System Temperature (T_{sys}) is 70 K, on average. A representative Band 3 antenna configuration is shown in figure 4.2.

[2]The Extended Very Large Array is an interferometric telescope composed of 27 antennas of 25 m located in Socorro, New Mexico. It works mostly on cm-wavelengths

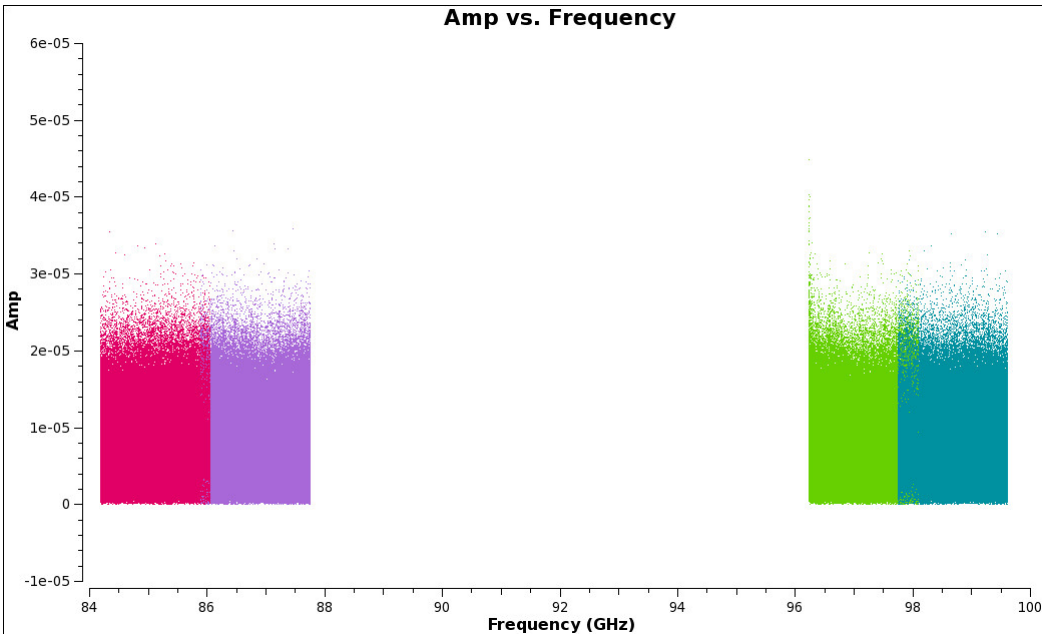

Figure 4.1: Representative Band 3 sky frequency coverage in GHz. Different colors for different SPWs.

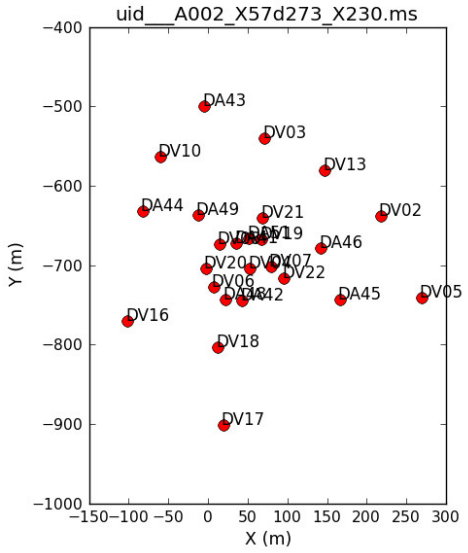

Figure 4.2: Representative Band 3 antenna configuration. Distances are in meters. Each red dot represents an antenna whose ID is labelled close to it.

4.2.2 The band 6 data

Band 6 observations are divided into two MOUS (see Section 3.4) of 4 EB each that were observed between 26 November 2011 and 23 January 2012. The spectral configuration of the two observation groups is different:

- **MOUSS 1:** 273 GHz (Representative frequency); 2 SPWs, 3840 channels each; 1875 MHz is the total bandwidth (2074 km/s), 0.98 MHz the channel width (1 km/s). The covered sky frequency range is $257.2 - 259.11$ GHz in the lower SPW and $272.35 - 274.22$ GHz in the upper one.
- **MOUSS 2:** 268 GHz (Representative frequency); 4 SPWs, 3840 channels each; 1875 MHz is the total bandwidth and 0.98 MHz the width of a single channel. The sky frequency coverage is $253.3 - 255.2$ GHz for the lower SPWs and $266.2 - 267.8$ GHz for the upper ones.

A representative plot of the Band 6 sky frequency ranges is shown in figure 4.3, where the different colors represent different MOUS. Figure 4.4 shows a representative Band 6 antenna configuration. For all the EBs, the bandpass calibrator is 3c454.3 and the phase calibrator J2157-694. Each run was performed with a maximum number of 18 12-m antennas arranged in a compact configuration, with baselines ranging from 18 to 269 m (201 in some case); the achieved resolution is ~ 0.85 arcsec. The amounts of PWV range from 1.15 to 4.2 mm for the eight EBs, while the average T_{sys} varies from 100 to 150 K.
The observations properties in the two Bands are summarized in table 4.1, where each run is indicated with its archival identificative name.

Table 4.1: Properties of the ALMA Cycle 0 observations used in this work

EB(1)	**Observation date**	**Time on target**(2)	**Flux calibrator**	**PWV**(3) **(mm)**	**Tsys**(4) **(K)**	**# antenna (12 m)**
Band 3 observation properties (baselines from 15 to ∼400 m)						
X8e	18/12/2012	45.9 min	Neptune	3.4	70	25
X230	18-19/12/2012	16.1 min	Callisto	3.6	70	25
X11e1	31/12/2012	16.1 min	Neptune	1.9	60	24
Band 6 MOUS 1 observation properties (baselines from 18 to ∼ 270 m)						
X1bc	29/12/2011	31.4 min	Neptune	1.15	100	14
X4f	13/01/2012	31.4 min	Neptune	1.6	110	17
X69	23/01/2012	27.22 min	Neptune	2	110	17
X1e1	23/01/2012	27.22 min	Neptune	2.2	130	17
Band 6 MOUS 2 observation properties (baselines from 18 to ∼ 270 m)						
X570	26/11/2011	24.7 min	Callisto	1.5	100	18
X60	28/11/2011	23.8 min	Neptune	2	110	14
X1c7	10/01/2012	24.7 min	Neptune	4.2	170	17
X1b8	13/01/2012	24.7 min	Neptune	3.3	150	17

(1) Identificative archival name of each Execution Block.
(2) Total integration time on the science target.
(3) Median amount of Precipitable Water Vapour (PWV) quantified during the observation time.
(4) System Temperature median value recorded in each run.

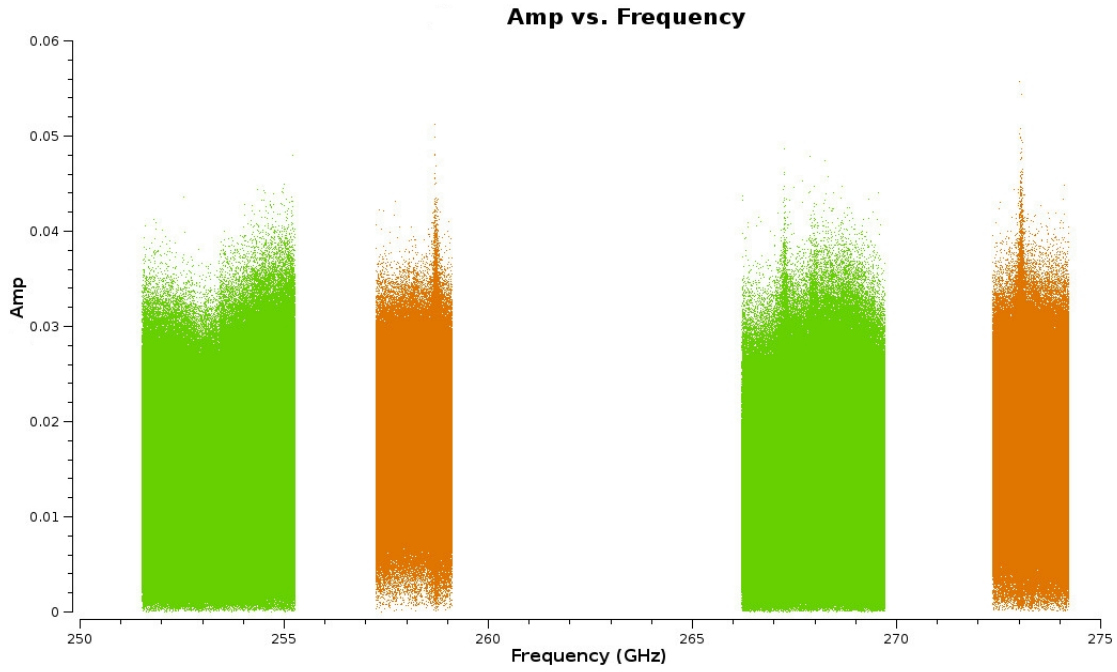

Figure 4.3: Representative Band 6 sky frequency coverage in GHz. Orange and green points indicate the MOUS 1 and MOUS 2 data, respectively.

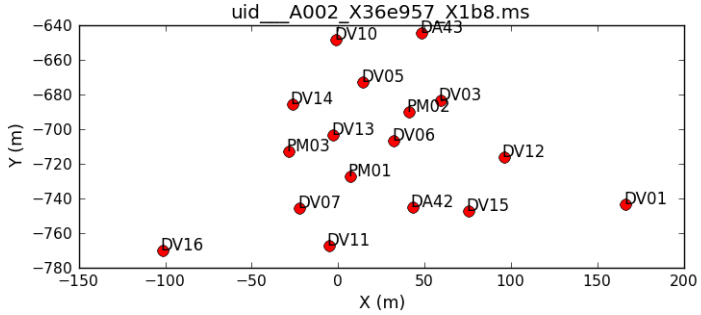

Figure 4.4: Representative Band 6 antenna configuration. Distances are in meters. Each red dot represents an antenna whose ID is labelled close to it.

4.3 The calibration workflow

The main steps of data reduction, the so-called offline calibration procedure (see Section 2.3), can be listed as on follow:

1. Data Import, initial inspection and editing (also known as flagging);
2. Water Vapour Radiometer (WVR) and System Temperature (T_{sys}) corrections;
3. Model information setting;
4. Frequency-dependent calibration;
5. Time-dependent calibration;
6. Flux density calibration;
7. Application of the calibration tables, data examination and further flagging (if necessary);
8. Imaging.

The packages downloaded from the archive include automatically generated python scripts for basic data reduction and datasets whose calibration was performed using previous versions of CASA software (3.2-3.4). In this work, new reduction scripts were generated using the 4.3.1 release of CASA, and changes to them were applied in order to take into account the peculiarity of each EB and provide an improvement with respect the archival results, wherever possible. Furthermore, CASA software is still in development, so that latest releases could use different procedures with respect to the previous one; for this reason, generating new reduction scripts and re-reducing data using the last CASA version is a careful choice, especially for Cycle 0 data. In the following sections, the offline calibration steps outlined above will be briefly discussed and the obtained check plots analyzed.

4.3.1 Data import, initial inspection and flagging

The work started from raw data stored on the ALMA ASDM format (see Section 3.4); using CASA task **importasdm** they were converted into the standard CASA visibility format, the Measurement Set (MS).
Data editing, also know as flagging, consists on removing from data the spurious fluctuations due to instrumental problems that cannot be solved by the calibration. There is also a group of initial flags, which can be done without any visual data inspection, such as:

- **Shadowing:** consists on the blockage of the aperture of an antenna caused by the shadow of a nearby antenna.

- **Autocorrelations:** represent the combination of the signal of each antenna with itself. Autocorrelations are flagged because of their high noise.

- **Pointing and Atmosphere:** consist on the scans performed to check the pointing precision and for the atmosphere calibration. They are unnecessary for the offline calibration purpose.

- **Edge channels:** represent the edge channels of each SPWs. They are always noisier than the central channels of the bandpass, thus they are usually flagged in all SPWs.

4.3.2 Water Vapour Radiometer (WVR) and System Temperature (T_{sys}) corrections

At ALMA's working wavelengths, the Earth's troposphere introduces significant degrading effect on the observed visibilities, such as phase fluctuation and amplitude absorption (see Section 2.3.1). In order to improve data for the atmospheric corruptions, the WVR and T_{sys} calibration steps are executed.

WVR correction

The WVR calibration corrects the observed visibilities for the phase variations on short timescales related to the amount of PWV during each run. The phase variation is larger on longer baselines, especially in presence of high amount of PWV. At this step, the WVR calibration table is generated basing on the information recorded by the radiometer each second during the observation and stored in the MS. Figure 4.5 shows how the *phase versus time* plot of a single baseline should appear before (upper panel) and after (lower panel) the application of the WVR correction: the phase spread has to be reduced when the WVR correction is on.

Wrong WVR correction

The WVR calibration goal is to reduce the observed phase scatter caused by the atmospheric turbulence. In one Band 3 EB (X230) it was found that the application of the WVR correction leads to the opposite result, as shown in figure 4.6. The panels display data for one baseline and one scan of the phase calibrator before (upper panel) and after (lower panel) the application of the WVR correction: the phase fluctuation is clearly enhanced in the lower panel. Since the WVR calibration did not give the expected results, it was decided to not apply the WVR calibration table to the whole dataset.

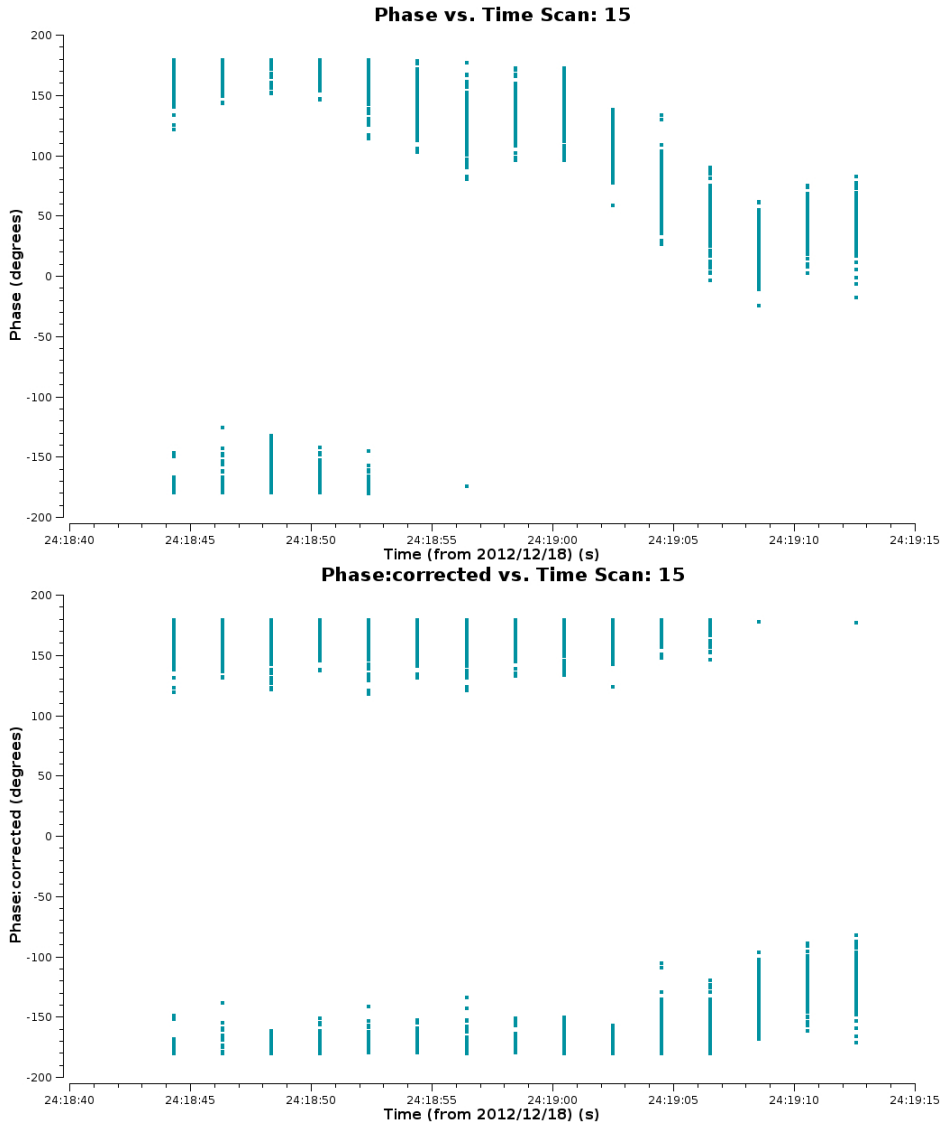

Figure 4.5: **Phase vs time** before (upper panel) and after (lower panel) the application of the radiometer correction. Data refer to one scan in one SPW, and each group of points refer to single integration time. These figures clearly show how the phase spread decreases after the application of the radiometer correction.

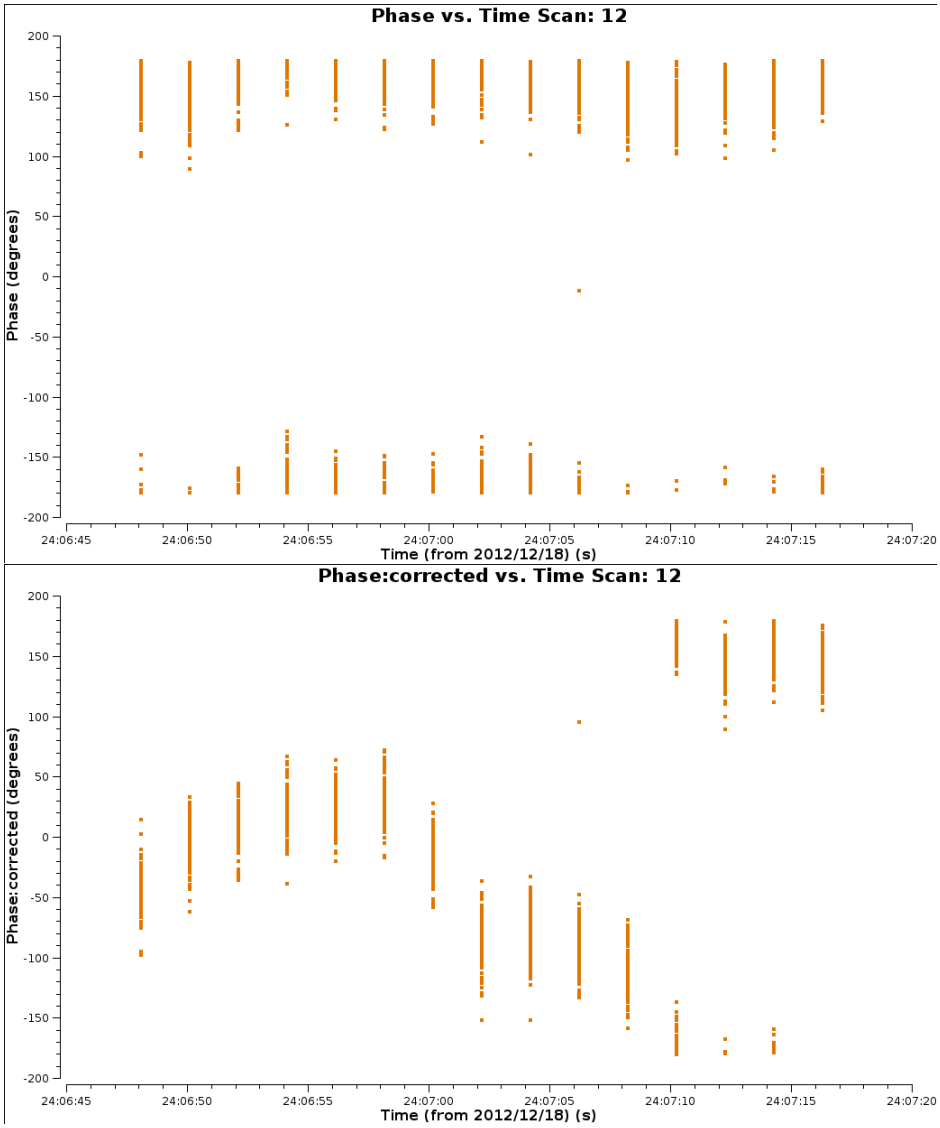

Figure 4.6: **phase vs time** data raw (upper panel) and corrected for the radiometer (lower panel). Data refers to one scan, and each group of points refers to single integration time. In this unusual case, the phase corruption increases after the application of the WVR correction (lower panel).

$\mathbf{T}_{sys}$ correction

The T_{sys} calibration corrects for the effects of the atmospheric opacity which produces signal attenuation and fake absorption lines on spectra. Once the T_{sys} gains are computed, it is useful to inspect them to check for the presence of atmospheric emission features and unusual antenna-based trends. Figure 4.7 shows an example of T_{sys} gains as a function of frequency (in GHz) for one antennas in one SPW; in this case, an atmospheric emission line can be seen at $\sim$ 273 GHz. This atmospheric feature yields to a fake absorption line in the data, as shown in the upper panel of figure 4.8. Once the T_{sys} correction is applied (lower panel of fig. 4.8), the absorption is corrected but a higher dispersion appears due to the low signal-to-noise ratio at the atmospheric line frequencies. Furthermore, the amplitudes scale increases when the T_{sys} correction is on.

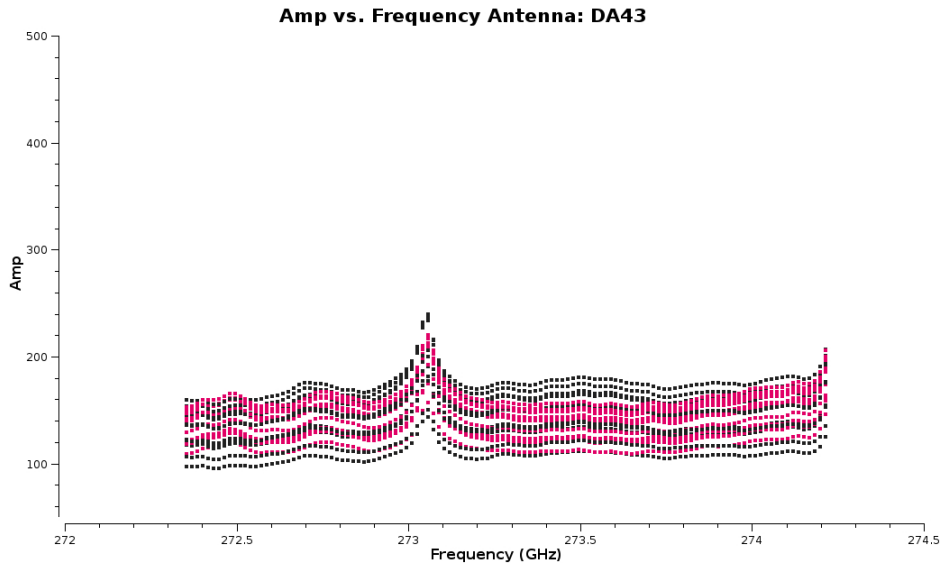

Figure 4.7: T_{sys} versus frequency check plot for one antenna in one SPW. T_{sys} values are in K, frequency are in GHz; different colors are for different polarization products (i.e. XX or YY). Inspecting these plots is necessary to check for possible atmospheric emission line (as in this case), or unusual trends.

Missing $\mathbf{T}_{sys}$ information

The Band 3 archival report notifies an instrumental problem on the T_{sys} measurement at the time of the observations. There is not a specific information about the origin of this problem, but for this reason only channel averaged T_{sys} information were available. However, in the observed frequency range, the atmospheric transmission curve does not shows significant atmospheric features (fig. 4.9), thus the lack of T_{sys} spectral information could not lead to data corruptions in this case.

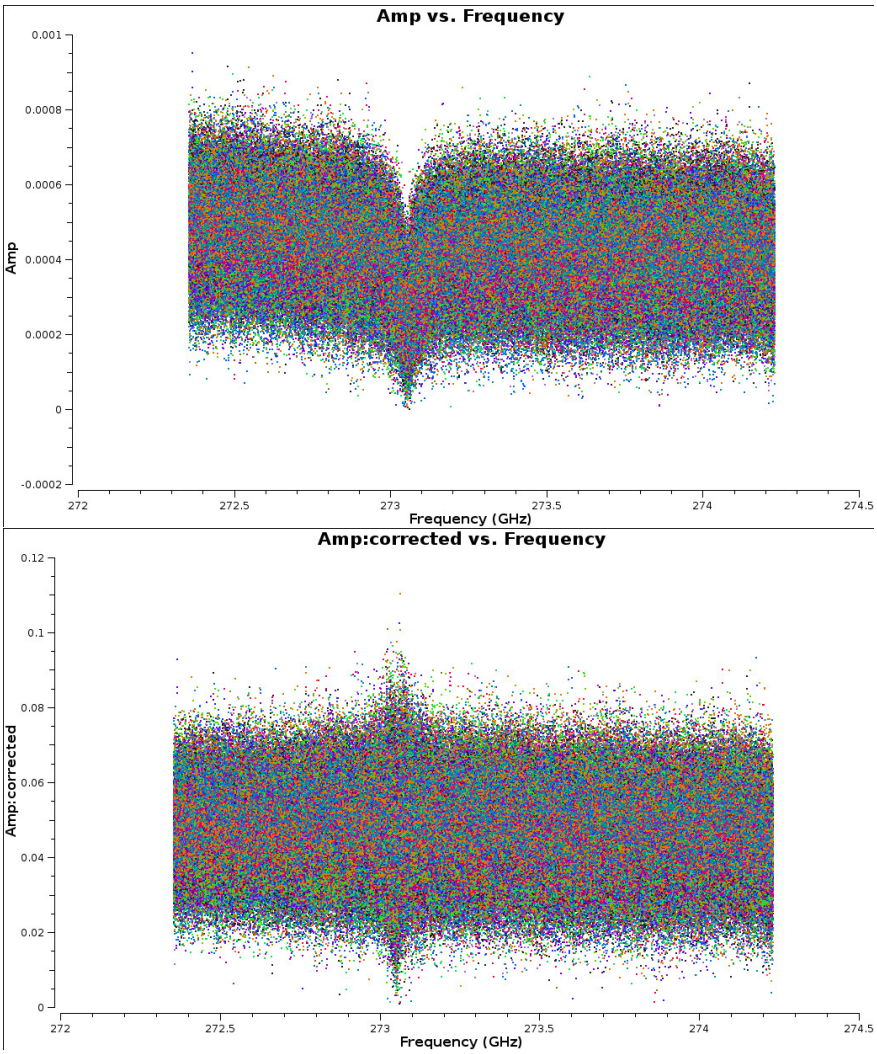

Figure 4.8: **Amplitude vs frequency** before (upper panel) and after (lower panel) the application of the T_{sys} correction. Different colors for different baselines; all times are averaged. The fake absorption line due to an atmospheric emission line is corrected after the application of the T_{sys} calibration table; at this place, higher amplitudes appears (the signal-to-noise ratio is very low at the atmospheric line frequencies). Also the flux scale changes once the T_{sys} correction is applied.

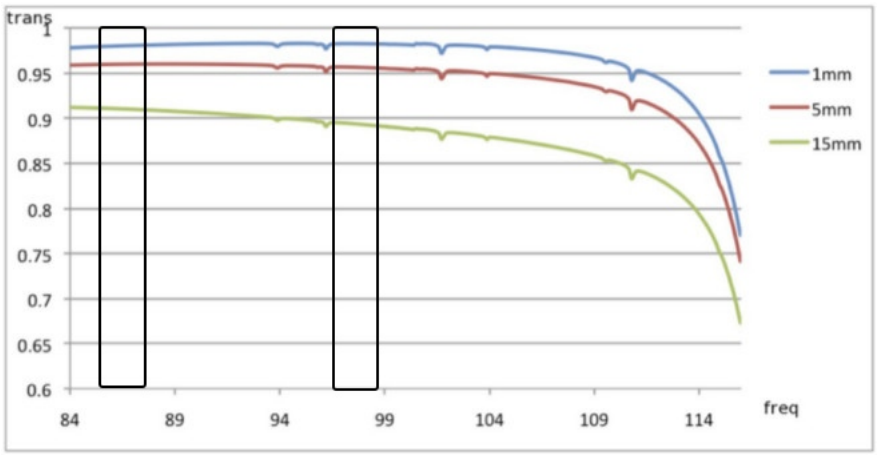

Figure 4.9: Band 3 atmospheric transmission curve for different amount of PWV (1, 5, 15 mm). Frequency is in GHz. The frequency ranges of the observations are highlighted in the boxes. A typical amount of PWV in Band 3 EB is ~ 1 mm.

4.3.3 Model information setting

This step consists on setting the model amplitude and phase visibilities of a specified source (a calibrator) using the CASA task **setjy**. It fills the Model column of the MS with the information of a source with well-known flux density and/or model. For recognized flux calibrators the task automatically calculates the flux density as a function of time, frequency and baseline length. At mm-wavelengths quasars have a very variable flux density, thus extended solar system objects, such as planets and moons, are usually used as flux calibrators. Their models are stored on *Butler-JPL-Horizons* stardards where such objects are modeled as uniform temperature disks based on their ephemerides at the time of the observation (this may oversimplify objects, in particular asteroids).

The flux model problem

In order to check for model setting, a model Amplitude versus UVdistance (i.e. the increasing baseline length for each antenna pair) plot is produced after running this step. Inspecting these plots, a difference was found in the obtained flux density scale with respect to the archival one. The difference is about of 20% when the reference solar system object is Callisto and it is approximately 8% when the flux calibrator is Neptune. Figure 4.10 shows how the Callisto model scale appears in the two cases: the data plotted are for the same SPW in the archival (green curve) and the actual (purple curve) model setting. The difference is attributed to the catalog versions used to set the flux model: in this work the *Butler-JPL-Horizons 2012* was used, while the archival flux model was set using the 2010 release. The two versions adopt a different method on computing the brightness temperature (T_b,

hereafter) of the solar system objects (see Butler 2012, ALMA memo series). In particular, the previous models for moons, e.g. Callisto, were hold using a constant T_b on the basis of Moore (2004). Figure 4.11 shows the T_b model curve as a function of frequency for Callisto (left panel) and Neptune (right panel).

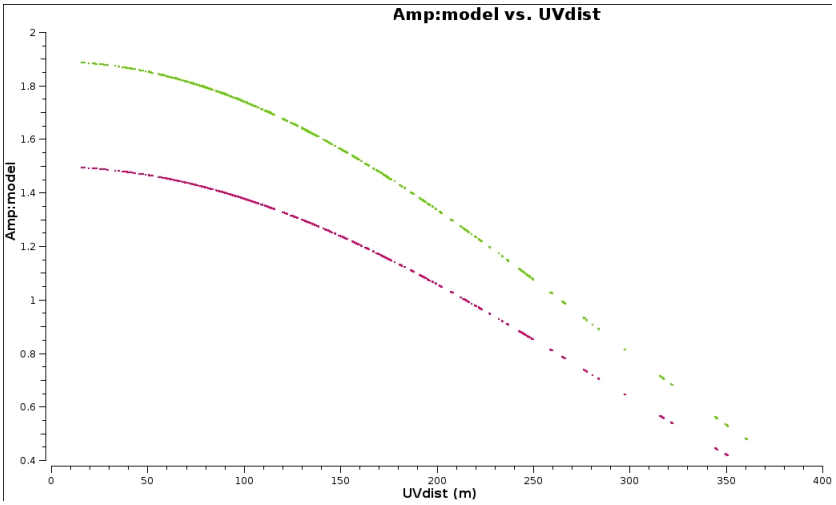

Figure 4.10: Model **amplitude vs UVdist** of Callisto from the archive (green curve) and the actual model setting (purple curve). They were set using the 2010 and 2012 *Butler-JPL-Horizons* versions, respectively. The scale difference between the curves is ∼20%.

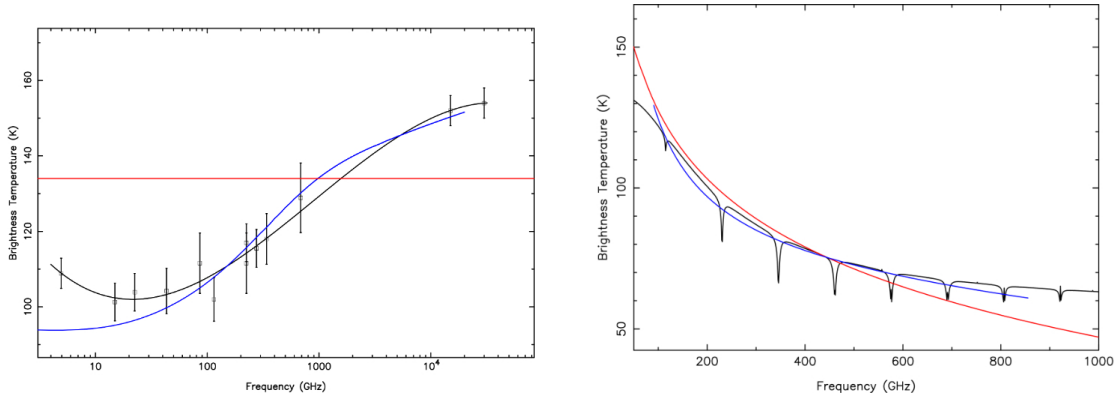

Figure 4.11: **Left panel:** The *Butler-JPL-Horizons* 2012 CASA model brightness temperature of Callisto (in black). The 2010 model is shown in red, blue is the model by Moreno *et al.* (2009).
Right panel: The *Butler-JPL-Horizons* 2012 CASA model brightness temperature of Neptune is shown in black. The red line shows the 2010 model and the blue one the model by Griffin & Orton (1993).

4.3.4 Frequency-dependent calibration

The Bandpass calibration corrects the variation of phase and amplitude as a function of frequency (i.e. the spectral response of each antenna) using CASA's task **bandpass**. Once determined, the electronic fluctuations are considered approximately constant during a single observing run; for this reason, the bandpass calibrator is a bright QSO, usually observed at the beginning of the run, allowing to obtain high SNR in short observation time-scale. The frequency-dependent data corruptions are computed on the basis of this model source and then applied to all sources, including the science target. Since the bandpass complex gains are considered time-independent, it is possible to average over all the integration time to maximize the SNR. In order to avoid signal decorrelation, before solving for bandpass, it is necessary to solve for the variation of phase as a function of time on very short timescale (i.e. for each integration). Usually, in the archival reduction this step is done selecting the central channel of each SPWs; in this work, no channel selection was set because it was verified that the SNR of the short-time phase solutions increases without any channel selection. The time-dependent gain table is applied "on the fly" when computing the bandpass calibration table.

4.3.5 Time-dependent calibration

The next step is to correct for time-dependent corruptions related to the atmospheric turbulence using CASA's task **gaincal**. These variations are frequency-independent, thus they are computed averaging over all the bandpasses to obtain a more statistically significant solution (i.e. higher SNR). Therefore, in order to avoid frequency-dependent decorrelation of the signal, the bandpass calibration tables is applied "on-the-fly" at this step. The phase calibrator is usually a QSO of known position, spectrum and flux density that is modeled as a point-like source at the phase center: once calibrated, it has to have flat amplitudes and phases at zero. Since the phase calibrator is observed to correct for the atmospheric fluctuations, it has to be close to the target in the sky (see Section 2.3.4).

4.3.6 Flux density calibration

Finally, the flux density scale of the secondary calibrators (i.e. bandpass and phase) is bootstrapped from the flux calibrator using CASA's task **fluxscale**. As explained in Section 2.3.5, the raw correlation amplitudes are in Kelvin units but the flux density is measured in Janskys. Fluxscale computes the K/Jy scaling factor that has to be applied to the observed visibilities of unknown flux density to obtain their absolute flux density scale.

Over-resolved flux calibrator

Solar system objects are modeled as uniform temperature disks in the image plane, thus their Fourier transform in the visibility plane is a Bessel function; an example of the corresponding model visibilities is shown in figure 4.12. The panels display the Neptune model amplitude (upper panel) and phase (lower panel) as a function of the increasing baseline length: the model field looks over-resolved at longer baselines. According to the Bessel function theoretical shape, its flux density drops down to zero and then rises again, while the phases have a jump at $\pm 180°$. However, a null flux density value cannot be used for computing the K/Jy scaling factor. In this case, the time-dependent gains of the flux calibrator have to be computed on a subset of antennas which excludes the outermost ones (i.e. the antennas which form the longest baselines); these solutions are used to determine the absolute flux density scale of the secondary calibrators. Once the phase calibrator flux density scale is determined, the K/Jy scaling factor can be solved for all the antennas.

4.3.7 Application of the calibration tables, data examination and further flagging (if necessary)

Once all the correction factors were computed, they were applied to the calibrators and the science target; the corrected data were then examined in order to check for the reliability of the calibration procedure. Amplitude and phase plots as a function of time and frequency were produced to inspect the quality of the time-dependent and frequency-dependent corrections, respectively. Figures 4.13 and 4.14 show how the corrected amplitude and phase versus time should appear: the black, purple, orange and green colors refer to bandpass, flux, phase calibrators and science target, respectively. As expected, the bandpass and the phase calibrators have constant amplitudes and flat phases centered at zero, since they are modeled as point-like sources. Conversely, figure 4.15 shows an example of calibrated visibilities with significant deviations from those expected; further investigations were done in these cases, in order to find the nature of the variation. Typically, systematic problems were found, i.e. issues related to individual time-ranges, corrupted baselines or bad antennas, so that the corrupted data were flagged and each calibration step repeated. In two Band 6 datasets (X1e1 and X1c7) it was not possible to improve the quality of the calibration, so that further investigations were done when the data were imaged (see Section 4.5).
The frequency-dependent calibration is usually checked visualizing the spectral shape of the phase and the flux calibrators; an example of the expected result is that shown in the top left and top right panels of figure 4.16, respectively: the amplitudes should appear generally constant all over the bandpass. In two Band 6 datasets (X4f, X69), the corrected amplitude versus frequency plots displayed an increase at increasing frequencies, and the same spectral behavior was seen in the phase and the flux calibrators spectra, as shown in the bottom left and bottom right

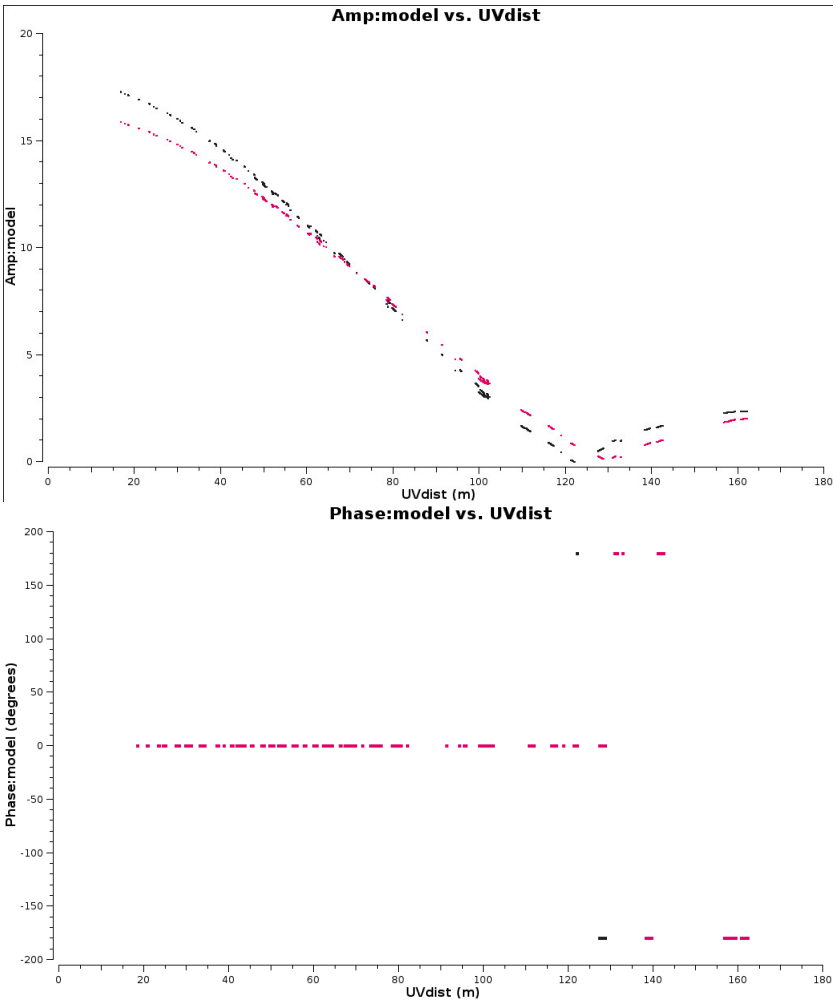

Figure 4.12: Neptune model amplitude (upper panel) and phase (lower panel) as a function of the increasing baseline length. Different colors refer to different SPWs. The panels show how the model of solar system object appears in the visibility plane when the source is over-resolved: the flux density has a discontinuity point at longer baseline lengths, thus drops down to zero and then rises (upper panel); the phases have a jump to $\pm 180°$ in correspondence of the discontinuity point.

panel in figure 4.16, respectively. This may suggest that something wrong happened in the bandpass calibration. In order to solve this issue, the frequency-dependent calibration was repeated, using the phase calibrator as the bandpass calibrator; the resulting flux calibrator spectral shape (left panel of fig. 4.17) is that expected from the model (right panel of fig. 4.17).

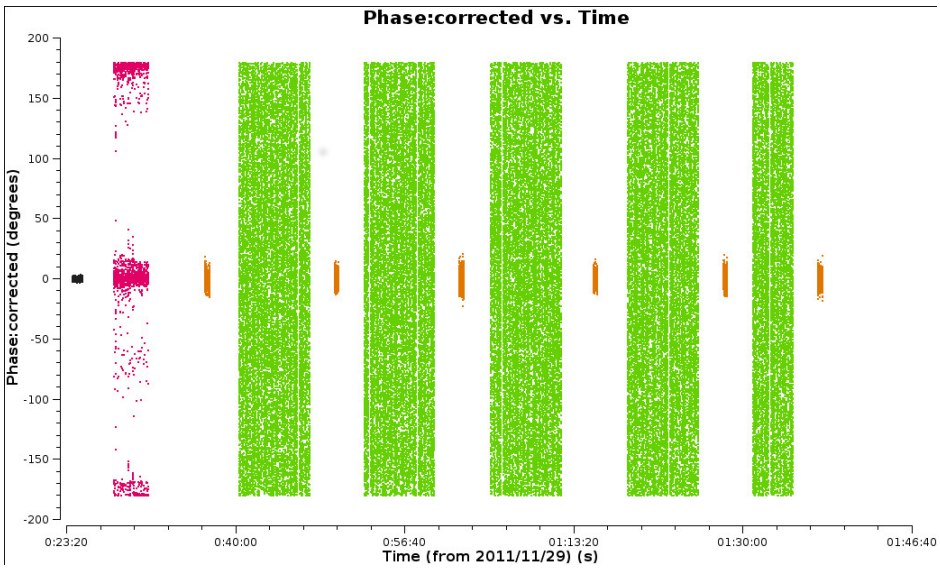

Figure 4.13: Corrected **phase vs time** check plot. All channels are averaged. Different colors for different fields: black, purple, orange and green refers to the bandpass, flux, phase calibrators and the science target, respectively. The panel displays how corrected phases versus time should appear in a good case: flat phases at zero for the point-like sources, the phase jump predicted by the model of the flux calibrator, and uncostrained phases for the science target.

QA2 results

Before starting the imaging process, further investigations about the quality of the calibration were carried out producing the QA2 diagnostic plots (see Section 3.4.1); the archival QA2 results are included in the downloaded packages. Figure 4.18 shows a meaningful example of such diagnostic diagram: they represent the amplitude (upper panel) and phase (lower panel) gains as a function of time for each antenna. Inspect the amplitude gains is useful to probe the antenna efficiencies during the observation time and search for possible outliers; when low amplitude solutions are found, the correspondent antenna is usually flagged (as for the antenna DV16 in the upper panel). The phase solution plots are produced to check for the phase stability as a function of time; when the gains show significant phase scatter, it is necessary to carefully inspect its effect on corrected data.

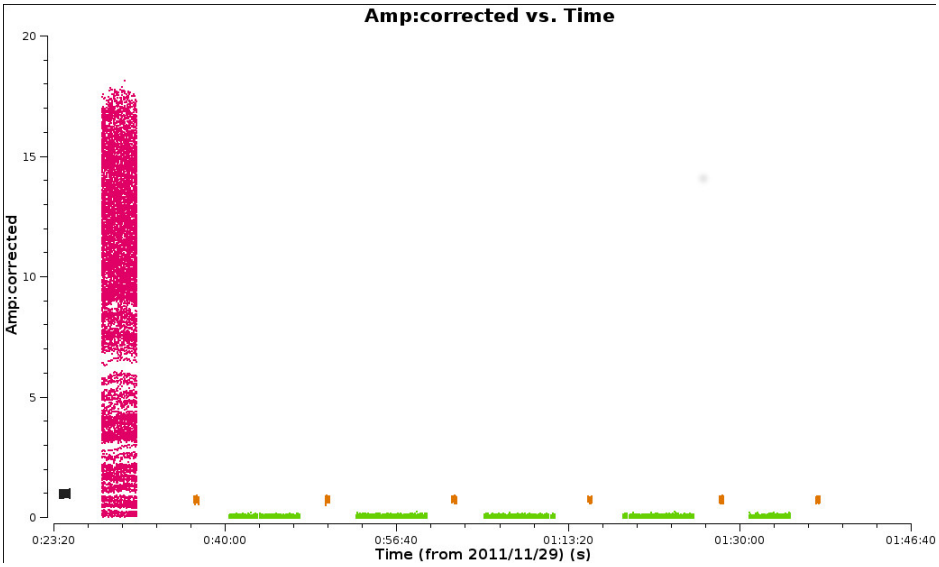

Figure 4.14: Corrected **amplitude vs time** check plot. All channels are averaged. The black, purple, orange and green colors refer to the bandpass, flux, phase calibrators and the science target, respectively. The panel displays a good amplitude calibration: the amplitudes are flat and without any ripples or significant scatter.

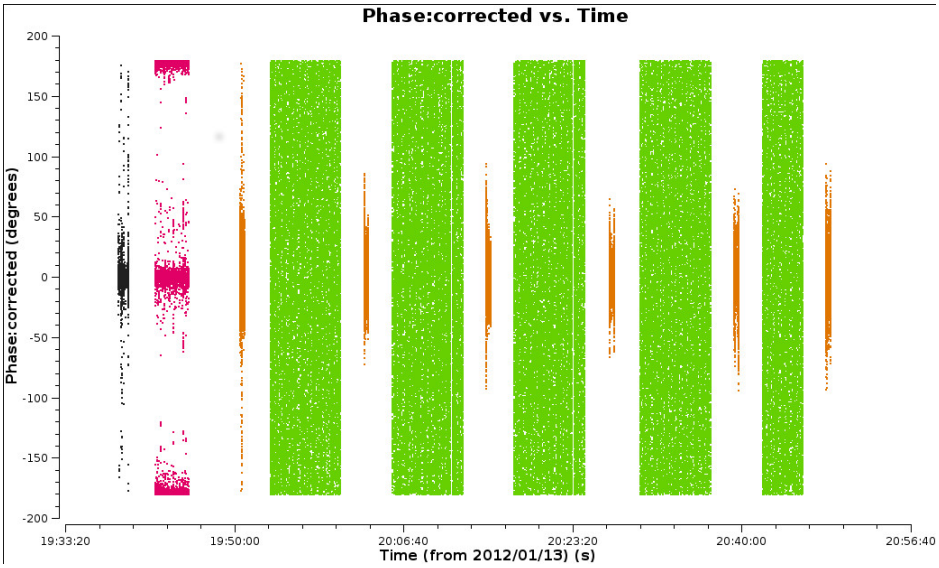

Figure 4.15: Corrected **phase vs time** visibilities check plot. Different colors for different fields: black, purple, orange and green indicate the bandpass, flux, phase calibrators and the science target, respectively. The panel serves as an example of data corruptions that has not been solved by the calibration; when the variation is related to systematic problems (i.e. corrupted baselines or antennas), the correspondent data has to be flagged.

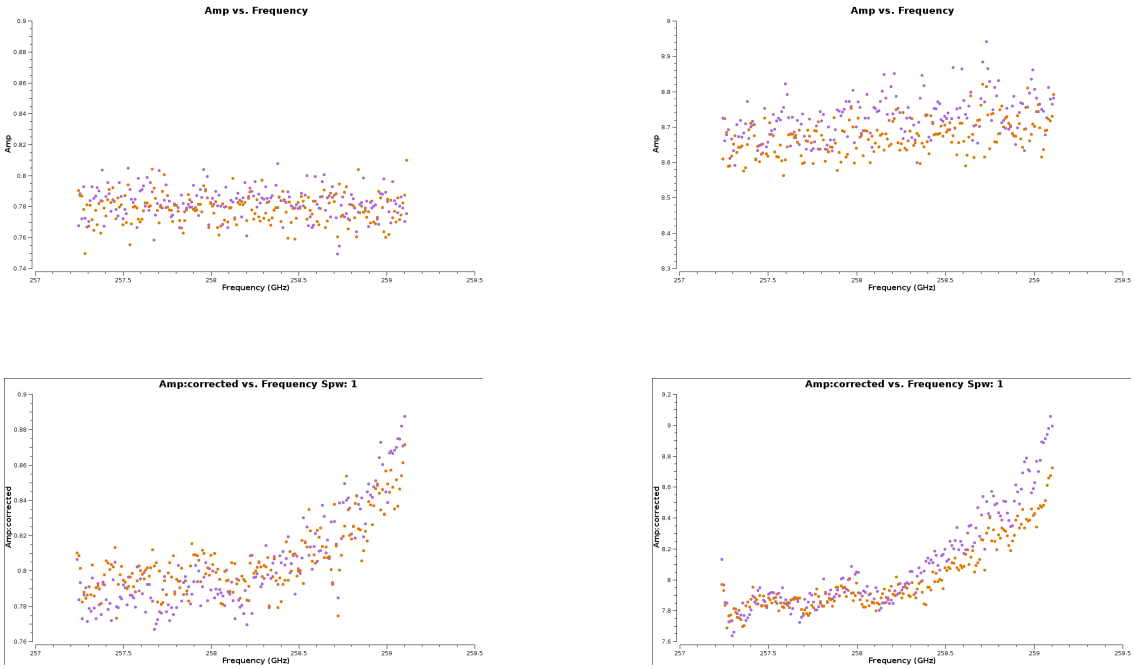

Figure 4.16: **Top left panel:** Amplitude versus frequency plot of the phase calibrator expected in case of reliable bandpass calibration. Data are colorized by correlation.
Top right panel: Amplitude versus frequency plot of the flux calibrator expected in case of a reliable bandpass calibration. Data are colorized by correlation.
Bottom left panel: Amplitude versus frequency plot of the phase calibrator that shows an unexpected increase at increasing frequency.
Bottom right panel: Amplitude versus frequency plot of the flux calibrator that shows an unexpected increase at increasing frequency.

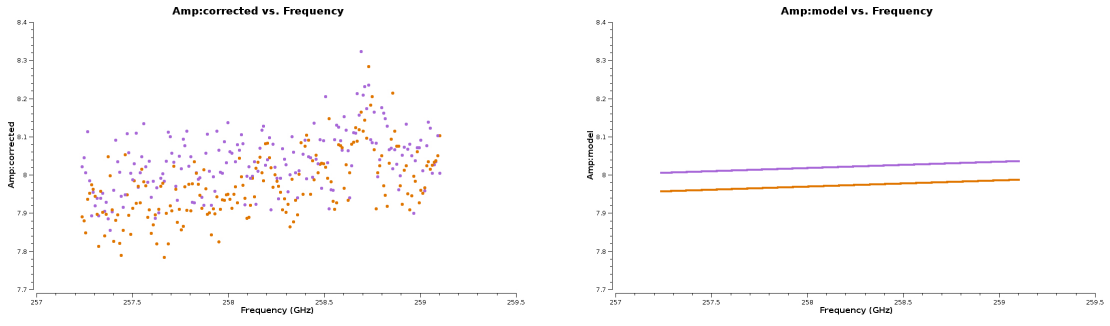

Figure 4.17: Corrected **amplitude vs frequency** of Neptune (left panel) which were obtained using the phase calibrator as the bandpass calibrator. The right panel shows the expected model spectrum. Different color for different polarization products. Time, scan and 20 channels are averaged.

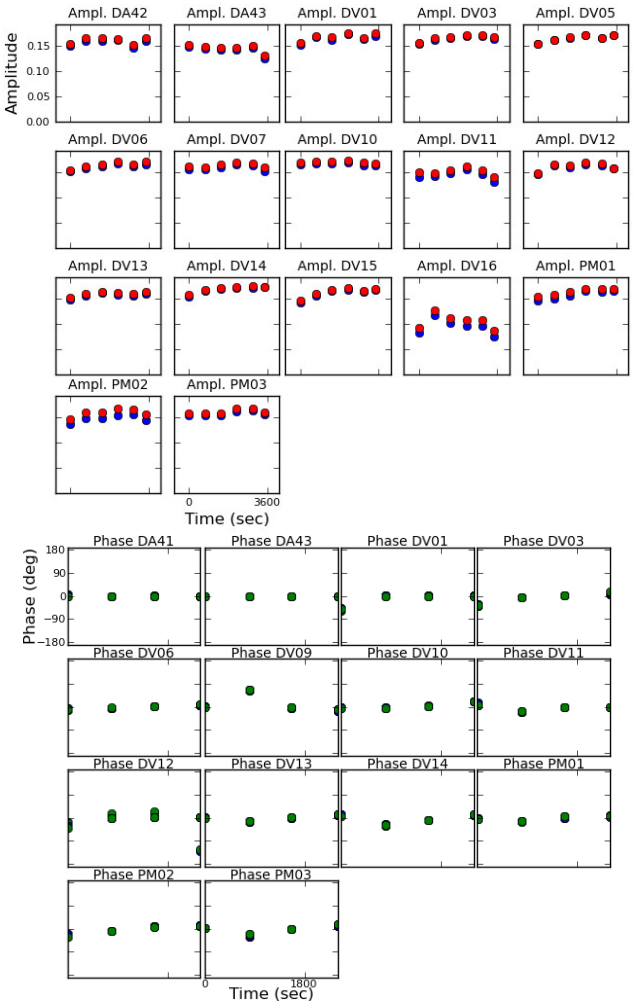

Figure 4.18: Amplitude (upper panel) and phase (lower panel) solutions as a function of time. The plots are iterated by antenna and colorized by correlation (i.e. XX and YY). In the upper panel, the antenna DV16 shows significant lower amplitudes than the others, thus it was flagged. The phase gains look overall stable for the antennas in the lower panel.

4.4 Imaging

Once a reliable calibration was obtained, each group of datasets belonging to the same SB were combined into one calibrated dataset, using CASA's task **concat**; one calibrated dataset in Band 3 and two in Band 6 were obtained and analyzed. Deconvolved images has been produced using the CASA's **CLEAN** task.

4.4.1 The phase calibrator: J2157-694

The phase calibrator at (sub)millimeters waveleghts is usually a bright quasar that, once calibrated, should appear as a point-like source in the image plane; the imaging of the secondary calibrator is another useful check for the quality of the calibration. Figure 4.19 shows the continuum maps of J2157-694 in Band 3 (left panel) and Band 6 (right panel): the phase calibrator looks extended at ∼90 GHz (Band 3), while it looks, as expected, point-like at ∼ 270 GHz (Band 6). Since the Band 3 map of J2157-694 shows an unexpected extended emission, additional inspections were done in the correspondent calibrated data. The extended emission leads to an increasing flux density at shorter baseline lengths and it is clearly shown in its corrected amplitudes versus UVdistance plot (fig. 4.20). In order to improve the accuracy of the calibration, a cut at the shortest baseline lengths was made (red box in fig. 4.20) and the whole calibration process was re-done to this point for Band 3 datasets.

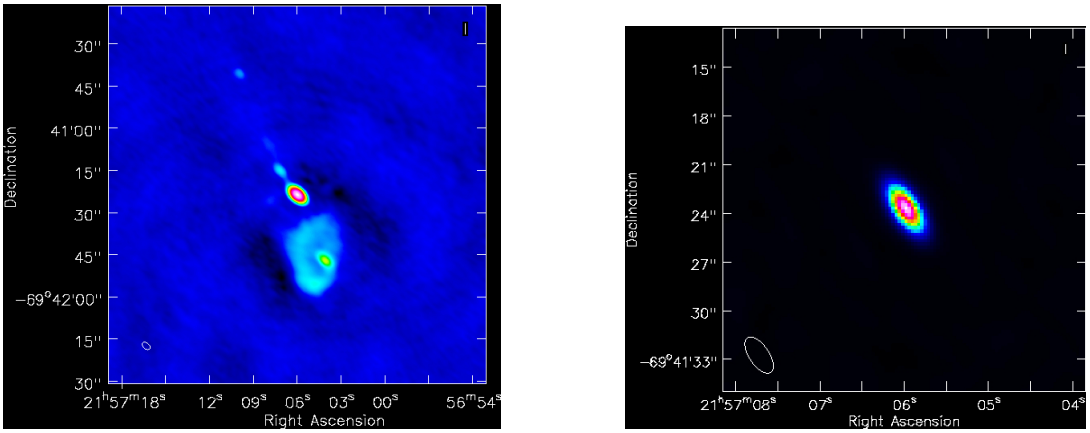

Figure 4.19: **left panel:** J2157-694 image at ∼ 90 GHz produced using natural weighting. The source looks extended. The rms noise level is ∼ 0.22 mJy beam^{-1} after performing amplitude and phase self-calibration. The dynamic range of the image, i.e. the ratio between the peak flux density and the rms noise level in source-free regions, is ∼ 5000. **right panel:** J2157-694 image at ∼ 270 GHz produced with natural weighting. The source looks point-like, as expected. The rms noise level is ∼ 1 mJy beam^{-1} and no self-calibration rounds were performed. The dynamic range of the map is ∼ 800.

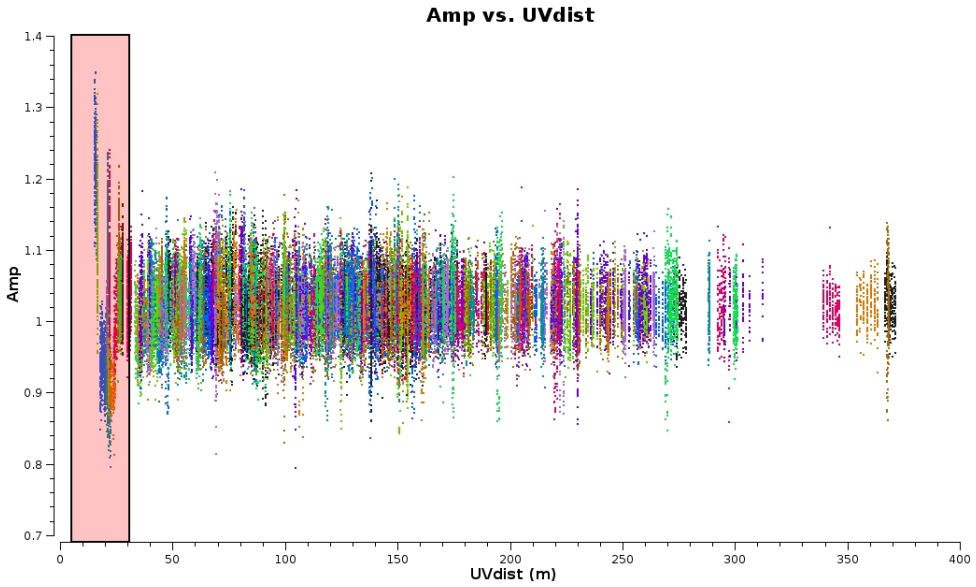

Figure 4.20: Band 3 J694 **Amplitude vs UVdist**. Different colors refer to different baselines. All channels are averaged. The amplitudes have an unexpected increase at shorter baseline lengths and it is due to the extended emission visible in the image plane. The red box highlights the cut that was done at shortest baselines in order to make a more accurate calibration.

Furthermore, in order to check if the calibration was improved with respect to the archival work, the obtained flux densities and rms noise levels of J2157-694 images were compared; the results are summarized in table 4.2. The peak flux densities obtained in this work are lower than the archival ones by $\sim 11\%$, as an expected consequence of the different T_b models (see Section 4.3.3); nevertheless, the dynamic range of the images produced in this work is significantly improved with respect the archival products: ~ 5000 versus 800 in Band 3, and ~ 800 versus 500 in Band 6.

Table 4.2: Comparison between the archival and this work phase calibrator flux densities and dynamic ranges of the images.

		Archival		**This work**	
		Peak flux(1)	**rms**(2)	**Peak flux**	**rms**
Band 3		1.1	1.4	0.98	0.22
Band 6	MOUS 1	0.7	1.3	0.68	0.95
	MOUS 2	0.9	1.3	0.8	1

(1) Peak flux density of the image in Jy beam^{-1}.
(2) Rms noise level of the image (extracted from source-free regions) in mJy beam^{-1}.

4.4.2 The Band 3 products

A first continuum image of the target was produced in Band 3, using *natural* weighting (see section 2.4). The achieved resolution is ~ 1.85 arcsec at 87 GHz and the measured rms noise level of the map was 20 μJy beam^{-1}. Thanks to the high signal-to noise ratio (SNR = 140), a round of phase-only self-calibration was performed, using half-time-on-source as the solution interval (2340 s=38 min). The self-calibrated continuum image shows an improvement with respect to the previous one: the rms drops to 16 μJy beam^{-1}. Consecutive rounds of self-calibration did not show significant improvement on the dynamic range, thus the phase-only self-calibration was applied to all data. The continuum self-calibrated image is shown in figure 4.21. The rms level measured from the available archival continuum map was ~ 40 μJy beam^{-1} after a phase-only self-calibration round.

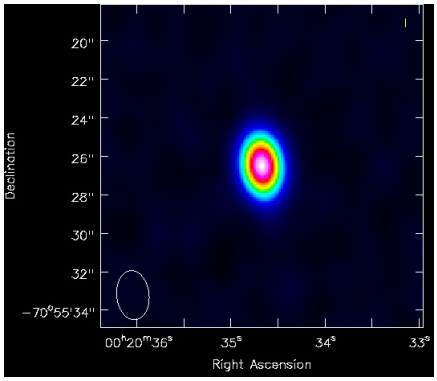

Figure 4.21: I00183 continuum self-calibrated image as seen in Band 3 (representative frequency = 87 GHz). The pixel size was 0.37", while the image size was set to be two times the primary beam at 87 GHz (~ 67 arcsec). The rms noise level is $\sim$16 μJy/beam.

A $CO_{(1-0)}$ line was successfully detected and its emission was isolated by subtracting the continuum in the visibility plane, using CASA's task *uvcontsub*[3]. The CO line channel image was produced using the finest spectral resolution (two channels width, $\sim$ 90 km s^{-1}) unlike what is usually done by the archival imaging, allowing the study of the gas kinematic with higher spectral details. The channels of the map in which the CO emission was found are shown in figure 4.22: the rms noise level is ~ 0.17 mJy beam^{-1}, significantly lower than the archival channel map (0.26 mJy beam^{-1}).

[3]Spectral line data usually contains continuum emission from the target which can make complex the line detection and analysis; for this reason, the continuum subtraction is done. It can be done in the visibilities plane or in the image plane: continuum channels with no lines are modeled and a low-order polynomial fit of them is performed; this continuum model is then subtracted from all the channels

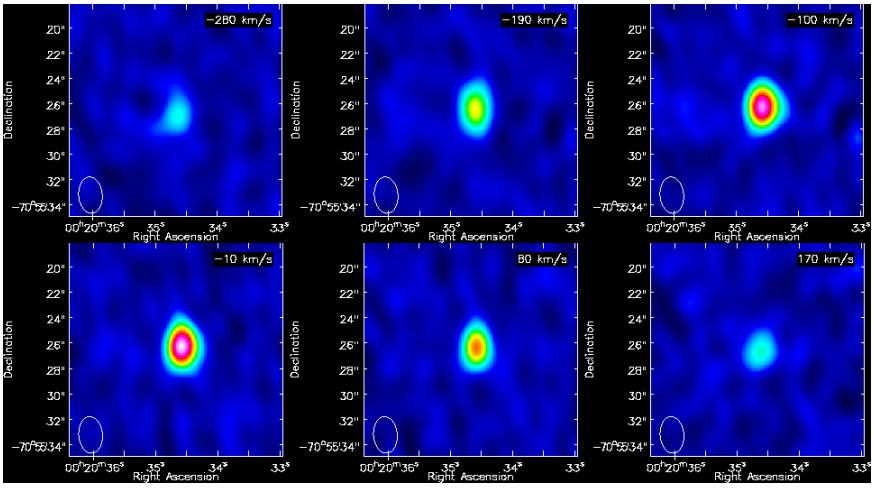

Figure 4.22: I00183 Band 3 CO line channel map. The spectral resolution is $\sim$ 90 km/s and the measured rms is 0.17 mJy beam^{-1}. The different panels show the channels of the map where the CO emission was detected.

4.4.3 The Band 6 products

MOUS 1

As disclosed in section 4.3.7, one EB of this group (X1e1) shows significant data corruptions that cannot be solved by the calibration or making further flags; a useful test was done producing two target continuum images: one obtained combining X1e1 with the others datasets, and one excluding it. The resolution at 270 GHz (3.4 mm) is $\sim$ 0.85 arcsec. The measured rms noise level in the continuum image with 4 EB was 45 μJy beam^{-1}, while it was 15 μJy beam^{-1} when X1e1 was excluded. The second image is clearly improved and X1e1 was marked as not helpful in this observation group. The left panel in figure 4.23 shows the continuum image obtained combining only three EB. The rms noise level of the archival continuum map was $\sim$ 73 μJy beam^{-1}.

MOUS 2

An unreliable calibration was obtained also for one datatset (X1c7), belonging to this observation group. To test its effect when the data are imaged, two continuum images were produced, including or excluding X1c7. The measured rms noise level in the two continuum maps was 48 μJy beam^{-1} (four EB) and 52 μJy beam^{-1} (three EB); even if the calibrated X1c7 data appeared of a poor quality, in this case their contribution yields to slightly improve the dynamic range of the target continuum map, thus all four EB were used. The 4 EB continuum image is shown in the right panel of figure **??**; the rms noise level of the archival product was 69 μJy beam^{-1}. A weak (5σ) HCN line was also detected at 266.7 GHz; the channels in which

the line emission can be identified are shown in figure 4.24. The HCN channel map was produced after subtracting the continuum with a spectral resolution of ~ 40 km/s (forty channels width). The image is highly noisy: the measured rms is ~ 1 mJy beam^{-1}; however, no line detection was declared in the archival report.

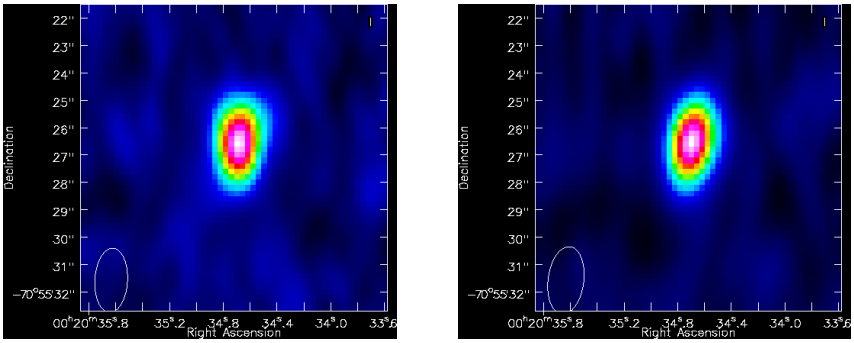

Figure 4.23: **left panel:** I00183 continuum image as seen in Band 6 in the first SB. The representative frequency is 273.27 GHz. The image were produced excluding the X1e1 EB, for which an unreliable calibration was obtained. A pixel size of 0.2" was chosen and an image size of 224×224 pixels was set. The image was produced using natural weighting and the achieved rms noise level is 15 μJy beam^{-1}.
right panel: I00183 continuum image as seen in Band 6 in the second spectral configuration (representative frequency 268.83 GHz). The image has been produced using all four Execution Blocks. A natural weighting was used, with 0.2" as the pixel size and 224×224 pixels as the image size. The rms noise level is 48 μJy beam^{-1}.

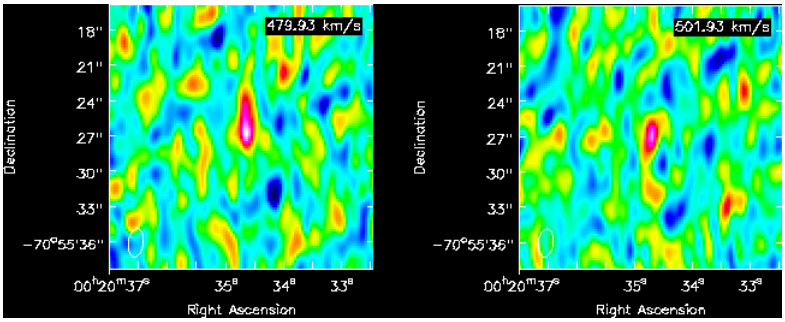

Figure 4.24: I00183 HCN line channel map. The image was produced using ~ 40 km s^{-1} as the spectral resolution (fourty channels width), and it shows the channel in which the line emission is visible; the peak of the line is at a frequency of 266.7 GHz. The measured rms noise level is ~ 1 mJy beam^{-1}.

Chapter 5

ALMA products analysis

5.1 Introduction

The molecular gas traces the colder gas regions where the star formation can take place; its rotational transitions are in the (sub-)millimeter range. These observations are usually used to derive the molecular gas properties and to clarify how and if the AGN is interacting with its host star-forming galaxy. Furthermore, the huge amount of dust surrounding the nuclear regions of ULIRGs absorbs the high-frequency radiation and thermally re-emits at shorter wavelengths. The dust continuum emission peak changes on the basis of the radiation field intensity (~ 20 μm when AGN-heated, ~ 100 μm when starburst heated) thus is can be used, in principle, to identify the dominant power source in ULIRGs. Therefore, the study of the sub-millimeter properties in this class of objects is important to better characterize the complex mechanisms that occur in their inner regions. In order to carry out the scientific purpose outlined in Section 1.4.1, the molecular gas column density was computed from the CO detection in Band 3 and the result will be presented in this Chapter; others interesting properties of the molecular gas were derived and the results will be briefly discussed. The analysis of continuum emission of I00183, sampled in three different frequency ranges, will be also presented.
The results in the following sections, according to the adopted cosmology (Section 1.1), were computed using an arcsec-to-kpc scale of 4.772 kpc/$''$ and a luminosity distance $D_L = 1731.1$ Mpc.

5.2 The CO as molecular gas tracer

The molecular gas mass in galaxies is dominated by molecular hydrogen, H_2, but its strongly forbidden rotational transitions make it very difficult to detect, unless shocked or heated to very high temperatures; for this reason the emission from tracer molecules is usually used to detect H_2 in galaxies (Carilli & Walter 2013). The carbon monoxide (CO), the most abundant molecule in the interstellar medium

(ISM) after H_2, emits strong rotational transition lines (occurring primarily through collisions with H_2): it can be considered as a "good" tracer of the molecular hydrogen. Furthermore, CO traces the star forming regions and is not contaminated by the presence of AGN (Mao *et al.* 2014), thus it can be used, in principle, to measure the relative contributions by star formation to the total power of the ULIRG, and to evaluate the interplay between the AGN and its host star-forming galaxy (Rupke & Veilleux 2013).
As anticipated in Section 4.4.2, a $CO_{(1-0)}$ line was successfully detected in Band 3. The CO luminosity, L'_{CO}, is usually used to compute the total molecular gas mass (dominated by H_2); it can be calculated by knowing the CO integrated flux density, which can be in turn derived from the moment 0 map of the line. For spectral line maps, the output of the imaging process is an image cube, with a frequency or velocity channel axis in addition to the two sky coordinate axes. This can be most easily thought as a series of image planes stacked along the spectral dimension. A useful product can be computed by collapsing the cube into a "moment" image, taking a linear combination of the individual planes. The line emission was isolated by subtracting the continuum from the data cube, and then the moment map was produced; the moment 0 (fig. 5.1) represents the integrated intensity map of the line. The rms noise level is ~ 0.5 Jy beam^{-1} km s^{-1}. A 2-D Gaussian fit was performed to estimate the spatial extent of the line-emitting region; it is resolved with deconvolved size of $(1.63 \pm 0.25) \times (1.09 \pm 0.51)$ arcsec^2, corresponding to $\sim (7.8 \pm 1.2) \times (5.2 \pm 2.4)$ kpc^2. The integrated line flux density is (2.56 ± 0.11) Jy km s^{-1} at 86.8 GHz. L'_{CO} can be measured via the (areal) inte-

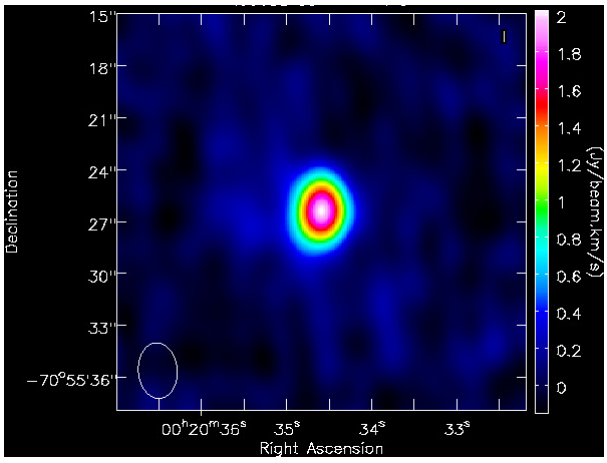

Figure 5.1: CO intensity map (moment 0). The rms noise level is ~ 0.5 Jy/beam km s^{-1} (determined in source-free regions). The wedge on the right shows the color-scale of the map in Jy beam^{-1} km s^{-1}. The integrated flux density results 2.56 ± 0.11 Jy km s^{-1}.

grated source brightness temperature in unit of K km s^{-1} pc^2, using the following equation, which is expressed for a source of any size in terms of the total line flux

(e.g. Bolatto 2013, Solomon & Vanden Bout 2005 and references therein):

$$L'_{CO} = 3.25 \times 10^7 \ (\frac{S_{CO}}{Jy \ km \ s^{-1}}) \ (\frac{\nu_{obs}}{GHz})^{-2} \ (\frac{D_L}{Mpc})^2 \ (1+z)^{-3} \ [K \ km \ s^{-1} \ pc^2] \quad (5.1)$$

where S_{CO} is the integrated line flux density, ν_{obs} is the observing frequency, z is the redshift and D_L is the luminosity distance. The resulting CO luminosity is $L'_{CO} = 1.42^{+0.08}_{-0.12} \times 10^{10}$ [K km s^{-1} pc^2].
Following Bolatto *et al.* (2013), the H_2 mass-to-CO luminosity conversion can be expressed as:

$$M_{(H_2)} = \alpha \ L'_{CO} \ M_\odot \quad (5.2)$$

where α is the so-called H_2 mass-to-CO luminosity conversion factor, and is defined as the ratio of the total molecular gas mass in $M_\odot$ to the total CO line luminosity. Different source populations likely have different values of α, because is strictly dependent on the molecular gas conditions, such as its density, temperature and kinetic state (e.g. Bolatto *et al.* 2013). Downes & Solomon (1998) find a characteristic value of $\alpha = 0.8$ M$_\odot$ (K km s^{-1} pc^2)$^{-1}$ in ULIRGs. Using this α, the estimated H_2 mass is $(1.14 \pm 0.11) \times 10^{10}$ M$_\odot$, which corresponds to the typical amounts found in ULIRGs (e.g. Sanders *et al.* 1999).

5.2.1 The molecular gas column density

The high amounts of gas and dust in ULIRGs are confined in the central region of the system (e.g. Lonsdale *et al.* 2006). As outlined in Section 1.4.1, I00183 has been classified as a AGN-dominated ULIRG (e.g. Mao *et al.* 2014) and was selected from the Spoon diagnostic diagram (Spoon *et al.* 2007) to be a strongly obscured AGN candidate. In order to verify if the molecular gas traced by the CO may be responsible for the obscuration observed in X-ray, the column density of the molecular gas was evaluated. Following the method adopted by Gilli *et al.* (2014), a spherical symmetry of the molecular gas regions was assumed. The radius of the sphere was assumed to be a median value between the major and the minor axis of the elliptical source size ($(7.8 \pm 1.2) \times (5.2 \pm 2.4)$), resulting in $\sim 6.4 \pm 1.7$ kpc. The column density could be roughly estimated multiplying the H_2 density (i.e. $\frac{M(H_2)}{4/3\pi r^3}$) by the median radius. The resulting N_H column density is $(8.0 \pm 0.9) \times 10^{21}$ cm^{-2}. It is important to note that usually the gas mass should refer to the total amount of hydrogen, i.e. M_{H2}+M_{HI}; since M_{HI} is not known, the column density was inferred considering only M_{H2}, and this leads to underestimate the total amount of gas along the line of sight.

5.2.2 The star formation rate

Stars can be created in the cores of molecular gas regions traced primarily by the CO (e.g. Gao & Solomon 2004); the young, hot stars in the star forming regions heat the dust, which thermally re-emits the absorbed radiation in the far-infrared (FIR) regime (Kennicutt 1998). A strong empirical relation was found between the CO and the FIR luminosity, and it can then used to derive an estimate of the galaxy star formation rate. Following Carilli & Walter (2013):

$$log(L_{IR_{starburst}}) = 1.37 \times log(L'_{CO}) - 1.74\ L_{\odot} \tag{5.3}$$

where the IR luminosity is usually defined in the 8-1000 μm wavelengths range, and $IR_{starburst}$ refers to the fact that most of the emission which fall in this regime is attributed to the starburst component. The associated SFR can be computed from:

$$SFR \sim \delta_{MF} \times 1.0 \times 10^{-10} L_{IR_{starburst}} \tag{5.4}$$

where δ_{MF} is a factor dependent on the stellar population; for different range of metallicities, starburst ages and initial mass function, δ_{MF} varies between 0.8-2 (Omont *et al.* 2001). Assuming a Salpter IMF, $\delta_{MF} = 1.8$ (Kennicutt 1998), so that the SFR is ≈ 180 $M_{\odot}$ yr^{-1}. The obtained result appears consistent with that derived by Mao *et al.* (2014) from a $CO_{(1-0)}$ detection, which was carried out with the Australia Telescope Compact Array (ATCA). Mao *et al.* also estimated that the derived SFR (~ 200 $M_{\odot}$ yr^{-1}) contributes only for the 14% to the total power of I00183, confirming that I00183 is predominantly powered by the AGN.

5.2.3 Outflow hint

Direct evidences for feedback phenomena (i.e. outflows) from cool molecular gas regions had been seen both in low or high redshift galaxies (Carilli & Walter 2013), and they have been attributed to either star formation or AGN activity (e.g. Carilli *et al.* 2012, Maiolino *et al.* 2012, Wagg *et al.* 2012). Line broadening and asymmetric profiles are typical spectral features due to outflows, and estimate the associated kinetic energy could provide important information to probe the issue of the galaxy evolution (Carilli & Walter 2013). I00183 was already known from optical emission line spectroscopy to harbor a large-scale galactic outflow (Heckman *et al.* 1990), and further evidence for high-velocity ejection of material was found by Spoon *et al.* (2009) in the mid-infrared regime. Even if the spectral resolution of Band 3 observations is very low (~ 90 km s^{-1}) to carry out a detailed analysis of the molecular gas kinematic, an outflow was tentatively found by analyzing the velocity dispersion map (moment 2) of the CO line emitting region (left panel of fig. 5.2); the analysis was restricted to pixels in the data cube where the signal-to-noise ratio (SNR) is at least five times the rms noise level (determined in line-free channels). The conical section in the south-east side (highlighted by the blue circle) suggests a broadening

of the line; also the velocity versus position map (moment 1, right panel of fig. 5.2) indicates that the corresponding emitting regions are blueshifted. The presence of

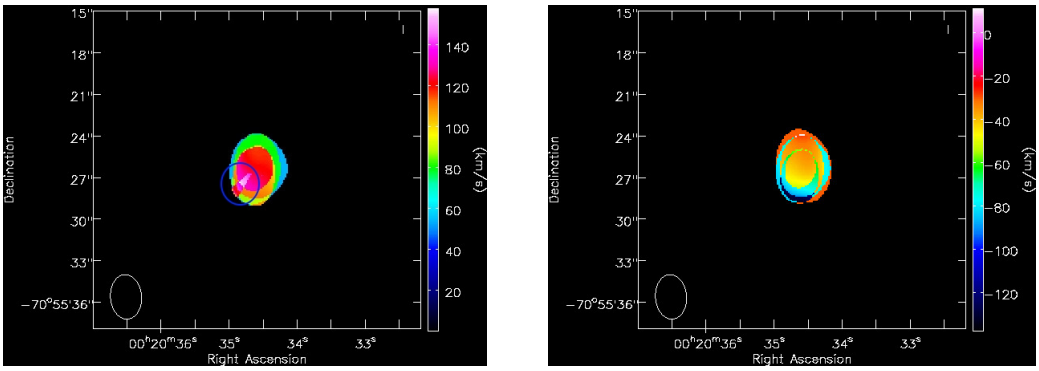

Figure 5.2: CO velocity dispersion (moment 2, left panel) and velocity versus position (moment 1, right panel) maps. The emission is restricted to regions where the SNR in the CO data cube is larger than 5. The color bar on the right shows the color scale in km s^{-1}. A possible outflow hint was found in the region highlighted by the blue circle in the left panel. The corresponding region in the right image shows a blueshift. A detailed analysis of the gas kinematic is not possible due to the poor spectral resolution ($\sim$ 90 km s^{-1}).

a molecular outflow seems to be confirmed by the analysis of the spectral line profile. The upper panel in figure 5.3 shows the spectral profile restricted to a region which excludes the south-east side of the map: it has a clear Gaussian shape with a FWHM of $\sim (363 \pm 14)$ km s^{-1}. The lower panel in figure 5.3 shows the spectrum extracted from the south-east region: the broader spectral shape and the nearly asymmetric profile are typical outflow features; the FWHM is $\sim (500 \pm 21)$ km s^{-1}. Since the poor spectral resolution does not allows to reach reliable conclusions, we are planning to apply for ALMA observations with higher spectral resolution to do further investigations with greater details. The spectra in figure 5.3 also show a velocity offset of $\sim$ 450 km s^{-1} between the expected and the observed line peak. The $CO_{(1-0)}$ rest-frequency is 115.2712 GHz, thus the line center is expected to be 86.87 GHz at z =0.3276 (Roy & Norris 1997). The line peak was found at $\sim$ 86.73 GHz, leading to measure a redshift of 0.3292, which is in agreement with that found by Mao *et al.* (2014). There are different possible explanations for the observed velocity shift: for example, it could be consistent with the redshift error (which is unknown), or it may indicate a possible velocity shift between the molecular gas regions and their host galaxy; anyway, similar velocity offset are frequently found in ALMA spectral line observations, and they cannot be always attributed to different relative velocities with respect to the other galactic components. However, the former hypothesis is favored.

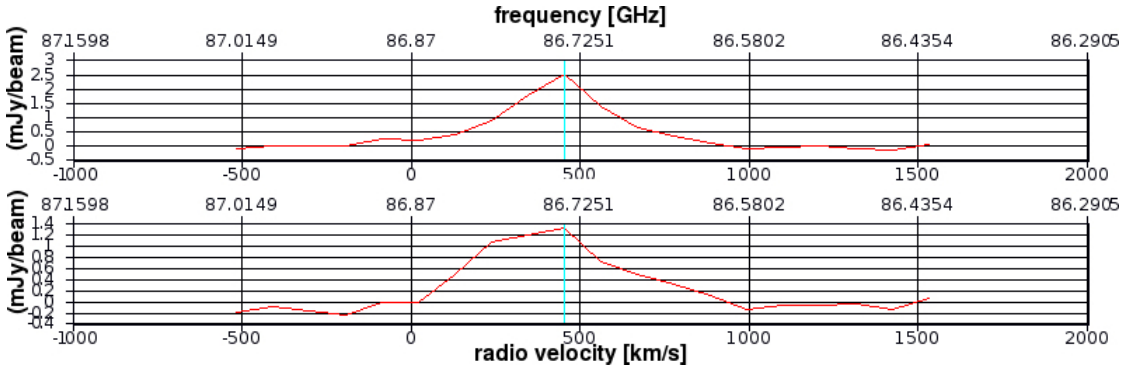

Figure 5.3: Spectral profiles of the $CO_{(1-0)}$ line detected in Band 3. The top axis shows the observed frequencies in GHz; the lower axis indicates the velocity in km s^{-1} relative to the line centre at z=0.327. The expected line peak is 86.87 GHz, while the observed peak is $\sim$ 86.73 GHz, as the light-blue vertical bar shows. The upper panel refers to the profile extracted excluding the south-east emitting region: the profile appears Gaussian with a FWHM$\sim 363 \pm 14$ km s^{-1}. The lower panel shows the spectral shape restricted to the south-east conical region of the line emission: the broader and nearly asymetrical shape are useful hint for ejection of material from the molecular gas regions.

5.3 HCN line detection: the dense molecular gas tracer

HCN is one of the most abundant molecules that traces *dense* molecular gas, $n(H_2) \gtrsim 3 \times 10^4$ cm^{-3}, and is directly associated with active star-forming regions (Carilli & Walter 2013); thus, HCN observations could be used to probe the physical properties of high-density molecular gas around the hidden energy source in the nuclear regions of ULIRGs. The HCN luminosity strictly correlates with the CO luminosity and their ratio could be considered as a powerful starburst indicator (Gao & Solomon 2004). A linear relation between $L'_{HCN(1-0)}$ and L_{FIR} has been found for nearby ULIRGs that seems to be stronger than the non-linear L_{IR} and L_{CO} correlation (Gao & Solomon 2004). Furthermore, ULIRGs nuclei classified as AGN-dominated tend to show higher HCN-to-HCO^+ J=1−0 flux ratios than starburst classified nuclei (e.g. Imanishi & Nakanishi 2006). AGN-heated hot dust could create large amounts of hot molecular gas and more HCN excitation is expected in an AGN than a starburst; for this reason, enhanced HCN emission can be used to detect AGN (Imanishi & Nakanishi 2014).
A weak $HCN_{(4-3)}$ line was found at 266.72 GHz and is shown in figure 5.4. The rms noise level is 1.1 mJy $beam^{-1}$ with a peak flux density of 5.70 ± 0.42 mJy $beam^{-1}$, thus the detection significance of the line is very low ($\sim 5\sigma$); the integrated flux density is 8.64 ± 0.79 mJy. It was not possible to evaluate the spatial extent of the emitting region because the emission is not resolved. Due to the low detection significance of the line, it was not possible to produce reliable moment maps from

its channel image and directly evaluate the HCN luminosity. However, it can be equally estimated from the tight correlation with the CO luminosity. Following Gao & Solomon (2004), the non-linear HCN-CO luminosity relation can be written as:

$$\log L_{HCN} = 1.38 \log L_{CO} - 4.79 \tag{5.5}$$

As computed in Section 5.3, $L_{CO} = 1.42 \times 10^{10}$ K km s^{-1} pc^2, thus $L_{HCN} \sim 10^9$ K km s^{-1} pc^2 and $\frac{L_{HCN}}{L_{CO}} \simeq 0.11$. Typically, for ULIRGs the HCN-CO luminosity ratio is > 0.09, so that the obtained result seems to be in agreement with that expected from theory.
The spectral profile is shown in figure 5.5: the HCN$_{(4-3)}$ rest-frequency is 354.5 GHz so that the expected line peak is 267.14 GHz at z=0.327. The observed line peak is $\sim$ 266.72 GHz confirming the presence of a velocity offset of $\sim$ 400 km s^{-1}. The FWHM is 385 ± 88 km s^{-1}.

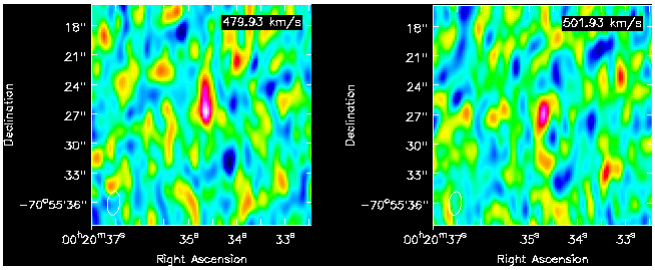

Figure 5.4: I00183 continuum-subtracted HCN map of the two channels in which the line emission was found. The image was produced with a spectral resolution of $\sim$ 40 km s^{-1}, using 0.2 arcsec as the cell size and weighting Briggs (robust=0.5). The rms noise level is 1.1 mJy beam^{-1}, thus the detection significance is very low (5σ).

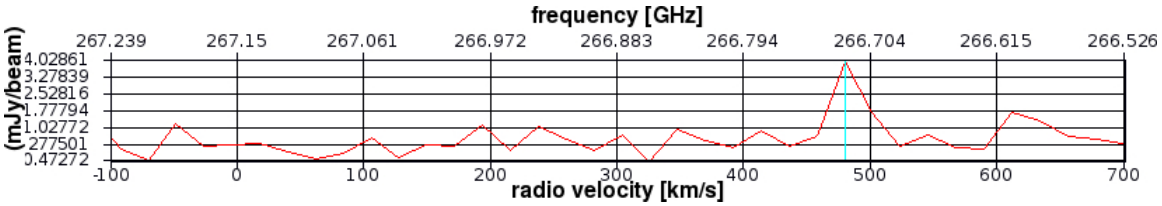

Figure 5.5: Spectral profile of the HCN line detected in I00183. The top axis shows the observed frequencies in GHz; the lower axis indicates the velocity in km s^{-1} relative to the line centre which is expected to be 267.14 GHz at z=0.327. The light-blue bar indicates the observed peak of the line at $\sim$ 266.72 GHz.

The properties of the line emissions, derived from the image analysis, are summarized in table 5.1.

Table 5.1: ALMA line emission properties

	$\nu_{rest}^{(1)}$	$\nu_{obs}^{(2)}$	**Peak flux**$^{(3)}$	**rms**$^{(4)}$	**Flux density**$^{(5)}$	**FWHM**$^{(6)}$	**Luminosity**$^{(7)}$
CO	115.271	86.73	5.5 ± 0.15 (32σ)	0.17	6.52 ± 0.30	363 ± 14	1.42×10^{10}
HCN	354.505	266.72	5.7 ± 0.42 (5σ)	1.1	8.64 ± 0.79	385 ± 88	$\sim 10^9$

(1) Rest-frame frequency of molecular lines in GHz.
(2) Observed frequency of the line peak in GHz.
(3) Observed line peak flux in mJy beam^{-1} with the detection significance relative to the rms noise in parentheses.
(4) Rms noise level (1σ, computed in line-free regions) in mJy beam^{-1}.
(5) Integrated line flux density in mJy.
(6) Observed FWHM of the line in km s^{-1}.
(7) Molecular line luminosity in K km s^{-1} pc^2.

5.4 Continuum analysis

As outlined in section 1.2, a significant fraction of the bolometric luminosity of ULIRGs is absorbed by the high amount of dust surrounding their central regions and thermally re-emitted in the infrared regime. The absorption cross-section of the dust is strongly peaked in the UV regime, thus in principle the FIR emission can be considered a tracer of young stellar populations, with a continuum emission peak at $\sim$ 100 μm (e.g. Kennicutt 1998). When the central dominant engine is an AGN, its intense radiation field "heats" the surrounding dust layers, and the continuum peak of this warmer dust component is shifted at shorter wavelengths ($\sim 20\ \mu$m). Therefore, the continuum emission can be considered another useful tool to investigate about the starburst and AGN contribution in ULIRGs (Lonsdale *et al.* 2006). The continuum maps obtained in this work refer to different frequency ranges, and allow to infer interesting properties about the observed continuum emission. The main results from the analysis of the continuum maps are summarized in table 5.2. The spatial extent of the emitting regions was derived performing a 2D Gaussian fit and the tabulated monochromatic luminosity was computed using Lister *et al.* (2011):

$$L = \frac{4\pi\ D_L^2\ \nu\ S_\nu}{(1+z)}\ erg\ s^{-1} \tag{5.6}$$

where D_L is the luminosity distance and (1+z) accounts for the k-correction factor.

5.4.1 AGN jets or dust?

The emission from dust is modeled as a modified Black Body, the so-called "grey body" (e.g. Berta *et al.* 2015). In a Rayleigh-Jeans regime ($h\nu \ll kT$), the dust continuum thermal emission can be approximated to $F_\nu \sim \nu^{\beta+2}$, where β is the emissivity coefficient, that is strongly dependent on the dust grain compositions (e.g. Li & Draine 2007); for a typical FIR dust emission it was found in the range between

Table 5.2: ALMA continuum emission properties

	Freq. ranges$^{(1)}$	**Flux**$^{(2)}$	**rms**$^{(3)}$	**Beam pattern**$^{(4)}$	**Source size**$^{(5)}$	**Luminosity**$^{(6)}$
Band 3	86.1-87.8/96.2-97.7	3.4 ± 0.0019	0.016	2.57×1.69	$(3.37 \pm 0.2) \times (2.26 \pm 0.1)$	$\sim 8.2 \times 10^{41}$
Band 6	257.2-259.11/272.35-274.22	2.21 ± 0.098	0.015	2.35×1.19	$(4.8 \pm 1.1) \times (3.8 \pm 1)$	$\sim 2.1 \times 10^{42}$
	253.3-255.2/266.2-267.8	2.6 ± 0.07	0.05	2.48×1.31	$(3.9 \pm 0.8) \times (2.7 \pm 0.52)$	$\sim 2.4 \times 10^{42}$

(1) Observed frequency ranges in GHz.
(2) Integrated continuum flux density in mJy.
(3) Rms noise level (1σ, computed in source-free regions) in mJy beam^{-1}.
(4) Synthesized beam size in $arcsec \times arcsec$.
(5) Source spatial extent deconvolved from the clean beam in kpc^2.
(6) Monochromatic luminosity in erg s^{-1}.

1.5-2.0 (e.g. Berta *et al.* 2015). As a consequence, the expected flux density from dust continuum emission has to significantly increase with the increasing frequency. The obtained continuum flux densities show the opposite behavior: they decrease from 3.4 to 2.6 and 2.2 mJy at 87, 260 and 270 GHz, respectively. It was already well established that I00183 hosts a powerful radio source in its central regions with $L_{4.8GHz} = 3 \times 10^{25}$ W Hz^{-1} (Roy & Norris 1997), which places it within the regime of the FRII (i.e. high luminosity) radio galaxies. Furthermore, VLBI observations of I00183 presented by Norris *et al.* (2012) show the presence of a compact radio-loud AGN in the galaxy nuclear regions; it shows quasar jets only 1.7 kpc long, boring through the dense gas and starburst activity that still confine them. Norris *et al.* argue that the morphology and the spectral index of the source are consistent with Compact Steep Spectrum (CSS) sources, which are widely thought to represent an early stage of evolution of radio galaxies: the I00183 AGN seems to have just switched on and started boring its way through the dense nuclear environment. The presence of a powerful radio source and its strong associated radio power can be considered an hint that the observed continuum could trace non-thermal radio emission. The radio synchrotron emission is described by a power law with $F_\nu \propto \nu^\alpha$, where α is the slope of the radio photon-energy spectrum (i.e. the spectral index); a negative spectral index is usually associated to the synchrotron spectrum. The ALMA continuum flux densities distribution shows a negative and flat spectral index ($\alpha \approx -0.24$) at increasing frequency, and this lead to consider the observed continuum as the tail of the radio synchrotron emission, rather than the thermal dust emission. This "picture" seems to be confirmed by computing the flux densities expected from dust emission at the observed frequencies. Following the method adopted by Berta *et al.* (2015), the expected monochromatic dust luminosity, from which the flux density can be derived, is computed as: $L_\nu = 4\pi M_{dust} k_\nu B_\nu(T_{dust})$, where M_{dust} can be approximately evaluated knowing that in Galactic environment $M_{gas}/M_{dust} \approx 10^{-2}$, and $k_\nu B_\nu(T_{dust})$ is the modified black body law; k_ν represent the frequency-dependent absorption coefficient of dust and was assumed from values tabulated by Li & Draine (2007, table 6). The obtained monochromatic flux densities are two orders of magnitude less than that observed ($\sim$ 10 μJy), reinforcing the hypothesis than the observed ones could not trace

primarily the dust emission. Figure 5.6 shows a Radio/IR SED of I00183, with radio, ALMA, and Herschel flux densities taken from Norris *et al.* (2011), the present work, and the Herschel archive, respectively; in the figure they are indicated by red triangles, green circles and blue squares, respectively. The negative and relatively flat slope of the ALMA observed flux densities seems to be consistent with the tail of the radio synchrotron emission.

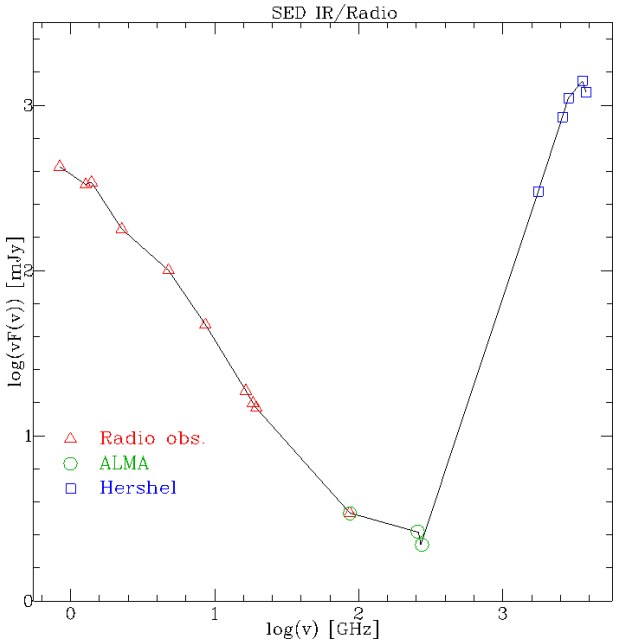

Figure 5.6: Radio/Infrared Spectral Energy Distribution of I00183 with the observed frequencies in the lower axis. The radio, ALMA and far-infrared flux densities are from Norris *et al.* (2011), this work and the archival Herschel observations, respectively; they are highlighted by red triangles, green circle and blue squares, respectively. The observed ALMA flux densities are consistent with the tail of radio synchrotron emission, rather than with the dust thermal emission, with a spectral index of -0.24.

5.4.2 The line-continuum emissions offset

By superimposing the Band 3 continuum and the CO line maps, an offset of 0.53 ± 0.08 arcsec ($\sim 7\sigma$), corresponding to $\sim 2.5 \pm 0.4$ kpc, was found between the two emitting sources, fitted with a Gaussian shape. The error of the offset was computed by considering the beam size and the $\mathrm{SNR}_{detection}$ for both images ($\sigma \sim beam\ size/SNR$). The measure has been performed in the not self-calibrated maps.
A possible explanation of this offset could be found in the AGN double-jet morphology observed by Norris *et al.* (2012). The jets length (1.7 kpc) seems to be consistent with the shift between the line and the continuum emission: probably

the quasar that has just switched on is starting boring its way through the dense nuclear environment. As shown in figure 5.7, the radio-loud structure results unresolved in ALMA Band 3 continuum map ($\sim$ 3 arcsec), because it is completely embedded within the beam size.

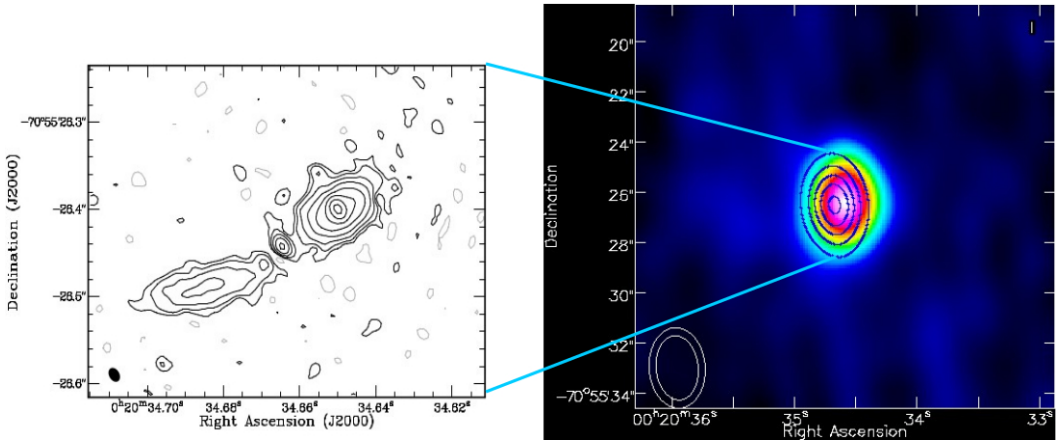

Figure 5.7: VLBI map of I00183 (left panel) adapted from Norris *et al.* (2012) and ALMA CO line moment 0 with the continuum contours superimposed. Contours are drawn at 3,6,9, ... times the 1σ rms noise level. The spatial extent of the region imaged by the VLBI observation is completely embedded into the ALMA continuum synthesized beam. The jets length (1.7 kpc) and orientations are consistent with the observed shift between the line and the continuum emission in ALMA Band 3 ($\sim$ 2.5 kpc).

5.5 Summary of the results

The principal results obtained from ALMA observations can be summarized as on follow:

- **Molecular gas mass:** The H_2 mass evaluated assuming an H_2 mass-to-CO luminosity conversion factor typical for ULIRGs (i.e. $\alpha = 0.8$) is $M_{H_2} = (1.14 \pm 0.10) \times 10^{10}$ $M_\odot$. In the following, this value will be compared with that derived from the X-ray spectral analysis.

- **Gas column density:** The molecular gas column density along the line of sight was roughly estimated assuming a spherical symmetry and using the derived molecular mass: $N(H_2) \approx (8.0 \pm 0.9) \times 10^{21}$ cm^{-2}.

- **Star formation rate:** The correlation between the CO and the FIR luminosity was used to compute a star formation rate of ≈ 180 $M_\odot$ yr^{-1}.

- **Outflow:** The velocity dispersion and the velocity versus position moment maps of the CO line suggest the presence of a molecular gas outflow from the

CO emitting regions. A detailed analysis about the gas kinematic was not possible due to the low spectral resolution of the observation (~ 90 km s^{-1}).

- **Dense molecular gas:** The HCN line detection highlights the presence of *dense* molecular gas, but its low detection significance ($\sim 5\sigma$) does not allow further investigations.
- **Continuum emission:** Three continuum maps at 87, 260 and 270 GHz were obtained, with an integrated flux density of 3.4, 2.6 and 2.2 mJy, respectively. The negative spectral index ($\alpha = -0.24$) of the continuum flux densities suggests a possible radio synchrotron origin, rather than a thermal dust emission.
- **Continuum-line offset:** An offset of ~ 2.5 kpc was found between the line and the continuum emission. The origin of the offset can be attributed to the radio-loud nuclear source, with jets 1.7 kpc long.

Chapter 6

X-ray data reduction and spectral analysis

6.1 Introduction

In order to address the scientific purpose outlined in section 1.4.1, *Chandra*, XMM-*Newton* and *NuSTAR* X-ray data of IRAS 00183-7111 (I00183) were used, covering the energy range $\sim 0.5 - 30$ keV. *Chandra* and XMM data were downloaded from the archives[1], and then data reduction, spectral extraction and analysis were carried out; *NuSTAR* data are still private and the reduced spectra were obtained by courtesy of the PI (K. Iwasawa).
The fundamental rules to reduce X-ray data are the same in most cases but a good knowledge of the properties of X-ray satellites and their instruments is important to maximize the scientific output. For this reason, the fundamental X-ray astronomy parameters will be introduced in this Chapter; in the second part, data and the process of data reduction and analysis will be discussed.

6.2 X-ray astronomy: the basics

The high-energies observations need to be done in space by satellite due to atmospheric absorption of the X-ray signal. X-rays detection is done using the reflection on mirrors based on the principle of **grazing incidence**. From the Snell's law, it is possible to derive the critical reflection angle as:

$$\theta_c \approx 28(\rho\ Z/A)^{1/2}\ E^{-1} \tag{6.1}$$

where ρ is the density of the material used to coat the mirrors (expressed in $g\ cm^{-3}$), E is the energy of the incident photons and Z/A is the ratio between the atomic

[1] *Chandra* archive: http://cda.harvard.edu/chaser;
XMM-*Newton* archive: http://nxsa.esac.esa.int/nxsa-web

number and the atomic weight of the coating material. The strategy is to use high-density material to coat the telescope mirrors, in order to increase the angle defined in 6.1. To be detected (i.e. to be reflected by the mirrors and focused on the instrument focal plane), a photon must have an incidence angle less than the critical incidence angle; to be more precise, in the Wolter-I optics (used, e.g., by XMM-*Newton* and *Chandra*) the X-rays must complete a double grazing reflection to be focused correctly. At energies below 10 keV, the most common X-ray detectors are different kind of CCD, which record the position, energy and arrival time of the incoming photons.
The most important properties of X-ray satellites and instruments are:

- Sensitivity
- Angular resolution
- Encircled energy fraction
- Effective area
- Spectral resolution

Sensitivity

The sensitivity defines the minimum detectable flux. It is related to the signal-to-noise ratio (SNR) of an observation which is defined as:

$$SNR = n_\sigma = \frac{C_s}{\sqrt{C_s + C_b}} = \frac{\varepsilon A_{eff} T_{int} \Delta E F}{\sqrt{A_{eff} T_{int} \Delta E B}} \tag{6.2}$$

where F and B are the source and background fluxes, respectively ($photons\ cm^{-2}\ s^{-1}\ keV^{-1}$), A_{eff} is the effective area of the instrument in cm^2, ΔE is the energetic range, ε is the detection efficiency and T_{int} is the integration time. From 6.2, it is possible to define the minimum detectable flux:

$$F_{min} = \frac{n_\sigma}{\varepsilon} \sqrt{\frac{B}{A_{eff} T_{int} \Delta E}} \tag{6.3}$$

Effective area

The geometric area of a telescope (A_{geom}), i.e. the mirrors cross-section, is reduced by several factor to a much smaller effective area. It can be defined as:

$$A_{eff}(E, \theta, x, y) = A_{geom} \times R(E) \times V(E, \theta) \times QE(E, x, y) \tag{6.4}$$

In 6.4, R(E) is the *reflectivity*, i.e. the fraction of photons reflected by the mirrors; V(E, θ) is the *vignetting*, which is the effect of photon loss as a function of the

increasing off-axis angle (θ); QE is the *quantum efficiency*, which represents the fraction of incident photons actually registered by the detector; in the case of a CCD, the QE is a function of the position (x,y) on the detector and of the energy. All these information define the efficiency of an instrument in revealing photons and are stored in the so-called *Auxiliary Response File* (ARF)[2]. Moreover, what an instrument measures is a collection of photon counts (C) associated to appropriate instrument channels (I). In order to obtain the observed source spectrum in photon count rate as a function of energy (in keV), a *Redistribution Matrix File* (RMF)[3] is created to associate to each instrument channel (I) the appropriate photon energy (E). Furthermore, a background spectrum needs to be extracted, in order to estimate its incidence in the observation. The ARF and RMF (i.e. the *instrumental response*) are combined with the source and the background spectra to carry out the spectral analysis producing a background-subtracted observed source spectrum folded with the instrumental response.

Angular resolution

The angular resolution is the detector capability to distinguish between objects in the same field of view separated by small angular distances: it is a measure of how well a telescope can solve details. The angular resolution can be quantified by the *Point Spread Function* (PSF) which is defined as the response of an imaging system to a point-like source. The PSF depends on the source position on the detector and the energy of the incoming photons: in the soft band (2−10 keV), it is broader (i.e. lower angular resolution) as the off-axis angle and the X-ray energy increase; thus, the image quality is best in a small area centered about the optical axis of the telescope, and for photons of lower energy. The angular resolution can be defined by the two parameters which describe the PSF: the Full Width at Half Maximum (FWHM) and the Half Energy Width (HEW); the latter is the PSF width including 50% of the incoming photons.

Encircled energy fraction

Directly related to the distribution of energy in the PSF is the *fractional encircled energy* measure. It represents the fraction of the total energy enclosed within a circular region of the image and is strongly dependent on the energy of incoming photons and on the off-axis angle. For an on-axis point source at 1.5 keV, the *Chandra* encircled energy is $\sim$ 90% within a radius of $\sim$ 1 arcsec (Fig. 6.1), while the XMM-*Newton* EPIC PN and MOS 1-2 encircled energy is $\sim$ 90% within a radius of 35 and 45 arcsec, respectively (Fig. 6.2). It is important to be aware of these quantities before choosing the spectrum extraction radius from X-ray images.

.

[2]http://cxc.harvard.edu/ciao/dictionary/arf.html
[3]http://cxc.harvard.edu/ciao/dictionary/rmf.html

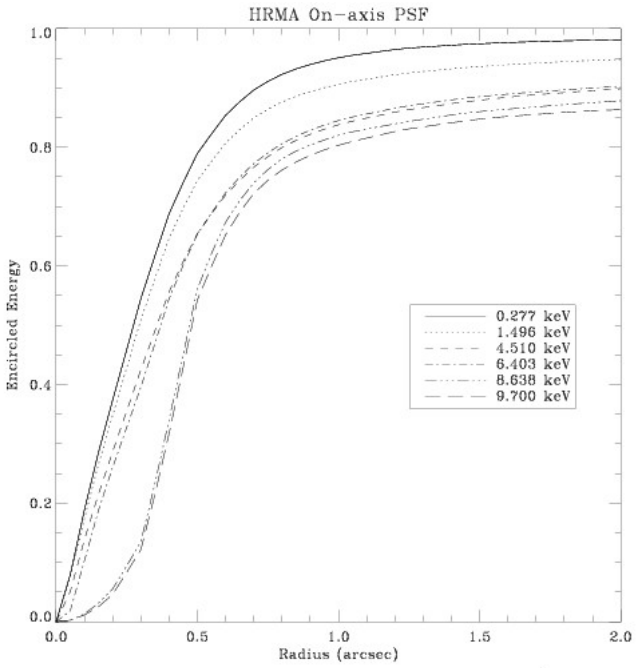

Figure 6.1: *Chandra* fractional encircled energy as a function of angular radius, calculated for an on-axis point source at different X-ray energies (from 0.3 to 9.7 keV).

Spectral resolution

One important property is the detector spectral response to a mono-energetic source of radiation. In an ideal case, the recorded pulse distribution is a delta function, while in the real case it is a Gaussian function, peaked around H_0 (the energy of the incident photon). The *spectral resolution* is defined as the ability of a detector to distinguish between photons of similar energy. Defining the FWHM as the parameter which describes the width of the response function, the energy resolution is:

$$R = \frac{FWHM}{H_0} = \frac{2.35\sigma}{H_0} \tag{6.5}$$

where σ is the standard deviation of the Gaussian distribution. If N is the number of recorded events, $H_0 = KN$, while assuming a Poissonian distribution (i.e. a random distribution) of the events, $\sigma = K\sqrt{N}$; so that:

$$R_{poisson} = \frac{FWHM}{H_0} = \frac{2.35K\sqrt{N}}{KN} = \frac{2.35}{\sqrt{N}} \tag{6.6}$$

However, a simple Poisson statistic cannot be applied because not all events can be considered totally independent from each others. For this reason, introducing the *Fano factor*, which represents the ratio between the observed and the expected

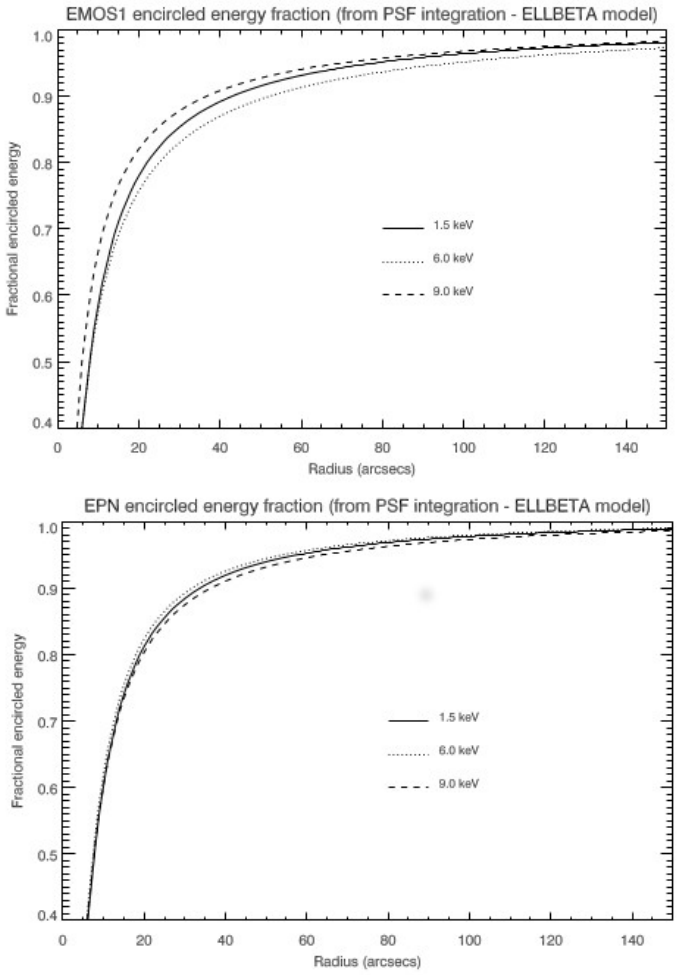

Figure 6.2: The MOS1 (upper panel) and PN (lower panel) fractional encircled energy as a function of angular radius (on-axis) at different energies (from 1.5 to 9 keV).

Poisson variance in N, the energy resolution that a detector can obtain is:

$$R_{stat.limit} = 2.35\sqrt{\frac{F}{N}} \tag{6.7}$$

6.2.1 Chandra

NASA's *Chandra* X-ray Observatory (CXO) was launched on July 23, 1999; it provides the best ever capabilities for high-resolution imaging, spectrometric imaging and high-resolution spectroscopy over the X-ray band 0.1−10 keV (Weisskopf *et al.* 2000). The telescope system consists of four nested pairs of grazing incidence paraboloid and hyperboloid mirrors which were assembled into a support structure called the High Resolution Mirror Assembly (HRMA; Gaetz & Jerius 2005, *Chandra* X-ray Center Memo Series). Mirrors are coated with iridium and aligned to be parallel with incoming X-rays; they are the smoothest and cleanest mirrors ever made. Such a structure leads to the best ever angular resolution reached by an X-ray telescope, 0.5 arcsec on axis, which is approximately 1000 times better than the first X-ray telescope[4]. *Chandra* effective area ranging from $\sim 800\ cm^2$ (@ 1 keV) to $\sim 40\ cm^2$ (@ 5 keV)[5]. The mirrors work together to focus the incoming X-rays to converge on the focal plane, which is about 10 meters away. The focal plane science instruments capture the images previously formed by the mirror and provide information about the incoming photons: their number, position, energy and time of arrival. *Chandra* QE is near to 100% from 1 keV to 7 keV but it has an important cut-off at very low energies or above 10 keV; its spectral resolution is ~ 100 eV at 6 keV.
There are different kind of science instruments aboard Chandra:

- **Advanced CCD Imaging Spectrometer (ACIS)**: ten CCD chips divided into two arrays of four square chips (ACIS-I) and six chips in a string (ACIS-S). Each CCD subtends 8.4 arcmin by 8.4 arcmin square on the sky providing imaging and spectroscopy[6];

- **High Resolution Camera (HRC)**: two micro-channel plates arrays referred to as HRC-I and HRC-S with a large field-of-view ($\sim 30 \times 30$ arcmin and $\sim 6 \times 90$ arcmin, respectively) to make X-ray images;

- **High Energy Transmission Grating (HETG)** and **Low Energy Transmission Grating (LETG)**: two movable grating inserted on focused X-ray beam and dedicated to high resolution spectroscopy.

[4]See http://chandra.si.edu
[5]http://cxc.harvard.edu/proposer/POG/html/chap4.html
[6]http://cxc.harvard.edu/proposer/POG/html/chap6.html

6.2.2 XMM-Newton

The X-ray Multi-Mirror (XMM-*Newton*) satellite is an X-ray space observatory launched by the European Space Agency (ESA) on December 10, 1999. The telescope consists of three mirror modules of 58 nested shells each which lead to the largest effective area of an X-ray telescope ever ($\approx 4650\ cm^2$ in total, @1.5 keV). There are three types of instruments aboard XMM: 3 European Photon Imaging Camera (EPIC) CCD instruments for X-ray imaging, moderate resolution spectroscopy and X-ray photometry, divided into two different types: EPIC MOS (Metal Oxide Semi-conductor) CCD arrays and EPIC pn CCD camera; 2 Reflection Grating Spectrometers (RGS) for high-resolution X-ray spectroscopy and spectro-photometry; an Optical Monitor (OM) for optical/UV imaging and grism spectroscopy. The three EPIC cameras and the two RGS spectrometers reside in the focal plane of the X-ray telescope, while the OM has its own telescope. All instruments work simultaneously and independently but only the EPIC pn camera focuses the full incident photons; the EPIC MOS cameras receive only $\approx 44\%$ of the incoming light, the rest is dispersed to the two RGS. The MOS 1-2 energy resolution is ~ 150 eV (@ 6 keV) while it is ~ 130 eV for the PN (@ 6 keV). The PSF FWHM is ~ 6 arcsec on-axis and the HEW is ~ 15 arcsec (see, e.g., Jansen *et al.* 2001, Turner *et al.* 2001, Strüder *et al.* 2001, and references therein). XMM QE is near to the 80% from 1 keV to ~ 8 keV for the MOS 1-2 and it is about 100% from 0.5 to 10 keV for the EPIC PN; it strongly decrease above 10 keV, where also the mirrors effective area has a significant decrease.

6.2.3 NuSTAR

The NASA's Nuclear Spectroscopic Telescope Array (*NuSTAR*), launched on June 13, 2012, is the first focusing hard X-ray satellite in orbit that operates in the 3-79 keV band. Thanks to the inherently low background associated with concentrating the X-ray light, *NuSTAR* provides more than two orders of magnitude improvement in sensitivity over the previous high-energy missions that have operated at similar energies (Harrison *et al.* 2013). The observatory consists of two co-aligned grazing-incidence X-ray telescopes with a 10-m focal length. The optics implement a conical approximation to the Wolter-I design which consists of 133 highly-nested mirror shells coated with Pt/SiC and W/Si multi-layers. The combination of the low graze angle X-ray optics and the multilayer coating, enables significant collecting area to be achieved out to 78.4 keV (fig. 6.3). The angular resolution of the satellite is dominated by the optics, and is 18" FWHM, with a half power diameter (i.e. the diameter of the circle enclosing 50% of the flux) of 58". The focal plane of each *NuSTAR* telescope consists of 2×2 modules (FPMA and FPMB) of imaging CdZnTe pixel detectors, each of them segmented into 32 x 32 pixels subtending 12.5" on the sky . The detectors measure the arrival time, energy and position of interaction of each incident X-ray, with an energy resolution

of ∼0.4 keV (@10 keV), and ∼0.9 keV (@60 keV)[7].

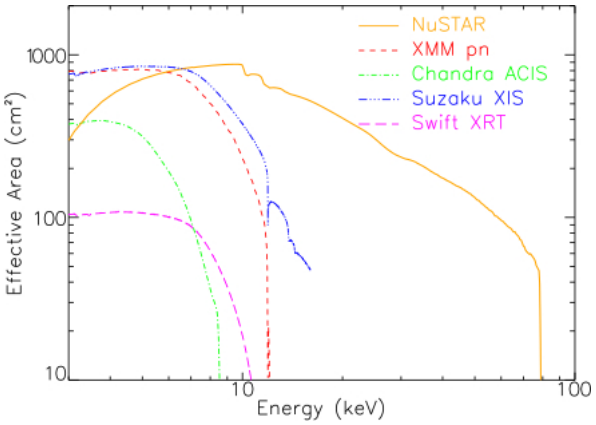

Figure 6.3: *NuSTAR* effective collecting area compared to other X-ray focusing telescopes. *NuSTAR* provides good overlap with these soft X-ray observatories and extends focusing capabilities up to 79 keV.

6.3 Chandra data

I00183 was observed by *Chandra* on 2013/02/13 with the ACIS-S detector, with an effective exposure time of 22 ks; the source was observed in *very faint* mode[8]. Data reduction was carried out using the CIAO (Chandra Interactive Analysis of Observations) software, version 4.7[9]. The analysis started from raw data which were reprocessed using the *chandra_repro* tool. Good grades and data in the 0.5−7 keV interval were selected and then the full-band image was extracted using *dmcopy* tool. The region files for the source and the background were selected visualizing the image with *ds9* viewer; an extraction region with a radius of 2 arcsec was chosen for the target and a larger nearby region for the background. The *specextract* tool was finally run to create the spectra and the ARF and RMF response matrices; the *grppha* tool from FTOOLS of HEASARC[10] was used to "group" the spectrum and due to the few number of spectral counts (133) it was chosen to group one count for bin and apply the Cash statistics[11]. The net count rate for the spectrum is 5.8×10^{-3} cts s^{-1}, 99.6% of which are source counts. The spectral analysis and fitting has been conducted with the XSPEC software[12], version 12.9.0.

[7]http://www.nustar.caltech.edu
[8]http://cxc.cfa.harvard.edu/proposer/threads/acis_notes
[9]http://cxc.harvard.edu/ciao
[10]http://heasarc.gsfc.nasa.gov/ftools/caldb/help/grppha.txt
[11]https://heasarc.gsfc.nasa.gov/xanadu/xspec/manual/XSappendixStatistics.html
[12]https://heasarc.gsfc.nasa.gov/xanadu/xspec

6.3.1 Chandra spectral models

At the beginning a simple spectral model composed of a powerlaw modified by the Galactic absorption[13] (*wabs*) was adopted. The resulting spectral fitting is shown in the upper panel of figure 6.4, while its lower panel shows the residuals between the observed and the model counts distribution in terms of the error (σ): it represents the statistical (χ) result about the "goodness" of the model chosen to fit the data. The amount of residuals in figure 6.4 suggests that a more complex modeling is needed to obtain a good fit; furthermore, a negative photon index was found from this model, $\Gamma = -0.48^{+0.27}_{-0.28}$; knowing that a typical photon index measured for an unobscured AGN and expected from theory is ~ 1.8, this could be considered as an indication of strong intrinsic absorption. For this reason, a *zwabs* component to model the intrinsic absorption at the AGN redshift, and a line component *zgauss* to model the iron emission line were added; all parameters were initially left free to vary. The resulting N_H intrinsic column density is $5.3^{+3.8}_{-2.8} \times 10^{22}$ cm^{-2} with an observed photon index $\Gamma = 1.3^{+0.9}_{-0.8}$; the center of the line was found at 6.77 ± 0.08 keV which is the rest-frame energy of the iron helium-like Kα line. The resulting spectral fitting is shown in figure 6.5. Such spectral features and the measured model parameters can be interpreted as signs of a strongly obscured AGN whose primary power law emission is flattened by the transmission through the obscuring medium (i.e. the torus) and the reflection component arises from ionized gas, with iron in the He-like Fe XXV state. Even if the phenomenological fitting shown in figure 6.5 suggests that the modeling is good, to better constrain the spectral features in this obscured object, the MYTorus (Murphy & Yaqoob 2009) physical model was adopted. It takes into account the geometry of the obscuring medium and consists of three component: one which considers the intrinsic absorption of the source and modifies the primary power law emission component, a reflection component to model the Compton reflection continuum, and the line components. However, MYTorus line component model only the 6.4 Kα and 7.1 Kβ iron lines; for this reason, in this particular case, the 6.7 keV Helium-like iron line was modeled using a single Gaussian component. The inclination angle of the source with respect the line of sight was found at 65° and frozen. The soft component visible below 2 keV in figure 6.5 is probably due to thermal emission from the host galaxy or a scattering component, and was modeled with a simple power law; it represents a simple method to model the soft emission, used when the data quality does not allow to apply a more complex and physical model. The resulting spectral fitting is shown in figure 6.6, while figure 6.7 shows the unfolded[14] spectrum, with the best-fit model represented by dotted lines. The best-fit N_H intrinsic column density was

[13]The Milky Way absorption was calculated using http://heasarc.nasa.gov/cgi-bin/Tools/w3nh/w3nh.pl web tool. The Leiden/Argentine/Bonn (LAB) Survey of Galactic HI value (3.27×10^{20} cm^{-2}) was used and then this parameter was frozen.

[14]The unfolded spectrum represent the theoretical source spectrum unfolded through the instrumental response.

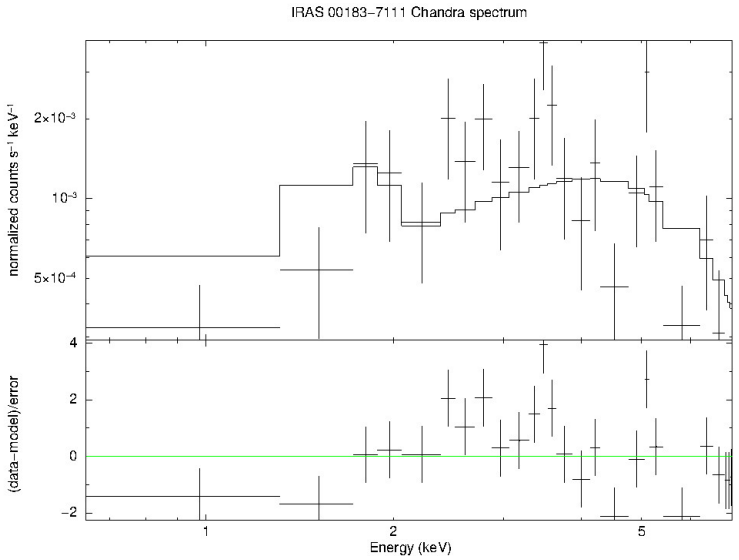

Figure 6.4: I00183 Chandra spectrum folded through the detector response with the model superimposed in the observed frame 0.5-7 keV. The model consists of a power law modified by the Galactic absorption. The bottom panel shows the residuals between the data and model counts in terms of σ. The spectrum has been rebinned for presentation purposes.

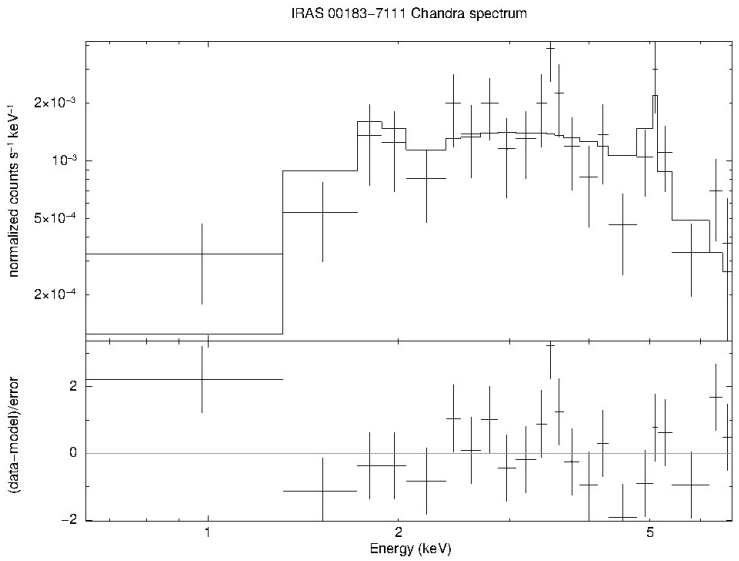

Figure 6.5: I00183 Chandra spectrum folded through the detector response with a transmission model superimposed in the observed frame 0.5-7 keV. The model consists of a power law modified by the intrinsic and the Galactic absorption plus a Gaussian line component. The bottom panel shows the residuals between the data and the model counts in terms of σ. The spectrum has been rebinned for presentation purposes.

$\sim 0.17^{+0.03}_{-0.02} \times 10^{24}$ cm^{-2} with an intrinsic photon index fixed at 1.9; the statistic is computed in a low-counting regime and to better constrain the intrinsic absorption, the photon index needs to be fixed at a typical intrinsic value. The line at 6.72 ± 0.07 keV has a rest-frame equivalent width (EW) of $\sim 0.7^{+0.4}_{-0.3}$ keV. Figure 6.8 shows the contours of confidence[15] between the line energy and its normalization. The observed best-fit model flux is $(1.54 \pm 0.03) \times 10^{-13}$ erg s^{-1} cm^{-2} in the energy range 2-10 keV, while the de-absorbed 2-10 keV rest-frame luminosity is 7.2×10^{43} erg s^{-1}. The presence of the high ionization iron line suggests an origin from highly ionized medium, thus more physical models are probably needed to account for the observed features. Due to the few number of spectral counts (133) of the *Chandra* spectrum, it was not possible to use more complex models, but they will be tested with the XMM-*Newton* spectra.

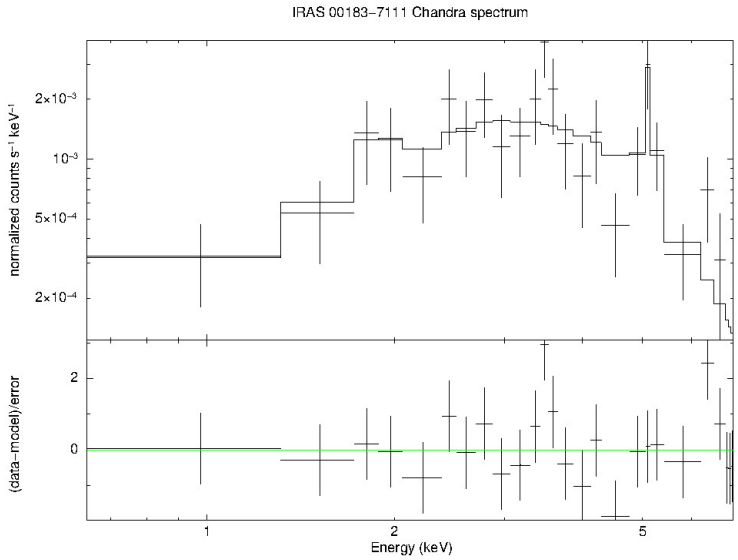

Figure 6.6: I00183 *Chandra* spectrum folded through the detector response with the best-fit model superimposed in the observed frame 0.5−7 keV. The model is composed of MYTorus to model the Compton reflection continuum and the primary power law modified by the instrinc absorption, a single Gaussian component to model the iron He-like line and a power law to model the thermal soft-excess. The bottom panel shows the residuals between the data and the model counts in terms of σ. The spectrum has been rebinned for presentation purposes.

[15]The contour plot analysis consists of performing a fit while stepping the value of one or more parameters through a given range using the XSPEC *steppar* task. They show the statistical uncertainties related to two parameters of interest.

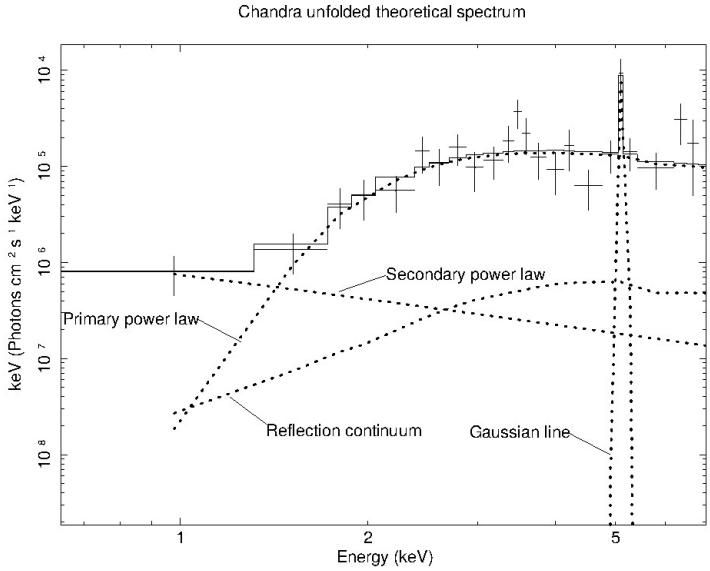

Figure 6.7: I00183 Chandra theoretical spectrum unfolded through the instrumental response, with the best-fit model superimposed in the observed energy frame 0.5−7 keV. The dotted lines represent the model components: MYTorus reflection and intrinsically absorbed primary power law components, Gaussian line and soft power law components, as labelled in the panel. The spectrum has been rebinned for presentation purposes.

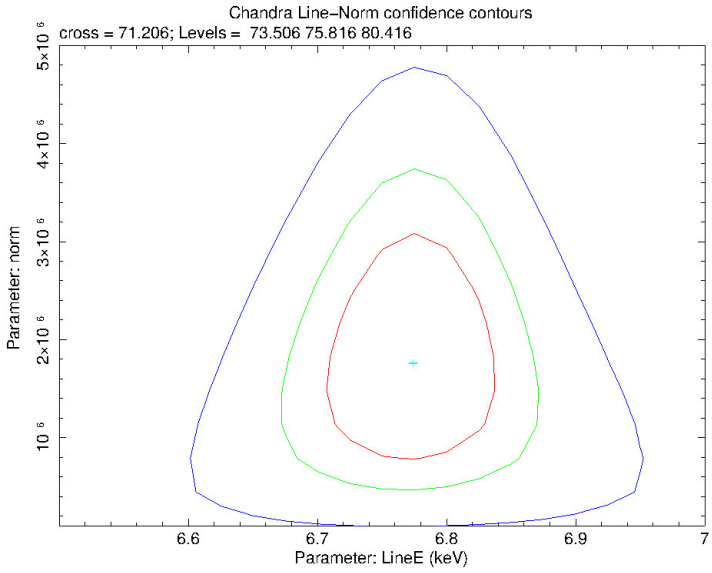

Figure 6.8: Contours of confidence for the energy of the Kα iron emission line at 6.7 keV and its normalization for *Chandra* data. The levels of confidence are shown as: 99% in blue, 90% in green and 68% in red.

6.4 XMM-Newton data

The target was observed on 2003/04/16 and the total integration time is 22.2 ks. The observation was carried out in Prime Full Window mode using a thin filter for the EPIC cameras[16]. The analysis started from the ODF (Observation Data Files) raw data and they were reprocessed using the HEASOFT Science Analysis System (SAS) software[17], version 14.0. Data reduction was carried out separately for PN and MOS1-MOS2; raw data were reprocessed using the *epproc* and *emproc* tasks, respectively. The SAS task *evselect* was used to create a light curve above 10 keV to identify interval of flaring particle background. The High Elliptical Orbit (HEO) of the XMM-*Newton* satellite allows to spend most of its orbit time beyond the radiation belts, but maximizes the possibility to intercept the Earth's magnetosphere soft protons clouds[18]. Checking for the external soft protons flares, and applying a threshold to the count rate at high-energies is the reason to make the high-energy light curve. *Tabgtigen* is the task used to select the good time intervals. Usually the selected count rate (CR) is < 0.5 counts s^{-1} for the EPIC PN and < 0.35 counts s^{-1} for the MOS 1-2. In this case, the observation appears highly noisy so that the following screening was adopted in selecting good time intervals (gti): CR< 5 counts s^{-1} for the PN and < 2 counts s^{-1} for the two MOS cameras, in order to achieve the best compromise between the SNR and the effective exposure time after selecting the gti. The PN and MOS 1-2 exposure times are 12.7 ks and 8.4 ks, respectively, after removing the periods of high background. The image of the cleaned and filtered event files was created using SAS task *evselect* and the spectra were extracted using the *especget* task. The PN spectrum was extracted within a region of radius 15 arcsec, while the MOS spectra were extracted from a region of 20 arcsec of radius, which both correspond to an Encircled Energy Fraction of $\sim 70\%$ (as shown in fig. 6.2). The two MOS 1-2 spectra were co-added using the *mathpha* task from HEASARC FTOOLS package[19] and the *grppha* task was used to group all spectra. The PN spectrum was grouped by fifteen counts for bin (spectral data counts: 289) and the MOS1-2 spectrum by seven counts for bin (spectral data counts:169); the net count rate is 1.3×10^{-2} counts s^{-1} (57.4% from the source) and 6.3×10^{-3} counts s^{-1} (63% from the source), respectively. The spectral analysis was conducted using XSPEC, version 12.9.0.

6.4.1 XMM-Newton spectral models

As in the *Chandra* case, the first adopted model, composed of a power law modified by the Galactic absorption, gives high residuals and a flat ($\sim 0.11 \pm 0.27$) photon index, suggesting the presence of a substantial obscuration. Adding the obscuration

[16]See XMM-Newton Users Handbook: https://heasarc.gsfc.nasa.gov/docs/xmm/uhb
[17]http://www.cosmos.esa.int/web/xmm-newton/sas
[18]https://heasarc.gsfc.nasa.gov/docs/xmm/uhb/epicbkgd.html
[19]http://heasarc.gsfc.nasa.gov/ftools/caldb/help/mathpha.txt

at the source redshift and a Gaussian line component, the photon index was fixed at an intrinsic value of 1.9, and the resulting line-of-sight column density is $5.2^{+1.2}_{-0.9} \times 10^{22}$ cm^{-2}. As shown in figure 6.9, the residuals in the soft X-ray band suggest the presence of an additional component below 2 keV. The line energy was found at $\sim 6.62 \pm 0.14$ keV. Using the same Chandra analysis strategy, MYTorus model was

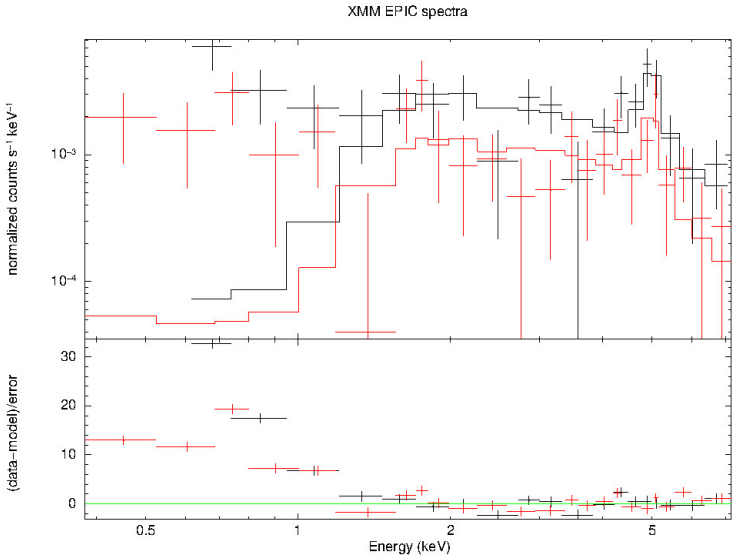

Figure 6.9: I00183 XMM EPIC spectra with the model superimposed in the observed energy frame 0.5−7.2 keV. The model consists of a power law modified by the instrinsic and the Galactic absorption and a Gaussian line component. The bottom panel shows the residuals between the data and the model counts in terms of σ. The black data counts represent the PN spectrum, the red ones are from the co-added MOS spectra.

adopted. The iron line was modeled using a single Gaussian component, and the "soft excess" with a simple power law. A normalization constant was also added to account for the cross-normalization of the different instruments: the PN constant was frozen at 1, while the MOS12 constant was left free to vary. The resulting spectral fitting folded through the instrumental response is shown in figure 6.10. The best fit N_H intrinsic column density is $0.17^{+0.07}_{-0.04} \times 10^{24}$cm^{-2} with an intrinsic photon index fixed at 1.9. The center of the line was found at 6.63 ± 0.14 keV with an EW of $1.27^{+0.65}_{-0.54}$ keV; figure 6.11 shows the confidence contours between the line energy and its normalization. The best-fit 2−10 keV observed flux is $1.47^{+0.31}_{-0.28} \times 10^{-13}$ erg s^{-1} cm^{-2}, which is consistent (within the errors) with that observed in the *Chandra* spectrum. The rest-frame 2−10 keV luminosity results 6.67×10^{43} erg s^{-1}.

MYTorus model results overall as a "good" model to reproduce the spectral shape, but the presence of the high-ionization iron emission line at 6.7 keV suggests that it could be not the best model to account for the physical involved processes. For this reason, Xillver model was then adopted (Garcia *et al.* 2010, 2013),

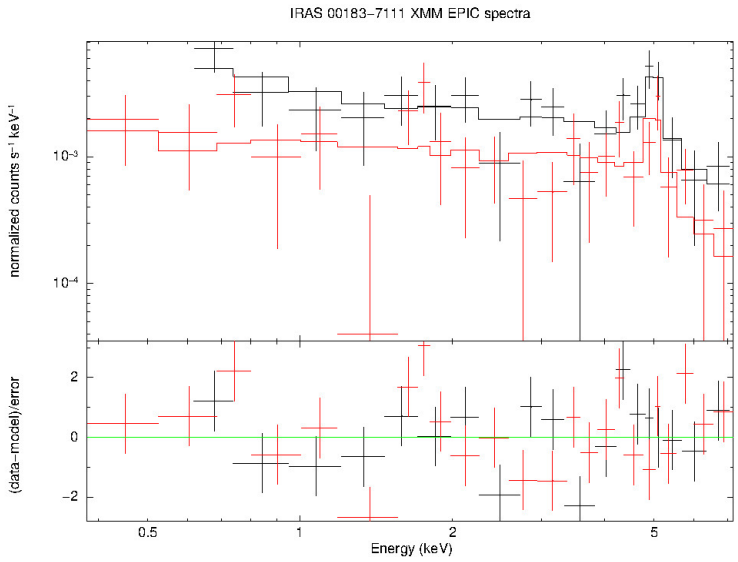

Figure 6.10: I00183 XMM EPIC spectra folded through the instrumental response with its model superimposed in the observed energy frame 0.5−7.2 keV. The model consists of MYTorus absorbed primary power law and reflection components, Gaussian line and soft secondary power law. The bottom panel shows the residual between the data and the expected counts in terms of σ. The black data counts represent the PN spectrum, the red ones are from the co-added MOS spectra.

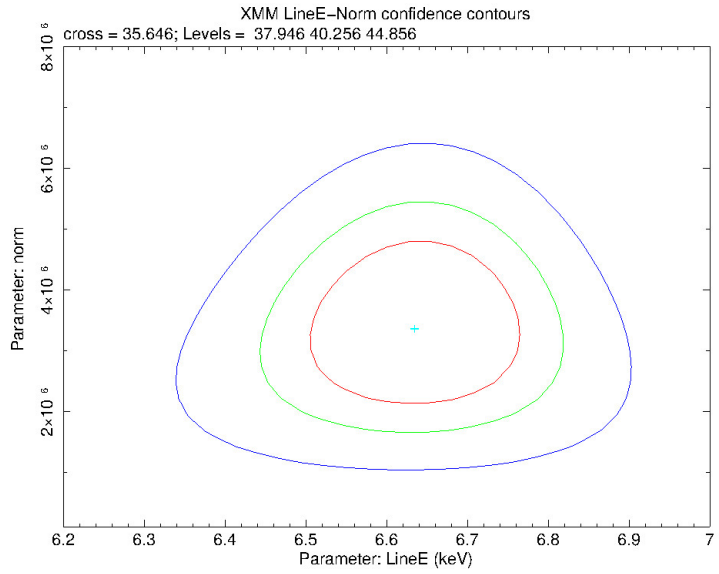

Figure 6.11: Contours of confidence for the energy of the Kα iron emission line at 6.7 keV and its normalization for XMM-*Newton* spectra. The levels of confidence are shown as: 99% in blue, 90% in green and 68% in red.

which accounts for the reflection component arising from a highly ionized medium, and provides an accurate description of the Fe K lines. The ionization state of the medium is taken into account by the so-called ionization parameter, defined as $\xi = 4\pi F_x/n$, where F is the flux of the illuminating radiation in the $\sim$0.1$-$100 keV energy range, and $n = 10^{15}$ cm^{-3} is the gas density. The ionization parameter was initially left free to vary and its best-fit value was found at $log\xi = 2.35 \pm 0.04$, suggesting the presence of a strong ionization. However, the observed spectral index is very flat and varying in the range 0$-$1, indicating that also the presence of a colder obscuring medium has to be considered. In this case, the PLCABS model (Yaqoob 1997) was tested; it represents a semi-analytic model that accounts for the transmission through an isotropic neutral medium, and enables to consider not only the absorption opacity, but also to correct the transmitted flux for non-relativistic Compton scattering. The resulting spectral fitting is shown in figure 6.12. The best-fit (reduced $\chi^2 = 1$) N_H intrinsic column density is $4.2^{+3.4}_{-2.0} \times 10^{22}$ cm^{-2} with a flat observed photon index at $1.1^{+0.15}_{-0.05}$. The resulting logξ is $2.0^{+0.3}_{-0.1}$. The de-absorbed intrinsic luminosity in the 2$-$10 keV range results 4.5×10^{43} erg s^{-1}. The derived high-ionization parameter seems to confirm that the medium surrounding the AGN, and from which the reflection arises, is highly ionized; similar ionization state are usually related to the high-radiation field produced by the AGN engine. To account for the presence of the 6.4 keV iron emission line, the typical neutral iron line that is expected in case of cold absorption (as the one traced by PLCABS), a Gaussian component was then included; the line is not statistically significant: its equivalent width upper limit is $\sim$300 eV rest-frame (90% of confidence level).

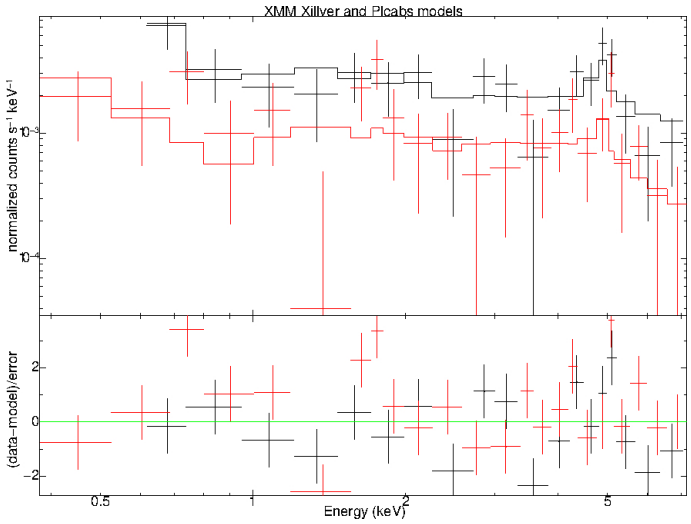

Figure 6.12: I00183 XMM EPIC spectra folded through the instrumental response with its model superimposed in the observed energy frame 0.5−7.2 keV. The model consists of XILLVER ionized reflection and PLCABS transmission through a cold obscuring medium. The bottom panel shows the residual between the data and the expected counts in terms of σ. The black data counts represent the PN spectrum, the red ones are from the co-added MOS spectra.

6.5 NuSTAR data

I00183 was observed by *NuSTAR* in two times between 21 December, 2015 and 26 April, 2016, with an effective exposure time of 115 ks. Data are still private and the reduced spectra were obtained by courtesy of the PI (K. Iwasawa). Complete results about the observations, data reduction and spectral analysis will be soon presented by Iwasawa *et al.* (in prep.). Four spectra were extracted (two observation blocks separated three months in time); they were grouped by five counts for bin, due to the few number of spectral data counts (240,218,269,201, respectively), and a Cash statistic was used. The net photon count rate is $\sim 3 \times 10^{-3}$ counts s^{-1} for the four spectra, about which 60% are from the source, on average. The spectral analysis was restricted within the 2−30 keV energy range and was conducted using XSPEC, version 12.9.0.

6.5.1 Nustar spectral models

Adopting the same strategy of *Chandra* and XMM-*Newton* spectral analysis, it was first tested if a simple power law modified by the Galactic absorption can explain the spectral shape; also a constant component was added to account for the cross-normalization between the two focal plane modules. The resulting spectral index ($\Gamma = 1.8 \pm 0.2$) is consistent with that measured for a typical unobscured AGN, but the amounts of residuals suggest that a more complex modeling is required. An

intrinsic absorption model component was then added to account for the presence of an obscuring medium along the line of sight; also a Gaussian line component was added to account for the presence of the Fe emission at 5 keV (observed). All the parameters were initially left free to vary. The derived photon index was 1.8 ± 0.2, with an intrinsic column density $> 7.0 \times 10^{22}$ cm^{-2}. The central energy of the line was 6.3 ± 0.3 keV, with an equivalent width of 285^{+270}_{-180} eV; the line strength is lower than those found in *Chandra* and XMM spectral analysis, and the central line energy results to be apparently different (see the associated errors), but this could be attributed to the significantly lower *NuSTAR* spectral resolution with respect to those of *Chandra* and XMM. For completeness, it was attempted to apply MYTorus model to test the properties of the obscuring medium beyond the energy range sampled by *Chandra* and XMM-*Newton* spectra; also a Gaussian component was added to model the weak emission at 5 keV (observed). In this case, MYTorus model does not work well in deriving robust values and errors for the parameters that characterize the torus. This model suggests a line-of-sight column density $> 5.0 \times 10^{22}$ cm^{-2}, with a photon index of 1.8 ± 0.2. The central energy of the line results 6.2±1.2 keV, with an equivalent width of 260^{+269}_{-244} eV. Finally, as in the XMM case, Xillver and PLcabs model were then tested to reproduce the spectral shape, accounting for the reflection from a strongly ionized medium and also for the transmission through a cold medium. The best-fit model ($\chi^2_{red} \sim 0.8$) is shown in figure 6.13. The resulting intrinsic column density is $8.0^{+7.0}_{-6.0} \times 10^{22}$ cm^{-2}, with a steep spectral index of 2.40 ± 0.22 and $log\xi = 1.30^{+0.11}_{-0.25}$. The rest-frame 2−30 keV luminosity is $\sim 1.3 \times 10^{44}$ erg s^{-1} cm^{-2}, with a 2−10 keV observed flux of $1.8^{+0.4}_{-0.3} \times 10^{-13}$ erg cm^2 s^{-1}, which is consistent (within the errors) with those observed in *Chandra* and XMM-*Newton* spectra.

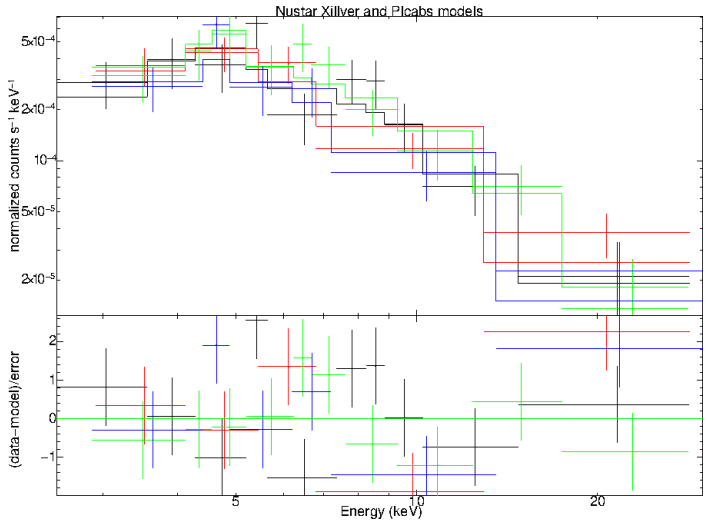

Figure 6.13: I00183 *NuSTAR* spectra folded through the instrumental response with the model superimposed in the observed energy frame 2−30 keV. The model consists of XILLVER ionized reflection and PLCABS transmission through a cold medium. The bottom panel shows the residual between the data and the model counts in terms of σ. The black, red, green and blue data counts refer to the two blocks of FPMA and FPMB spectra.

6.6 The broad-band fitting

The study of the broad-band ($\sim 0.5 - 30$ keV) X-ray properties of I00183 was finally carried out modeling together the XMM-*Newton* and *NuSTAR* spectra, to test the models that seem to describe the complex phenomena that involved this source better. Thus, starting from the results obtained by modeling the spectra individually, XILLVER model was used to account for the reflection from a ionized medium and PLCABS was used to model the intrinsic absorption. *Chandra* spectrum was not included in the broad-band analysis because of its low statistics. The best-fit ($\chi^2_{red} \sim 0.92$) derived photon index is $1.80^{+0.22}_{-0.19}$ with a line-of-sight column density of $7.1^{+2.8}_{-1.9} \times 10^{22}$ cm^{-2}. The obtained ionization parameter is $log\xi \sim 2.65^{+0.35}_{-0.91}$. The 2−10 keV rest-frame luminosity results $\sim 3 \times 10^{43}$ erg s^{-1} cm^{-2}. However, the two models do not work well in the broad-band spectrum, since the spectral fit cannot reach a proper convergence, leaving also a large amount of residuals at the line energy. For this reason, the cold absorption component was then modeled using a simpler phenomenological model composed of a power law modified by the intrinsic absorption. A power law modified only by the Galactic absorption was added to account for the "soft excess", since the low statistic below 2 keV does not allow to use a more complex modeling to reproduce the spectral shape. The resulting best-fit ($\chi^2_{red} \approx 0.9$) spectrum is shown in figure 6.14. The derived column density for the line-of-sight neutral absorber is $8.3^{+2.8}_{-1.9} \times 10^{22}$ cm^{-2}; the power law photon index

results 1.9 ± 0.2, and is consistent with the intrinsic value expected from theory for an unobscured object. The inclination angle of the ionized reflection component was initially left free to vary, and then was fixed at the best-fit value of 80°. The ionization parameter results $log\xi = 2.8^{+0.2}_{-0.1}$. The de-absorbed 2−30 keV luminosity is 1.0×10^{44} erg s^{-1}, while that in the 2−10 keV range is $\sim 6.0 \times 10^{43}$ erg s^{-1}. The observed 2−10 keV flux is of the order of $(1.5 \pm 0.3) \times 10^{-13}$ erg s^{-1} cm^{-2}. A Gaussian line component was finally tested to account for the presence of the 6.4 keV neutral iron line, but its (rest-frame) equivalent width is ∼300 eV (90% of confidence upper limit), showing that the component is not statistically significant.

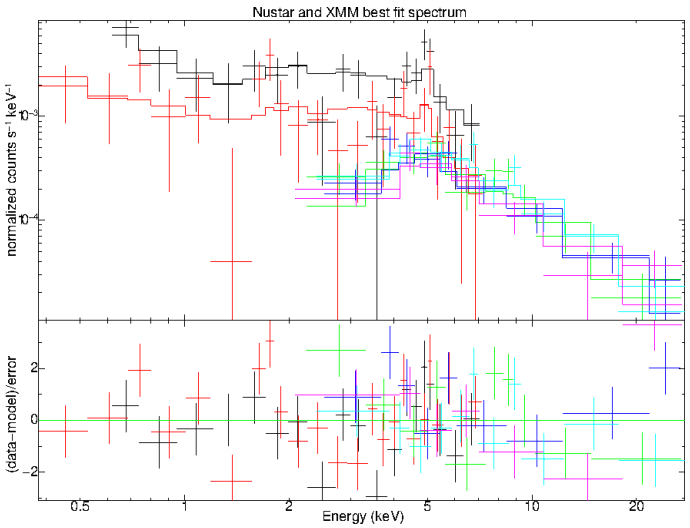

Figure 6.14: I00183 XMM-*Newton* and *NuSTAR* spectra folded through the instrumental response with the model superimposed in the observed energy frame 0.5−30 keV. The model consists of XILLVER ionized reflection and a phenomenological model of transmission through a neutral medium. The bottom panel shows the residual between the data and the model counts in terms of σ. The black and red colors refer to the XMM EPIC cameras, while the green, light blue, purple and cyan refer to the two FPMA and FPMB *NuSTAR* detectors.

6.7 Derived X-ray parameters

The best-fit X-ray parameters extracted from the spectra are summarized in table 6.1 and 6.2. In particular, table 6.1 refers to the results obtained by modeling the spectra with MYTORUS model, that accounts for the geometry of the obscuring cold medium; table 6.2 refers to the XMM-*Newton*, *NuSTAR* and the broad-band obtained parameters using XILLVER, to account for the ionized reflection, and a transmission model (PLCABS or power law modified by the intrinsic absorption).

Table 6.1: X-ray best-fit parameters obtained using MYTorus model

	Line E$^{(1)}$	**EW**$^{(2)}$	$\mathbf{N}_H^{(3)}$	**Flux**$^{(4)}$	**Luminosity**$^{(5)}$
Chandra	6.70±0.07	$0.6^{+0.4}_{-0.3}$	$0.17^{+0.05}_{-0.04}$	1.53±0.03	7.2
XMM-*Newton*	6.64±0.14	$1.27^{+0.65}_{-0.54}$	$0.17^{+0.07}_{-0.04}$	$1.47^{+0.31}_{-0.28}$	6.67
NuSTAR	6.2±1.2	$0.26^{+0.27}_{-0.24}$	> 0.05	$1.8^{+0.4}_{-0.3}$	5.68

(1) Energy of the iron emission line in keV calculated from the best spectral fitting with its errors quoted at 90% of confidence.
(2) Rest-frame equivalent width of the iron emission line in keV with errors quoted at 90% of confidence level.
(3) Intrinsic N_H column density in units of 10^{24} cm^{-2} and obtained from the best fit.
(4) Observed-frame 2-10 keV flux from the best spectral fitting in units of 10^{-13} erg cm^{-2} s^{-1}.
(5) Intrinsic rest-frame 2-10 keV luminosity from the best spectral fitting in units of 10^{43} erg s^{-1}.

Table 6.2: XMM-*Newton*, *NuSTAR*, and broad-band best-fit parameters obtained using Xillver model

	log$\xi^{(1)}$	$\Gamma^{(2)}$	$\mathbf{N}_H^{(3)}$	**Flux**$^{(4)}$	**Luminosity**$^{(5)}$
XMM-Newton	$2.0^{+0.3}_{-0.1}$	$1.12^{+0.15}_{-0.05}$	$4.2^{+3.4}_{-2.0}$	1.65±0.25	~ 4.5
NuSTAR	$1.3^{+0.11}_{-0.25}$	2.40 ± 0.22	$8.0^{+7.0}_{-6.0}$	$1.8^{+0.2}_{-0.3}$	~ 13
XMM-Newton and NuSTAR broad-band fitting (0.5−30 keV)					
	$2.8^{+0.2}_{-0.1}$	$1.86^{+0.19}_{-0.16}$	$8.34^{+2.8}_{-1.9}$	1.5 ± 0.3	~ 6.1

(1) Ionization parameter derived from the best fit, with its errors quoted at 90% of confidence.
(2) Photon index derived from the best-fit with errors quoted at 90% of confidence level.
(3) Intrinsic N_H column density in units of 10^{22} cm^{-2} and obtained from the best fit.
(4) Observed-frame 2-10 keV flux from the best spectral fitting in units of 10^{-13} erg cm^{-2} s^{-1}.
(5) Intrinsic rest-frame 2-10 keV luminosity from the best spectral fitting in units of 10^{43} erg s^{-1}.

The X-ray luminosity and the SFR

The X-ray observations of I00183 confirm the presence of a powerful source coincident with the nucleus, with a large de-absorbed intrinsic 2−10 keV luminosity ($\simeq 6 \times 10^{43}$ erg s^{-1} in the XMM and *NuSTAR* simultaneous fitting). This luminosity exceeds the range usually observed in heavily obscured AGN detected in nearby ULIRGs ($< 10^{42} - 10^{43}$ erg s^{-1}, e.g. Lonsdale *et al.* 2006), and may be consistent with the scenario proposed by Norris *et al.* (2012) for which the quasar has just switched on in the center of I00183 and started boring its way through the surrounding medium, proceeding to its bright, unobscured phase. The I00183 X-ray spectrum also shows an excess of emission below 2 keV, which is a typical expected features for AGN hosted in star-forming galaxies (e.g. Nardini *et al.* 2010). The statistics is too low to use a proper modeling to reproduce the "soft-excess" and carry out a deep investigation about its origin, but a simple power law modified by the Galactic absorption gives a good fit to the 0.5−2 keV data. The rest-frame absorption-corrected 0.5−2 keV luminosity is $L_{SX} \simeq 3.6 \times 10^{42}$ erg s^{-1}, more luminous than classical nearby ULIRGs (Iwasawa 1999). By assuming that the soft-band emission could be solely powered by the nuclear starburst, an estimate of the expected SFR was computed using Ranalli *et al.* (2003):

$$SFR = 2.2 \times 10^{-40}\ L_{0.5-2keV}\ M_{\odot}\ yr^{-1} \tag{6.8}$$

The so-computed SFR is ~ 800 M$_{\odot}$ yr^{-1}, which is 4 times higher that that inferred from the relation between the CO and the IF luminosity of the starburst component (~ 180 M$_{\odot}$ yr^{-1}, see Section 5.5.2). This may tells that the observed soft emission in the 0.5−2 keV range cannot be attributed only to thermal emission from the star forming activity, but also to a significant scattering component related to the powerful AGN activity. The result can be considered in agreement with the fact that the bolometric luminosity of I00183 (9×10^{12} L$_{\odot}$, mostly radiated at infrared wavelengths, Spoon *et al.* 2009) is predominantly powered by the AGN, which accounts for $> 80\%$ of it (Nandra & Iwasawa 2007), while only 14% of the total power of I00183 is contributed by star-formation (Mao *et al.* 2014).

The He-like iron line

The X-ray spectrum of I00183 shows a He-like iron line at ~ 6.7 keV with a large EW (~ 1 keV), constrained from *Chandra* and XMM-*Newton* spectra. The presence of this feature suggests that the reflection component arises from highly ionized matter. To account for this detection, a ionized reflection analytic model was used, and the obtained best-fit logξ (ionization parameter) is ~ 2.8. It is worth noting that the use of self-consistent analytic models, such the recent XILLVER, allows the study of the ionized reflection component with greater accuracy with respect to the previous published X-ray analysis of I00183 (e.g. Nandra & Iwasawa 2007). The

obtained result is consistent with the presence of matter in highly ionized state, probably related to the intense radiation field produced by the nuclear engine.

The cold absorber

One of the main goals of this Thesis work was to derive whether the molecular gas traced by the CO and observed with ALMA could be considered responsible at least in part for the obscuration observed in band X. The line-of-sight column density derived from the CO detection is $(8.0 \pm 0.9) \times 10^{21}$ cm^{-2}, while that obtained from the best-fit X-ray spectrum is $N_H \simeq 8.3^{+2.8}_{-1.9} \times 10^{22}$ cm^{-2}. The difference by one order of magnitude could be consistent with the approximations used computing the column density from the CO detection: assuming a H_2 mass-to-CO luminosity ratio typical for ULIRGs ($\alpha = 0.8$, see Section 5.2.1), the column density was evaluated from a gas mass which accounts only for the molecular gas H_2, since the mass of the atomic hydrogen is unknown. This factor leads to underestimate the gas mass and, in turn, the column density; for this reason, the results obtained in the two energy bands could be considered broadly consistent.

Discussion

The nuclear regions of I00183 appears stratified in different layers of matter, extending from the nuclear power source: one hotter and highly ionized, close to the AGN, and mostly inferred by the presence of the iron in the He-like Fe XXV state; the other colder and outer, which accounts for the presence of a cold absorbing medium extending up to 2 kpc from the nucleus (see Section 5.4.2), and mostly related to the presence of high amounts of molecular gas around the nuclear regions. This scenario is also consistent with that proposed by Spoon *et al.* (2004) by studying the mid-infrared $4-30$ μm spectrum of I00183. They identified two layers of obscuring material: a cold outer shell responsible for ice and silicate absorption, and a warm inner shell. In particular, the thickness of the inner shell is constrained to be smaller than 0.03 pc, with an extension of $\sim 0.5 - 2$ pc from the nucleus; the estimated equivalent hydrogen column density was of the order of $\sim 10^{23}$ cm^{-2}, for both shells. The involved scales in the Spoon *et al.* observations are different than ours, but the properties of the matter in the nuclear regions of I00183 can be reasonably considered consistent. However, the poor data quality in the $2-10$ keV X-ray band does not allow us to draw firm conclusions about the complex mechanisms that occur in the inner regions of this source; the purpose is to apply in future for longer $0.5-10$ keV observations of I00183, to carry out a deeper analysis of the broad-band X-ray properties of this source.

Summary and conclusions

The scientific purpose of the present work was to study the multi-frequency properties of the Ultra Luminous infrared Galaxy IRAS 00183-7111 (I00183), lying at z= 0.327; one of the main goal was to estimate if the molecular gas traced by the CO can be responsible for the obscuration observed in X-ray. Most of ULIRGs are known to host a heavily obscured AGN in its nuclear regions, and this fraction increases at increasing infrared luminosity. The detection of the most heavily obscured sources is crucial to shed light on the obscured accretion phase in black hole growth, the AGN/host galaxy co-evolution issue, and eventually estimate the contribution of these sources to the X-ray cosmic background.

Context

I00183 was selected from the so-called Spoon diagnostic diagram (Spoon *et al.* 2007) which compares the strength of the 9.7 μm silicate absorption feature and the equivalent width of the 6.2 μm Polycyclic Aromatic Hydrocarbon (PAH) emission feature to investigate about the AGN/starburst components in ULIRGs. I00183 was selected from the top-left region of the diagram, where the sources with strong silicate absorption features (i.e. absorption-dominated sources) are located.
Observations at various wavelengths reveal the peculiar nature of I00183. Its mid-infrared spectrum lacks the typical AGN tracers (e.g. the 7.65 μm [Ne IV], and the 14.3 and 24.3 μm [Ne V] emission lines), but the presence of a powerful AGN source in its nuclear regions was already established at others wavelengths. Especially important in this respect was the detection by Nandra & Iwasawa (2007) of a 6.7 keV Fe Kα line (Fe XXV) with a large equivalent width, indicating the presence of a highly obscured AGN in I00183. Another clear indication is a higher than expected radio power ($L_{4.8\ GHz} \sim 10^{25.4}$ W Hz^{-1}) based on the radio-far-infrared correlation for starburst galaxies, that places I00183 within the regime of high luminosity radio galaxies (FRII-class, Roy & Norris 1997). More recently, Norris *at al.* (2012) reported the VLBI detection of a core-jet radio loud AGN in I00183, with jets only 1.7 kpc long. Furthermore, Spoon *et al.* (2009) detected the presence of a nuclear outflow in I00183 traced by high-velocity ($\sim$ 3000 km s^{-1}) ionized and blueshifted 12.81 μm [Ne II] and 15.51 μm [Ne III] emission lines. By comparing the combined [Ne II] and [Ne III] luminosity and the combined 6.2 and 11.2 μm PAH luminosity for

a large sample of AGNs, ULIRGs, and starburst galaxies, they have found unusual excitation conditions (i.e. 8 time stronger neon lines) compared to the typical ratio for the sample, and consistent with an origin in fast shocks ($v > 500$ km s^{-1}) in a dense environment: it was considered as a tracer of the (partial) disruption of the obscuring medium around a buried AGN. All these characteristics place I00183 in an evolutionary scenario in which it appears to have been caught in the brief transition period as a radio-loud AGN switches on in the center and starts boring its way through the dense dust and gas layers surrounding it. The lack of the classical signs of AGN at optical and IR wavelengths is attributed to the many magnitude of dust extinction accompanying the starburst activity (~ 220 M$_\odot$ yr^{-1}, Mao *et al.* 2014).

Methods and main results

To link the sub-mm to the X-ray properties of I00183, ALMA archival Cycle 0 observations in Band 3 ($\sim$87 GHz) and Band 6 ($\sim$ 270 GHz) were calibrated and analyzed. It is worth noting that significant improvements were obtained by the detailed analysis carried out in this work, with respect to the available archival products; in particular: more reliable flux calibration, thanks to the use of the latest model library releases; more accurate frequency-dependent calibration, allowing to better isolate the line from the continuum emission; significant improvement in the dynamic range of the obtained products (e.g. from 500 to 800 in Band 6 continuum images); emission from HCN molecular gas observed in Band 6 with a detection significance of $\sim 5\sigma$, higher than that claimed by Imanishi & Nakanishi (2014), using the same data.
A $CO_{(1-0)}$ emission was successfully detected in Band 3, with an integrated flux density of (2.56 ± 0.11) Jy km s^{-1}, from which a H_2 mass of $(1.14 \pm 0.10) \times 10^{10}$ M$_\odot$ was computed. The molecular gas column density along the line of sight was estimated to be $N(H_2) \approx (8.0 \pm 0.9) \times 10^{21}$ cm^{-2}, assuming a very simple geometrical model. Furthermore, a SFR of ~ 180 M$_\odot$ yr^{-1} was derived using the empirical relation between the CO and the far-infrared luminosity attributed to the starburst component. The weak HCN emission line was found at 266.7 GHz, but its poor detection significance ($\sim 5\sigma$) does not allow us to derive the properties of the cold and dense molecular gas that it traces. The continuum emission of I00183 was sampled in three different frequency ranges, centered at 87, 260 and 270 GHz, with integrated flux densities of 3.4, 2.6 and 2.2 mJy, respectively. Since the thermal emission from dust is expected to significantly increase at increasing frequency, the opposite observed behavior suggests an origin from the tail of the radio synchrotron emission rather than thermal emission from dust. An offset of $\sim 0.53 \pm 0.08$ arcsec ($\sim 2.50 \pm 0.38$ kpc) between the continuum and the CO line emission has been also observed, and seems to be consistent with the jet length (1.7 kpc) of the radio-loud source detected from Norris *et al.* (2012) VLBI observations.
The X-ray analysis was carried out using *Chandra*, XMM-*Newton*, and *NuSTAR*

data, allowing a broad-band coverage of the X-ray spectrum (0.5−30 keV). The spectra were firstly analyzed individually, showing similar spectral shape and consistent observed fluxes (within the errors), thus XMM-*Newton* and *NuSTAR* data were then used for a simultaneous X-ray spectral fitting. The analysis started from simple, phenomenological fit that confirmed the presence of an obscured AGN with a strong (equivalent width$\sim$ 1 keV) 6.7 keV helium-like iron line. Using MyTORUS, a physical model which takes into account the geometry of the obscuring medium, a N_H intrinsic column density of $\sim 1.7\times10^{23}$ cm^{-2} and a very good fit to the data were obtained. Also a soft excess (below 2 keV) was observed in the spectra, probably due, at least in part, to thermal emission from the host galaxy, expected in case of star formation. The detection of the He-like line (Fe XXV) suggests that the reflection arise from a strongly ionized medium and, for this reason, Xillver model was then tested to reproduce the broad-band spectral shape, along with Plcabs, which accounts (with a proper treatment of scatterings) for the transmission through a neutral medium. The soft emission (below 2 keV) was modeled by a simple power law modified only by the Galactic absorption, since the low spectral statistics does not allow to test more complex (thermal) models. It is worth considering that the use of self-consistent semi-analytic models, such as the recent Xillver, allows us the study of a possible ionized reflection with greater accuracy with respect to the previous published X-ray analysis of I00183 (e.g. Nandra & Iwasawa 2007). However, due to problems with a proper convergence of the fit, the best-fit was obtained using a simple transmission model composed of a power law modified by the intrinsic absorption, rather than using the more complex Plcabs model. The derived results suggest the presence of a powerful source of radiation which ionizes the surrounding medium with a resulting ionization parameter log$\xi = 2.8$; the photon index is consistent with that expected from theory ~ 1.8, with an intrinsic N_H column density of $\sim 8 \times 10^{22}$ cm^{-2}. The difference of one order of magnitude with respect to that estimated using the 87 GHz CO detection ($\approx 8.0 \times 10^{21}$ cm^{-2}) can be consistent with the approximation used to compute this column density: it was evaluated considering only the molecular gas mass (H_2), since the mass of the atomic hydrogen is unknown, leading to underestimate the line-of-sight column density. A de-absorbed intrinsic 2−10 keV luminosity of $\sim 4 \times 10^{43}$ erg s^{-1} was derived, which is slightly higher than those usually observed in nearby AGN-dominated ULIRG ($L_{2-10\ keV} < 10^{42} - 10^{43}$ erg s^{-1}, e.g. Lonsdale *et al.* 2006); this may be consistent with the scenario proposed by Norris *et al.* (2012) for which the quasar has just switched on in the nuclear regions of I00183 and started boring its way through the surrounding medium, proceeding to its bright unobscured phase. Furthermore, a de-absorbed intrinsic luminosity of $\sim 4 \times 10^{42}$ erg s^{-1} was derived in the 0.5−2 keV range; assuming that it is solely powered by the starburst nuclear activity, this would imply a SFR$>$ 800 M$_\odot$ yr^{-1}, which is more than 4 times higher than that derived from the CO luminosity. This may tells that the observed excess below 2 keV can be attributed to a combination of thermal emission related to the

nearby star forming regions, and a significant scattering components related to the powerful nuclear accretion activity. However, the spectral data counts in the soft X-ray regime it too low to properly analyze its properties, and the purpose is to carry out a more detailed analysis in future by planning deeper and (on a quality level) better X-ray observations of this source.

Conclusions

The millimeter and X-ray properties of I00183 derived from this Thesis work seems to confirm the complex structure of the inner regions of I00183: the source appears to have different layers of matter, extending from a powerful nuclear engine; the inner regions are highly ionized by the strong radiation field of the AGN, while the outer layers are composed of colder gas, which extends up to 2 kpc from the nucleus and is responsible of a significant obscuration of the AGN, and a star formation rate of ~ 180 $M_{\odot}$ yr^{-1}. Similar results were obtained from the analysis of the $4-27$ μm spectrum of I00183 by Spoon *et al.* (2004), which identified two layers of obscuring material: a cold, outer shell with an estimated equivalent hydrogen column density of the order of $\sim 10^{23}$ cm^{-2}, and a warm, inner shell with an estimated thickness of 0.03 pc, and a location at $\sim 0.5-2$ pc from the nucleus. The involved scales could be reasonably different from those considered by Spoon *et al.* (2004), and the data quality does not allow us deep studies about the morphology of the inner regions of I00183, but both scenarios seem to be in agreement from each other. Finally, in view of all the discussed properties, the observed shift between the line and the continuum emission in ALMA Band 3, which can be reasonably attributed to the "newborn" jets of the central radio-loud source, can be considered as an evidence of the interplay between the AGN and its host galaxy. Similar results highlight the importance of these studies, not only to better understand the nature of local ULIRGs themselves, but also to improve the knowledge about the interplay and mutual feedback between star formation and black hole accretion, which are basic ingredients of galaxy formation and evolution.

Future perspectives

An outflow was tentatively detected by analyzing the velocity dispersion map of the CO line emission but a detailed study of the gas kinematic was not possible due to the low spectral resolution of Band 3 observation ($\sim$ 90 km s^{-1}). We plan to apply for future ALMA observations with higher spectral resolution, using the unprecedented capabilities of ALMA for the next observing cycles in terms of sensitivity and spatial resolution. In the next ALMA Cycle 5 we will attempt to investigate the $CO_{(1-0)}$ kinematic in the same Band (Band 3, 87 GHz as the representative frequency) with a spectral resolution of at least $\sim$ 15 km s^{-1}. By using the ALMA Observing Tool[20] (OT), it was estimated that this calls for a time-

[20]https://almascience.eso.org/proposing/observing-tool

on-source of ~ 5 hours, achieving an rms of ~ 0.2 mJy (comparable to that of the CO detection analyzed in this work). Furthermore, the inner regions of I00183 can be observed with better angular resolution (~ 0.3 arcsec, i.e. ~ 1 kpc), by using the highly extended array configuration available for Cycle 5 (up to 12 km as the maximum baseline length); this will allow us to also deeper investigate the nuclear continuum emission of I00183.

Bibliography

[1] Alexander, D. M., Hickox, R. C. 2012, NewAR, 56, 93

[2] Antonucci, R. 1993, ARA&A, 31, 473

[3] Armus, L., Heckman, T., M. & Miley, G., K. 1989, ApJ, 347, 727

[4] Arnaud, K., Dorman, B. & Gordon, C. 2015, *An X-ray Spectral Fitting Package, User's Guide for Version 12.9.0*, HEASARC

[5] Asayama, S., Biggs, A., de Gregorio, I. *et al.* 2016, *ALMA Cycle 4 Technical Handbook*, ALMA Partnership

[6] Bolatto, A., D., Wolfire, M. & Leroy, A., K. 2013, ARA&A, 51, 207

[7] Butler, B. 2012, ALMA memo 594

[8] Berta, S., Lutz, D., Genzel, R. *et al.* 2016, A&A, 587, 73

[9] Carilli, C., L., Riechers, D., Walter, F. *et al.* 2013, ApJ, 763, 120

[10] Carilli, C., L. & Walter, F. 2013, ARA&A, 51, 105,

[11] CASA *Synthesis & Single Dish Reduction, Reference Manual & Cookbook*, V. April 11, 2016, NRAO

[12] Clark, B. G. 1980, A&A, 89, 377

[13] Conway, J. 2004, ALMA memo 503

[14] Dasyra, K., M., Tacconi, L., J., Davies, R., I. *et al.* 2006, ApJ, 651, 835

[15] Di Matteo, T., Springel, V. & Hernquist, L. 2005, Nature, 433, 604

[16] Downes, D. & Solomon, P., M., 1998, ApJ, 507, 615

[17] Draine, B., T. & Li, A. 2007, ApJ, 657, 810

[18] Drake, C., L., McGregor, P., J. & Dopita, M., A. 2004, AJ, 128, 955

[19] Ferrarese, L. & Merritt, D. 2000, ApJ, 539, L9

[20] Transceschini, A., Braito, V., Persic, M. *et al.* 2003, MNRAS, 343, 1181

[21] Gao, Y. & Solomon, P., M. 2004, ApJ, 606, 271

[22] Fabian, A., C. 2012, ARA&A, 50, 455

[23] Farrah, D., Rowan-Robinson, M., Oliver, S. *et al.* 2001, MNRAS, 326, 1333

[24] Farrah, D., Lonsdale, C. J., Borys, C. *et al.* 2006, ApJ, 641, L17

[25] Farrah, D., Bernard-Salas, J., Spoon, H., W., W. *et al.* 2007, ApJ, 667, 149

[26] Fruscione, A. *et al.* 2006, *Chandra's data analysis system*, SPIE, 6270, 1

[27] Gaetz, T., J. & Jerius, D. 2005, http://cxc.harvard.edu/cal/Hrma/UsersGuide.html

[28] Garcia, J. & Kallman, T., R. 2010, ApJ, 718, 695

[29] Garcia, J., Dauser, T., Reynolds, C., S. *et al.* 2013, ApJ, 768, 146

[30] Genzel, R., Lutz, D., Sturm, E. *et al.* 1998, ApJ, 498, 579

[31] Gilli, R., Comastri, A. & Hasinger, G. 2007, A&A, 463, 79

[32] Gilli, R., Norman, C., Vignali, C. *et al.* 2014, A&A, 562, 67

[33] Griffin, M., J. & Orton, G., S. 1993, Icar, 105, 537

[34] Hamaker, J., P., Bregman, J., D. & Sault, R., J. 1996, Astronomy and Astrophysics Supplement, v.117, 137

[35] Harrison, F., A., Craig, W., W., Christensen, F., E. *et al.* 2013, ApJ, 770, 103

[36] Heckman, T., M., Armus, L. & Miley, G., K. 1990, ApJS, 74, 833

[37] Högbom, J. A. 1974, A&AS, 15, 417

[38] Hopkins, P., F., Hernquist, L., Cox, T., J. *et al.* 2005, ApJ, 630, 705

[39] Hopkins, P., F., Hernquist, L., Cox, T., J. *et al.* 2008, ApJS, 175, 356

[40] Hopkins, P., F., Hernquist, L., Cox, T., J. *et al.* 2008, ApJ, 679, 156

[41] Imanishi, M., Nakanishi, K., Tamura, Y. *et al.* 2009, AJ, 137, 3581

[42] Imanishi, M., Nakagawa, T., Shirahata, M. *et al.* 2010, ApJ, 721, 1233

[43] Imanishi, M. & Nakanishi, K. 2014, AJ, 148, 9

[44] Imanishi, M. & Nakanishi, K. 2016, PASJ, 58, 813

[45] Jansen, F., Lumb, D., Altieri, B. *et al.* 2001, A&A, 365, L1

[46] Jewell, P. R., & Mangum, J. G. 1997, MMA memo 170

[47] Kennicutt, R., C., Jr. 1998, ARA&A, 36, 189

[48] Kormendy, J. & Ho, L., C. 2013, ARA&A, 51, 511

[49] Kormendy, J. & Richstone, D. 1995, ARA&A, 33, 581

[50] Lipari, S., Terlevich, R., Díaz, R., J. *et al.* 2003, MNRAS, 340, 289

[51] Lister, M., L., Aller, M., Aller, H. *et al.* 2011, ApJ, 742, 27

[52] Lonsdale, C., J., Farrah, D. & Smith, H., E. 2006, AsUp book, 285

[53] Magorrian, J., Tremaine, S., Richstone, D. *et al.* 1998, AJ, 115, 2285

[54] Maiolino, R., Comastri, A., Gilli, R. *et al.* 2003, MNRAS, 344, L59

[55] Maiolino, R., Gallerani, S., Neri, R. *et al.* 2012, MNRAS, 425, L66

[56] Mao, M., M., Norris, R., P., Emonts, B. *et al.* 2014, MNRAS, 440, L31

[57] Moore, L. E. *et al.* 2004, Icar, 172, 503

[58] Murphy, K., D. & Yaqoob, T. 2009, MNRAS, 397, 1549

[59] Nandra, K. & Iwasawa, K. 2007, MNRAS, 382, L1

[60] Nardini, E., Risaliti, G., Watabe, Y. *et al.* 2010, MNRAS, 405, 2505

[61] Nardini, E. & Risaliti, G. 2011, MNRAS, 415, 619

[62] Nikolic, B., Bolton, R., C., Graves, S., F. *et al.* 2013, A&A, 552, 104

[63] Norris, R., P., Lenc, E., Roy, A., L., Spoon, H., W., W. 2012, MNRAS, 422, 1453

[64] Norris, R., P., Mao, M., Y., Lenc, E. *et al.* 2013, in Proceedings of the conference: *The Interstellar Medium in High Redshift Galaxies Comes of Age*, NRAO Conference Series, Vol. 28, ed. J. G. Mangum

[65] Omont, A., Cox, P., Bertoldi, F. *et al.* 2001, A&A, 374, 371

[66] Ranalli, P., Comastri, A. & Setti, G. 2003, A&A, 399, 39

[67] Rigopoulou, D., Spoon, H., W., W., Genzel, R. *et al.* 1999, AJ, 118, 2625

[68] Roy, A., L. & Norris, R., P. 1997, MNRAS, 289, 824

[69] Rowan-Robinson, M. 2000, MNRAS, 316, 885

[70] Ruiz, A., Carrera, F., J. & Panessa, F. 2007, A&A, 471, 775

[71] Ruiz, A., Risaliti, G, Nardini, E. *et al.* 2013, A&A, 549, 129

[72] Rupke, D., S. & Veilleux, S. 2005, ApJ, 631, L37

[73] Rupke, D., S. & Veilleux, S. 2013, ApJ, 775, L15

[74] Sanders, D., B. & Mirabel, I., F. 1996, ARA&A, 34, 749

[75] Sanders, D. B., Surace, J. A. & Ishida, C. M. 1999, IAUS, 186, 289

[76] Solomon, P. M. & Vanden Bout, P. A. 2005, ARA&A, 43, 677

[77] Somerville, R., S. 2008, ASPC, 399, 391

[78] Spoon, H, W., W., Armus, L., Cami, J. *et al.* 2004, ApJS, 154, 184

[79] Spoon, H., W., W., Marshall, J., A., Houck, J., R. *et al.* 2007, ApJ, 654, L49

[80] Spoon, H., W., W., Armus, L., Marshall, J., A. *et al.* 2009, ApJ, 693, 1223

[81] Strüder, L., Briel, U., Dennerl, K. *et al.* 2001, A&A, 365, L18

[82] Surace, J., A. et al. 1998, ApJ, 492, 116

[83] Surace, J., A., Sanders, D., B. & Evans, A. S. 2000, ApJ, 529, 170

[84] Schwab, F. R. 1984, AJ, 89, 1076

[85] Taylor, G., B., Carilli, C., L. & Perley, R., A. 2008. *Synthesis Imaging in Radio Astronomy II*, Astronomical Society of the Pacific Conference Series, V. 180

[86] Tran, H., D., Lyke, J., E. & Mader J., A. 2011, ApJ, 726, L21

[87] Treister, E., Urry, M., C., Schawinskiet, K. *et al.* 2010, ApJ, 722, L238

[88] Turner, M., J., L., Abbey, A., Arnaud, M. *et al.* 2001, A&A, 365, L27

[89] Urry, M., C. & Padovani, P. 1995, PASP, 107, 803

[90] *Users Guide to the XMM-Newton Science Analysis System*, Issue 10.5, 2014, ESA: XMM-Newton SOC

[91] Veilleux, S., Kim, D., C. & Sanders, D. B. 2002, ApJS, 143, 315

[92] Veilleux, S. 2003, in ASP Conference Series, Vol. 290, Active Galactic Nuclei: From Central Engine to Host Galaxy, ed. S. Collin, F. Combes, & I. Shlosman, 11

[93] Vilaro, B., V. 2011, *ALMA Cycle 0 Technical Handbook*, ALMA Partnership

[94] Wagg, J., Wiklind, T., Carilli, C., L. *et al.* 2012, ApJ, 752, L30

[95] Weisskopf, M., C., Tananbaumb, H., D., Van Speybroeckb, L., P. & O'Dell, S., L. 2000, SPIE, 4012, 2

[96] Yaqoob, T. 1997, ApJ, 479, 184

[97] Zheng, X., Z. 2013, in Proceedings IAU Symposium, No. 295, 2012, ed. D. Thomas, A. Pasquali, I. Ferreras

Acknowledgements

I apologize to foreign readers, but I need to write my personal acknowledgements in my mother tongue.
É giunto dunque il momento dei ringraziamenti...e se sono arrivata a scrivere questi, vuol dire che sono quasi alla fine di questo mio percorso. Ho pensato tanto in questi 10 mesi al momento in cui mi sarei ritrovata a scrivere i miei "grazie", e tutte le volte avevo paura che me ne sarei dimenticata qualcuno, o che non avrei trovato le parole giuste per esprimermi. Ma iniziamo con ordine...
Prima di tutto, ringrazio sentitamente il professor Cristian Vignali, per aver creduto in questo progetto fin dall'inizio, per la sua estrema precisione, per essere stato reperibile anche ad orari improponibili, e perchè il suo sostegno e contributo scientifico sono stati fondamentali per la riuscita del lavoro. Un grazie infinito al dottor Arturo Mignano, per tutto quello che mi ha insegnato, per avermi SUpportato e SOpportato in questo lungo periodo di tesi, e per la sua estrema dedizione e comprensione. Grazie a Rosita Paladino, Nuria Marcelino e tutti i membri dell'ARC italiano, per la loro disponibilità e gentilezza. Grazie anche alla dottoressa Paola Grandi e a Eleonora Torresi, per il loro prezioso aiuto. Infine, grazie a tutti quelli che in questi mesi di lavoro all'IRA hanno dato il loro contributo, a partire dai tecnici, fino a chiunque abbia speso anche solo un secondo del suo tempo per aiutarmi, in qualsiasi modo, a continuare il mio percorso.
Ed ora la parte più "delicata", quella per cui io stessa faccio fatica a non emozionarmi mentre scrivo. Il mio primo, incommensurabile GRAZIE va alle certezze della mia vita; a mio padre, a cui riesco solo a dire: GRAZIE PAPÁ, perchè senza di te, senza i tuoi sacrifici e il tuo appoggio, non avrei mai potuto coronare il sogno di provare a diventare un'astrofisica, e non avrei mai potuto vivere fino ad oggi con la certezza che non mi mancasse mai nulla per essere felice; e a mia madre, la mia roccia, colei che mi ha insegnato a sorridere sempre, nonostante tutto e tutti: GRAZIE MAMMA, per avermi insegnato ad essere forte, determinata e combattiva, e a rialzarmi sempre, anche quando sembra impossibile. Grazie a voi due per avermi fatto diventare quello che sono, per avermi dato la forza quando mi mancava, e per avermi fatto sempre e comunque sentire immensamente amata. Un GRAZIE dal profondo del mio cuore all'altra certezza della mia vita, a mio zio Giuseppe, per amarmi come una figlia e per essere presente, sempre. GRAZIE zio, perchè senza di te non avrei mai potuto affrontare questi otto anni di università allo stesso modo. Grazie anche ai miei fratelli, Alessio ed Emanuele, per il semplice fatto di esistere, e per avermi regalato la gioia, in questi anni, di diventare zia dei miei tre meravigliosi nipoti. Un doveroso e sentito ringraziamento anche ad Antonio Felice Maria Furchì, il mio pranoterapeuta, amico, consigliere, la persona che più di tutte mi segue e mi sostiene, e che mi sta aiutando ad arrivare alla fine del mio percorso universitario nel migliore dei modi.
Ed ora passiamo agli amici...il primo grazie va a Virginia, "la mia amica stor-

ica dell'universitá", perchè da otto anni a questa parte ci siamo sempre l'una per l'altra, sostenendoci a vicenda e gioendo dei rispettivi piccoli successi, e perchè in quest'ultimo delicato periodo è riuscita a starmi ugualmente accanto, nonostante fosse fisicamente dall'altra parte dell'Oceano. Ringrazio dal profondo del cuore Beatrice, la mia "anima gemella", per esserci tenute per mano in questi mesi, condividendo le nostre gioie, ansie e dolori e per essere l'altra parte di me, quella con cui le parole, spesso, sono superflue. Grazie a Matteo, per aver condiviso con me gli anni più belli di convivenza universitaria, e perchè, nonostante il suo essere burbero (e tendenzialmente asociale), sa sempre esserci al momento giusto, dimostrandomi, a modo suo, tutto il suo affetto. Grazie a Fulvia, per il suo essere sempre presente e attenta, e per avermi "soccorso" nei momenti più disperati, contribuendo a portare a termine questo lavoro. Grazie a Sara, Linda e Deborah, le mie "Charlie's Angels", perchè senza di loro, spesso, non saprei come fare. Grazie a Teta, per far costantemente parte della mia vita ormai da 14 anni, nonostante la distanza e le rispettive impegnative vite. Grazie a Vincenzo, Rocco, Alessandro, Tiziana e tutti i ragazzi che durante questo periodo di permanenza al CNR hanno condiviso con me le pause pranzo, gli "scleri" e le risate, e che sono stati sempre estremamente disponibili di fronte alle mie svariate richieste d'aiuto. Grazie anche ad Elisabeth, per il suo sostegno, ad Acela e a tutto il gruppo di ballo, per aver pazientemente compreso la mia (quasi) assenza di questi 10 mesi. Grazie, insomma, a chi c'è, a chi c'è stato e a chi non c'è più, a chi è riuscito a starmi accanto nei momenti di maggiore stress e nervosismo, e a chi no, perchè ognuna delle persone che ho incontrato lungo il mio cammino ha contributo (a modo suo) a farmi arrivare fino a qui. Infine, anche se forse un pò insolito, un piccolo grazie anche a me, perchè delle volte ho bisogno di ricordare a me stessa che esisto anche io, e perchè, come dico sempre io (e come dicono i Five for Fighting): "it's not easy to be me"...